Copyright
by
David Hernán Menéndez Arán
2013

The Thesis committee for David Menéndez Arán

certifies that this is the approved version of the following thesis:

Hydrodynamic Optimization and Design of Marine Current Turbines and Propellers

APPROVED BY

SUPERVISING COMMITTEE:

Spyros A. Kinnas, Supervisor

Brenden Epps

Hydrodynamic Optimization and Design of Marine Current Turbines and Propellers

by

David Hernán Menéndez Arán, B.S.

THESIS

Presented to the Faculty of the Graduate School of

The University of Texas at Austin

in Partial Fulfillment

of the Requirements

for the Degree of

MASTER OF SCIENCE IN ENGINEERING

THE UNIVERSITY OF TEXAS AT AUSTIN

August 2013

Dedicated to my family for their enduring support, especially my parents Ana and Norberto and my wife Amy.

Acknowledgments

I wish to thank the people who helped make this thesis a reality. In particular, I want to acknowledge my adviser, Dr. Kinnas, whose guidance was invaluable; Ye Tian, for his assistance throughout my research; and everyone else in the Ocean Engineering Group, for the help and friendship during my time at the University of Texas. I would also like to thank Dr. Epps for agreeing to be the second reader and lending me his expertise in the field, and Dr. Hull for his assistance in developing the optimization methodology.

This thesis was supported by the U.S. Office of Naval Research (Contracts N00014-07-1-0616 and N00014-10-1-0931) and members of the Phase VI of the Consortium on Cavitation Performance of High Speed Propulsors: American Bureau of Shipping, Kawasaki Heavy Industry Ltd., Rolls-Royce Marine AB, Rolls-Royce Marine AS, SSPA AB, Andritz Hydro GmbH, Wärtsilä Netherlands B.V., Wärtsilä Norway AS, Wärtsilä Lips Defense S.A.S. and Wärtsilä CME Zhenjiang Propeller Co. Ltd.

Hydrodynamic Optimization and Design of Marine Current Turbines and Propellers

David Hernán Menéndez Arán, M.S.E.
The University of Texas at Austin, 2013

Supervisor: Spyros A. Kinnas

This thesis addresses the optimization and design of turbine and propeller blades through the use of a lifting line model.

An existing turbine optimization methodology has been modified to include viscous terms, non-linear terms, and a hub model. The method is also adapted to the optimization of propellers. Two types of trailing wake geometries are considered: one based on helical wakes which are aligned at the blade (using the so-called "moderately loaded propeller" assumption), and a second one based on a full wake alignment model in order to represent more accurately the wake geometry and its effect on the efficiency of the rotor.

A comparison of the efficiencies and the loading distributions obtained through the present methods is presented, as well as convergence and numerical accuracy studies, and comparisons with existing analytical results. In the case of turbines, various types of constraints are imposed in the optimization

method in order to avoid abrupt changes in the designed blade shape. The effect of the constraints on the efficiency of the turbines is studied. Once the optimum loading has been determined, the blade geometry is generated for given chord, thickness and camber distributions. Finally, a low-order potential-based boundary element method and a vortex-lattice method are used to verify the efficiency of the designed turbines.

Table of Contents

Acknowledgments **v**

Abstract **vi**

List of Tables **xi**

List of Figures **xiii**

Nomenclature **xviii**

Chapter 1. Introduction **1**

1.1 Renewable Energy 1
1.2 Hydrokinetic Energy 4
1.3 Marine Current Turbines 6
1.4 Objective 8
1.5 Organization 9

Chapter 2. Literature Review **10**

2.1 Lifting Line Method (LLM) 10
2.2 Vortex Lattice Method (VLM) 12
2.3 Boundary Element Method (BEM) 12

Chapter 3. Methodology **14**

3.1 Turbines 14
3.1.1 Actuator Disk Theory 14
3.1.2 Lifting Line Theory 16
3.1.3 Optimization Formulation 18
3.1.4 Inclusion of Hub Effects 24
3.1.5 Glauert Series Representation 26

3.1.6 Polynomial Representation 28
3.1.7 Constrained Optimization 29
3.2 Propellers 34
3.2.1 Actuator Disk Theory 34
3.2.2 Optimization Formulation 36
3.2.3 Inclusion of Hub Effects 40
3.3 Wake Models 41
3.3.1 Lerbs-Wrench Model 41
3.3.2 Wake Alignment Model 44
3.3.3 Numerical Accuracy 52
3.4 Generation of Blade Geometry 58

Chapter 4. Results **61**
4.1 Turbines 61
4.1.1 LLOPT-LW 61
4.1.2 LLOPT-FWA 65
4.1.2.1 Constraints on Alignment 67
4.1.2.2 Constraints on Loading 71
4.1.3 Comparison of Results 81
4.1.4 Blade Geometry 83
4.1.5 Analysis with VLM and BEM 88
4.2 Propellers 94
4.2.1 LLOPT-LW 94
4.2.2 LLOPT-FWA 98
4.2.3 Comparison of Results 103

Chapter 5. Conclusions and Recomendations **111**
5.1 Conclusions 111
5.2 Recommendations 113

Appendices **115**

Appendix A. Maximum Efficiency for a Constant-Loading Turbine **116**

Appendix B. Non-Linear Lifting Line Optimization **122**
B.1 Formulation 122
B.2 Preliminary Results and Recommendations 124

Appendix C. NACA Data for Blade Geometry Design **127**
C.1 NACA Mean Line a = 0.8 127
C.2 NACA 66 Modified 129

Bibliography **130**

Vita **138**

List of Tables

1.1 Comparison of available technologies for electricity generation 3

3.1 Wake geometry discretization parameters for the cases analyzed 55

3.2 Relative error of different wake discretizations with respect to the results obtained through the use of the Lerbs-Wrench formulas and a very precise numerical wake ($dth = 0.5$, $nc = 80000$, $L_w = 35$). Average values of relative error for all control points on the blade 57

4.1 Comparison of efficiencies for the unconstrained LLOPT-FWA model, varying values of the drag-to-lift ratio κ. ($Z = 3$, $TSR = 5$) 65

4.2 Comparison of efficiencies for the unconstrained LLOPT-SWA model, varying values of the drag-to-lift ratio κ. ($Z = 2$, $TSR = 5$) 69

4.3 Comparison of efficiencies with respect to number of modes and functional representation. Absolute difference with respect to original unconstrained LLOPT-FWA model. ($Z = 2$, $TSR = 4$) 74

4.4 Comparison of efficiencies with respect to number of modes and control points for constrained optimization models. Absolute difference with respect to original unconstrained LLOPT-FWA model. ($Z = 2$, $TSR = 4$) 77

4.5 Comparison of efficiencies between constrained and unconstrained optimization models, for the case of a turbine with hub. Absolute difference with respect to original unconstrained LLOPT-FWA model. ($Z = 2$, $TSR = 4$) 80

4.6 Comparison of efficiencies as calculated by different models. Absolute difference with respect to LLOPT-FWA model. ($Z = 1$, $TSR = 8$) 90

4.7 Comparison of efficiencies as calculated by MPUF-3A for the case of a two-bladed turbine with hub. Absolute difference with respect to LLOPT-FWA model. ($Z = 2$, $TSR = 4$) 93

4.8 Efficiencies for LLOPT-LW model, hub-less propeller ($Z = 5$) . 96

4.9 Efficiencies for LLOPT-LW model, propeller with hub ($Z = 5$) 97

4.10 Efficiencies for LLOPT-FWA model, hub-less propeller ($Z = 5$) 100
4.11 Efficiencies for LLOPT-FWA model, propeller with hub ($Z = 5$) 101

C.1 Data for NACA a=0.8 128
C.2 Data for modified NACA 66 129

List of Figures

1.1 Installation of a 35kW three-bladed horizontal-axis marine turbine. Free Flow System turbine being lowered into East River, New York, December 2006 7

1.2 Two 1.2MW two-bladed horizontal-axis marine turbines. SeaGen Project, located in Strangford Lough, Northern Ireland 8

3.1 Schematic of actuator disk model, turbine case (based on original figure by www.offshoremoorings.org) 15

3.2 Discretization scheme for the lifting line model, where the line vortex on the key blade is represented by M horseshoe vortices 17

3.3 Combined velocity and force diagram on blade section at radius r, turbine case 19

3.4 Image model for a 2D point vortex in a circle of radius r_h . . . 26

3.5 Two possible constrained optimization models: a) only imposing an inequality constraint on the curvature; b) adding a constraint on the slope ($Z = 2, TSR = 4$). 31

3.6 Schematic of actuator disk model, propeller case 35

3.7 Combined velocity and force diagram on blade section at radius r, propeller case 37

3.8 Flowchart of Lerbs-Wrench algorithm (LLOPT-LW) 43

3.9 Flowchart of Full Wake Alignment algorithm (LLOPT-FWA) . 46

3.10 Velocity induced by a vortex segment $X1 - X2$ of strength Γ on a point P 47

3.11 Alignment of the wake geometry and the induced velocity vectors induced on the wake panels (key blade coincident with y axis, inflow in the x-axis direction) 49

3.12 Comparison of wake shapes for two different alignment schemes: Full Wake Alignment (top) and Simplified Wake Alignment (bottom). $Z = 1$, $TSR = 8$ 50

3.13 Comparison of wake cross sections for two different alignment schemes: Full Wake Alignment (left) and Simplified Wake Alignment (right). The curves are obtained through the intersection of the 3D wake surface with the xz plane (at $y = 0$). $Z = 1$, $TSR = 8$, varying number of radial elements (m) 51

3.14 Normalized axial velocity. Validation of the numerical method by comparison with Lerbs-Wrench formulas: a) single vortex at the blade's mid-point, for different pitch angles; b) single tip vortex, for different pitch angles; c) horseshoe vortex at the blade's mid-point ($\beta_w = 15°$); d) horseshoe vortex at the blade's tip ($\beta_w = 15°$) 53

3.15 Constant-pitch wake used to simulate the use of the Lerbs-Wrench formulas ($L_w = 15$, $dth = 1$, $nc = 1500$) 54

3.16 Circulation distributions for the first iteration of the optimization code, for different wake discretization schemes ($Z = 2$, $TSR = 10$) 56

3.17 Comparison of LLOPT-LW using Lerbs-Wrench formulas to a model using a discretized wake, results for the first three iterations ($Z = 2$, $TSR = 4$) 58

3.18 Comparison of blade geometries as generated from unconstrained and constrained LLOPT-FWA models for a turbine with a hub ($Z = 2$, $TSR = 4$) 60

4.1 Optimum efficiency as a function of tip speed ratio for different values of drag-to-lift ratio κ, LLOPT-LW model, different number of blades Z 62

4.2 Glauert series and polynomial representation with Lerbs-Wrench model, $Z = 3, TSR = 6$, turbine with hub 64

4.3 Convergence analysis for the optimal circulation distribution, for different number of radial sections, simplified wake alignment and varying drag-to-lift ratio κ ($TSR = 5$, $Z = 3$). . . . 66

4.4 Comparison of optimum circulation distributions for Full and Simplified Wake Alignments ($TSR = 4$, $Z = 2$) 67

4.5 Comparison of results for LLOPT-SWA and LLOPT-LW models ($TSR = 5$, $Z = 2$) 68

4.6 Convergence analysis for the optimal circulation distribution, for different number of radial sections, simplified wake alignment and varying drag-to-lift ratio κ ($Z = 2$, $TSR = 5$). . . . 69

4.7 Optimum efficiency as a function of tip speed ratio for different values of drag-to-lift ratio κ, LLOPT-SWA model, different number of blades Z 70

4.8 Optimum circulation distributions for the case of a turbine with hub, Full and Simplified Wake Alignments. ($TSR = 4$, $Z = 2$) 71

4.9 Comparison between unconstrained LLOPT-FWA and functional representations, different values of NG parameter ($Z = 2, TSR = 4$). 73

4.10 Comparison of circulation distribution multiplied by number of blades ($Z\Gamma$) for LLOPT-LW and constrained LLOPT-FWA. ($TSR = 6$, varying number of blades) 75
4.11 Convergence analysis of the constrained optimization method, curvature-only case ($Z = 2, TSR = 4$). 76
4.12 Convergence analysis of the constrained optimization method, curvature and slope case ($Z = 2, TSR = 4$). 76
4.13 Comparison of circulation distributions between constrained and unconstrained LLOPT-LWA, different Z and TSR 78
4.14 Comparison between constrained and unconstrained LLOPT-LWA. ($Z = 2$, $TSR = 4$) 78
4.15 Ratio between the aligned pitch angle β_i and the geometric pitch angle β, for different values of Z and TSR 79
4.16 Optimum circulation distributions for turbines with hubs. Comparison of solution for unconstrained optimization with both unconstrained polynomial representation and constrained optimization distributions ($Z = 2$, $TSR = 4$). 80
4.17 Comparison of efficiencies obtained through different lifting line optimization methods, different number of blades Z 81
4.18 Convergence of both models with number of iterations. The LLOPT-FWA results include both the unconstrained and constrained versions. ($Z = 2$, $TSR = 4$) 83
4.19 Comparison of blade geometries; vortex-lattice method (MPUF-3A) and boundary element method (PROPCAV); $Z = 1, TSR = 8$, based on optimum loading as determined by unconstrained LLOPT-FWA. 85
4.20 Blade geometry for a two-bladed turbine with hub, based on optimum loading as determined by constrained LLOPT-FWA. ($Z = 2$, $TSR = 4$) 87
4.21 Comparison of wake geometries; slice of the wake at an xz plane at $y = 0$. LLOPT-FWA wake in black; PROPCAV aligned wake in red, MPUF-3A unaligned wake (geometric pitch) in blue. . 88
4.22 Comparison of circulation distributions between the input optimal circulation (unconstrained LLOPT-FWA) and the one calculated from the designed blade (MPUF-3A and PROPCAV). ($Z = 1$, $TSR = 8$) 89
4.23 Comparison of circulation distributions between the input optimal circulation (constrained LLOPT-FWA) and the one calculated from the designed blade (MPUF-3A and PROPCAV). ($Z = 2$, $TSR = 4$) 91

4.24 Comparison of circulation distributions for thickness factor $t_f = 0.25$ and varying number of panels 92
4.25 Comparison of circulation distributions between the input optimal circulation (constrained LLOPT-FWA) and the one calculated from the designed blade using the MPUF-3A model for a turbine with hub ($Z = 2$, $TSR = 4$). The corresponding efficiencies are presented in Table 4.7. 93
4.26 Comparison of results for circulation distribution ($C_T = 0.512$, $Z = 5$). PLL results from class notes by Kerwin 94
4.27 Comparison of circulation distributions for different M, LLOPT-LW model 95
4.28 Comparison of circulation distributions for different M, LLOPT-FWA model 98
4.29 Wake geometry corresponding to the optimum circulation distribution for a propeller, $Z = 5$, $C_T = 0.512$, different J. a.1) $J = 0.6$, key blade; a.2) $J = 0.6$, all blades (cross section with respect to y axis); b.1) $J = 1.4$, key blade; b.2) $J = 0.6$, all blades (cross section with respect to y axis) 102
4.30 Comparison of optimum circulation distributions for different advance ratios J and design thrust C_T; $Z = 5$ 103
4.31 Comparison of optimum circulation distributions for different number of blades Z 104
4.32 Comparison of induced axial velocities u_a on the key blade, $J = 1$, $Z = 5$, different C_T 105
4.33 Comparison of induced tangential velocities u_t on the key blade, $J = 1$, $Z = 5$, different C_T 105
4.34 Comparison of induced axial velocities u_a on the key blade, $J = 0.7$, $C_T = 1.8$, different Z 106
4.35 Comparison of efficiencies for both methods at different J, $Z = 5$, different C_T 107
4.36 Relative error of efficiencies as calculated by both methods. Values expressed in percentages (%), for a hub-less five-bladed propeller 108
4.37 Relative error of efficiencies as calculated by both methods. Values expressed in percentages (%), for a five-bladed propeller with infinite hub 109
4.38 Convergence of both models with number of iterations ($J = 0.4$, $Z = 5$, $C_T = 2$) 109

4.39 Ratio between the aligned pitch angle β_i and the geometric pitch angle β, for different values of C_T. ($Z = 5$, $J = 0.3$) 110

B.1 Circulation distributions as a function of the normalized radius for a three-bladed turbine using inviscid linear (LLOPT-LW) and non-linear methods. ($Z = 3$; $M = 20$; $TSR = 6$; $r_h/R = 0.2$) 125

C.1 Pressure distribution and camber line for NACA a=0.8 127

Nomenclature

Latin Symbols

A	Rotor area, $A = \pi R^2$
c	Blade chord length
C_D	Sectional drag coefficient, $C_D = \frac{D}{0.5\rho V^2 c}$
C_L	Sectional lift coefficient, $C_L = \frac{L}{0.5\rho V^2 c}$
C_p	Pressure coefficient, $C_p = \frac{P-P_\infty}{2\rho n^2 R^2}$
C_{pow}	Power coefficient, $C_{pow} = \frac{Q\omega}{0.5\pi V^3 R^2}$
C_Q	Torque coefficient, $C_Q = \frac{Q}{0.5\rho\pi V^2 R^3}$
C_T	Thrust coefficient, $C_T = \frac{T}{0.5\rho\pi V^2 R^2}$
Dia	Rotor diameter, $Dia = 2R$
D	Drag
dth	Time step for wake geometry
f	Camber
f_{max}	Maximum camber
f_0	Ideal maximum camber for $C_L = 1$
J	Advance ratio, $J = \frac{V}{2nR} = \frac{\pi}{TSR}$
K_Q	Torque coefficient, $K_Q = \frac{Q}{32\rho n^2 R^5}$
K_T	Thrust coefficient, $K_T = \frac{T}{16\rho n^2 R^4}$
L	Lift
L_w	Wake lengh

n	Rotational frequency
nc	Number of streamwise panels for wake geometry
Q	Torque
r	Radius of rotor blade section
r_h	Hub radius
R	Rotor radius
t	Blade thickness
t_{max}/c	Maximum thickness to chord ratio
T	Thrust
TSR	Tip Speed Ratio, $TSR = \frac{\omega R}{V} = \frac{\pi}{J}$
u_a^*	Induced axial velocity
u_t^*	Induced tangential velocity
V	Current speed
V^*	Total inflow velocity relative to the rotor sections
x, y, z	Propeller fixed coordinates
Z	Number of blades

Greek Symbols

α_0	Ideal angle of attack for $C_L = 1$
α_i	Ideal angle of attack
β	Undisturbed wake pitch angle, $\tan(\beta) = \frac{V}{\omega R}$
β_i	Wake pitch angle
Δr	Radius interval between vortex points
Γ	Circulation
η	Turbine efficiency, $\eta = \frac{Q\omega}{0.5\rho\pi V^3 R^2}$
η	Propeller efficiency, $\eta = \frac{K_T}{K_Q}\frac{J}{2\pi} = \frac{C_T}{C_Q}\frac{J}{\pi}$
ϕ	Blade pitch angle
κ	Drag-to-lift ratio, $\kappa = \frac{C_D}{C_L}$
ω	Rotor angular velocity
ρ	Fluid density

Acronyms

BEM	Boundary Element Method
CPU	Central Processing Unit
NACA	National Advisory Committee for Aeronautics
LLM	Lifting Line Method
VLM	Vortex Lattice Method

Computer Program Names

LLOPT-LW	Lifting line optimization using Lerbs-Wrench formulas
LLOPT-FWA	Lifting line optimization using Full Wake Alignment
LLOPT-SWA	Lifting line optimization using Simplified Wake Alignment
MPUF-3A	Cavitating propeller potential flow solver based on VLM
PROPCAV	Cavitating propeller potential flow solver based on BEM

Chapter 1

Introduction

1.1 Renewable Energy

Worldwide energy consumption is continuously raised year after year by the increasing global population and industrial development. A large majority of this growing demand has been traditionally covered with non-renewable fossil fuels, which are not sustainable long term and pollute the environment. Virtually nonexistent five decades ago, non-hydropower renewable energies have been the object of numerous research projects by governments and private companies looking to produce cost-effective technologies to replace traditional coal and fossil fuel sources.

Solar and wind energy have received a lot of attention in the last several decades, and as a consequence they are currently the most developed renewably energies available in the market. Solar energy has proven competitive mainly for decentralized generation, but daily and monthly fluctuations are still a problem for large scale plants because solar storage technology has not yet reached its potential. Furthermore, the capital cost of installing solar panels is still high compared to conventional electricity sources. Onshore wind energy plays a key role in many countries' long term energy plans, and the cost per

kilowatt of utility power installed rivals most that of most conventional fuel plants. However, the unpredictability of wind energy is still a hurdle for its use as a replacement of fossil fuel and nuclear energy for baseload demand.

Ocean and hydrokinetic energy, virtually inexistent a decade ago, have grown faster than any other energy sector. Similarly to wind energy, this energy is clean, renewable and free of fuel costs. Most research has focused on *wave energy*, harnessing the power of wind-driven waves, and *hydrokinetic energy*, harnessing the energy from water currents. Despite the similarities between wind energy and hydrokinetic energy, the harsher environment in which hydrokinetic turbines must operate present a new set of problems that must be solved in order to make marine energy projects economically feasible.

Table 1.1 presents a basic comparison of different energy sources. Cost estimates are based on the Levelized Cost of Energy Analysis developed by Lazard [31] and other characteristics are based on the Energy Information Administration's Annual Energy Outlook [2]. It is expected that well-optimized hydrokinetic projects will be able to compete with onshore wind farms, once the many remaining engineering and regulatory obstacles have been surpassed.

Characteristic	Hydrokinetic	Fossil fuel	Onshore wind	Offshore wind	Solar
Energy density	High	Very high	Low	Moderate	Low
Predictability	High	High (coal and gas)	Low, except in some sites	Moderate	Varying
Capacity factor	$55\% - 90\%$	$50\% - 90\%$	$25\% - 35\%$	$25\% - 40\%$	$10\% - 30\%$
Emissions	None	Carbon, NOx, SO2, Mercury	None	None	None
Visual impact	Minimal	From unobtrusive to high	Moderate	Low to moderate	From unobtrusive to high
Potential sites	Very high - U.S.A. can double hydropower growth without building a new dam	Extensive but permitting process can be lengthy and social component to development is increasingly difficult	High in some areas, but not practical; low to moderate in other areas	Limited in US, Moderate in Europe	Limited for high energy density, extensive for low to moderate density
Cost per kW/h	$3 - 10$ cents (estimated)	$4 - 7$ cents	$5 - 8$ cents	$8 - 12$ cents	$12 - 25$ cents

Table 1.1: Comparison of available technologies for electricity generation (based on the Levelized Cost of Energy Analysis developed by Lazard [31] and on the Energy Information Administration's Annual Energy Outlook [2])

1.2 Hydrokinetic Energy

Hydrokinetic energy has many environmental benefits, since unlike conventional hydropower turbines, hydrokinetic turbines do not require dams to capture potential energy, which have been increasingly resisted by communities aware of the environmental impact caused by flooding. Similar to wind turbines, water current turbines do not emit Green House Gases (GHG) during operation, and only minimal amounts during construction. However, the latter also has the added benefits of no visual impact or noise pollution, two of the major complaints against wind farms.

Most hydrokinetic devices are still in the trial phase, with many pilot turbines currently being installed by several private developers. However, early evidence indicates that the environmental impact on the marine environment is likely to be limited (Frid et al, 2012 [15]). Bird and mammal collisions and displacement by marine turbines were studied by Haskoning UK Ltd. (2011) [38] for the SeaGen project located in Northern Ireland (see Figure 1.2), who found little effect on the local fauna because of the slow optimum rotational speeds. The impact of noise on fish has yet to be evaluated in depth, but it is expected that the it will be possible to limit noise generated on dangerous frequencies. It will also be important to limit noise during the construction of turbine arrays. Lloyd et al (2011) [36] attempts to model the noise generated by arrays of different tidal turbine prototypes.

Another possible source of impact are the electromagnetic fields generated by underwater electric cables that connect the turbines to the power

grid. Various fish species and other marine organisms, such as sharks and marine mammals, are attracted to these fields, but there is not evidence of wide impact for offshore power cables (Öhman et al, 2007 [44]). On the other hand, Langhamer and Wilhelmsson (2009) [30] show that offshore structures like those used by hydrokinetic turbines can enhance fish and invertebrate populations. Some studies show that offshore wind farms also have a positive impact on fish populations (Wilhelmsson et al, 2006 [49]), so a similar effect is expected from offshore marine turbine projects. These conclusions are however based on limited data, so major coordinated studies will be necessary in the future as large scale projects are developed.

Hydrokinetic turbines also offer great energy management flexibility, adapting to in-stream and low-head projects, and even to man-made irrigation channels. They are easy to place in remote sites with low power needs, and can be scaled up in case demand increases. Ocean energy is in general more reliable and predictable than other intermittent renewable energies, with a high usage factor, and have no need of storage. Developers have the opportunity to use pre-manufactured modular systems and cheaper and smaller support structures than for wind turbines, whereas independent power investors can be lured by the short construction timelines, which assure a fast cash inflow. This is not intended by any means as an exhaustive list of the many advantages hydrokinetic energy provides, but serves as a quick summary of the reasons that have led marine energy to become the most promising new field for renewable energy.

The estimated global wave resources alone could generate $6,000TWh$ (terawatt-hours) per year, and tidal resources could account to up to $700TWh$ per year [46]. A report by Pike Research [3] estimates a wide range for potential ocean energy development by 2025. It states that more than 300 hydrokinetic projects are currently in the works around the world, and that the global installed capacity could reach anywhere from $25GW$ to potentially as high as $200GW$ by 2025. The United Kingdom governments Marine Energy Action Plan of 2010 [43] estimates that 1 to $2GW$ of marine energy could be installed in just in that country by 2020. Despite these positive signs for the future of marine energy worldwide, the main disadvantage of hydrokinetic energy is the current lack of a regulatory framework to encourage the research and development of standardized designs for this relatively untested technology.

1.3 Marine Current Turbines

Many different types of hydrokinetic turbine designs have been proposed, but they can largely be divided into: *horizontal axis* and *vertical axis* turbines. Horizontal axis turbines can be further broken into two groups: *parallel axis* turbines, where the axis is parallel to the water stream direction, and *perpendicular axis* turbines, where the axis is perpendicular to the water stream direction (Güney et al, 2010 [18]). Figure 1.1 shows the installation of a 35kW horizontal-axis turbine in the East Channel of the East River in New York, USA, as part of the RITE project (www.theriteproject.com/). Figure 1.2 presents one of the largest hydrokinetic turbines currently installed, two

two-bladed horizontal axis turbines developed and installed by Sea Generation Ltd. in Strangford Lough, Northern Ireland.

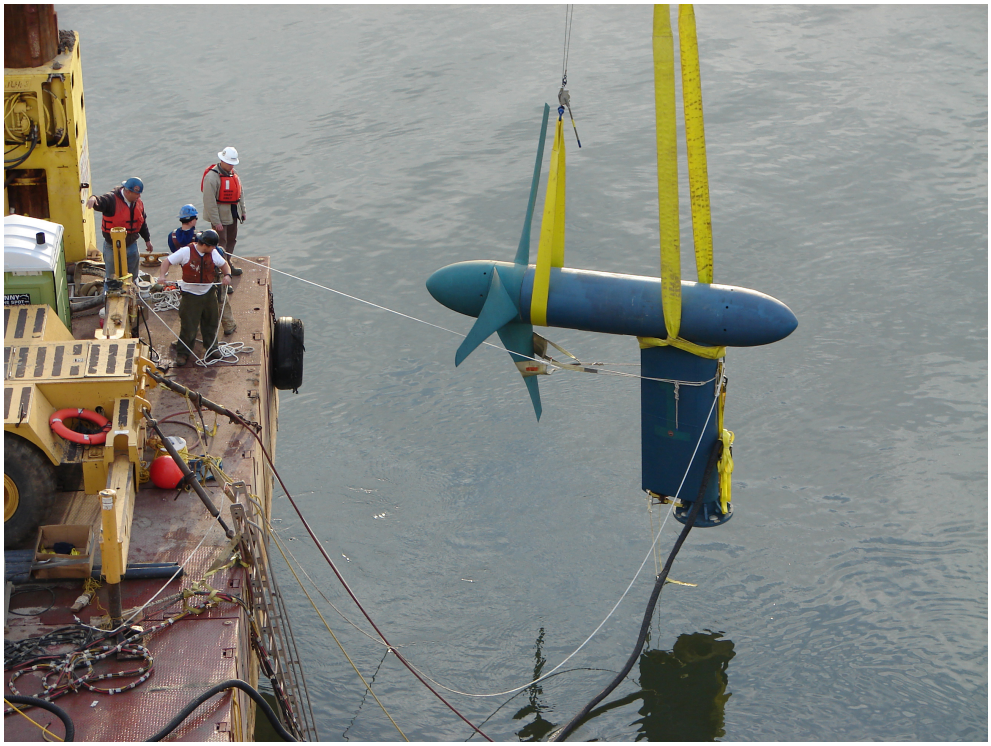

Figure 1.1: Installation of a 35kW three-bladed horizontal-axis marine turbine. Free Flow System turbine being lowered into East River, New York, December 2006. Kris Unger / Verdant Power, Inc. (source: verdantpower.com/media-free/)

Classic water wheels and cross flow turbines are examples of horizontal perpendicular water turbines, and have been used for many decades for varied applications. Most recent research has focused on vertical axis and parallel horizontal axis turbines, although some turbines can be used in both horizontal and vertical positions. The optimization tools developed in this thesis are

Figure 1.2: Two 1.2MW two-bladed horizontal-axis marine turbines. SeaGen Project, located in Strangford Lough, Northern Ireland (source: www.siemens.co.uk/)

mainly tailored to two- and three-bladed horizontal axis turbines, but can be applied to turbines with any number of blades.

1.4 Objective

Numerous hydrokinetic projects have so far been proposed, and pilot turbines are currently being tested, but this remains an expensive technology that often requires subsidies to be feasible. Furthermore, very few design tools have been created and made public, thus forcing engineers to opt for more traditional alternatives with high environmental impact. As the designs im-

prove and higher efficiencies are achieved, more and more projects will become economically and technically feasible.

This thesis seeks to develop and improve upon several optimization tools that will allow the design of efficient hydrokinetic turbines. A preliminary design methodology is proposed and tested for accuracy with a vortex lattice method and a boundary element method. As a complimentary objective, this thesis evaluates the accuracy of the moderately loaded propeller hypothesis in the optimization of propellers.

1.5 Organization

This thesis is organized into five chapters. *Chapter 1* introduced the concepts of marine energy, hydrokinetic turbines and this thesis's objective. *Chapter 2* presents a short literature review, describing previous developments in related topics. *Chapter 3* includes the methodology followed, discriminating between turbine and propeller optimization. *Chapter 4* presents the results obtained. *Chapter 5* comprises conclusions and recommendations for future research.

Chapter 2

Literature Review

2.1 Lifting Line Method (LLM)

The development of optimization tools for the design of efficient marine turbines has been one of the focuses of recent research for those interested in this nearly untapped renewable energy resource. Betz (1920) [6] determined by means of the actuator disk theory the maximum efficiency limit for such a device, known as the Betz limit, and it is explained in detail in Section 3.1. Thus, any inviscid model looking to represent this phenomenon should reach this limit for an idealized situation whose conditions approach those of the actuator disk.

Falcão de Campos (2007) [13] developed an optimization model based on lifting line theory and a classical helical vortex model of constant pitch. Vortex wake deformation was thus neglected, and the induced velocities were assumed to have a linear behavior such that $\tan(\beta_i)/\tan(\beta) = \gamma$, where γ is a constant. This condition is equivalent to assuming a constant-pitch trailing wake. Epps et al (2009) [12] have developed OpenProp, an open source software for axial-flow turbines and marine propulsor optimization. This code also determines the optimum circulation distribution for a given set of geo-

metrical parameters, and calculates influence coefficients through the use of the Lerbs-Wrench asymptotic formulas. Epps and Kimball (2013) [11] formulated a hybrid lifting-line/momentum-theory optimization procedure that can be applied to both propellers and turbines, which is based on the momentum theory assumptions of (i) a constant-pitch wake and (ii) that the induced velocities at a given radius are independent of the circulation at other radii. The efficiencies as calculated by this method approach Betz's limit for high number of blades and high rotational velocity.

This thesis builds on previous research carried out in the Ocean Engineering Group at the University of Texas. Zan (2008) [54] developed the initial inviscid linear formulation, and discretizing the lifting line into a series of horseshoe vortices. Xu (2010) [52], Xu and Kinnas (2010) [51], and Kinnas et al (2012) [29] improved the results through a circulation database method and set up a design methodology that considered viscous effect and cavity optimization. Menéndez Arán and Kinnas (2012) [39] proposed to circumvent the database method through a non-linear model, but preserved the use of the Wrench formulas, which assume that the vortex sheet trailing behind the turbine forms a helical surface of constant pitch. In other words, the individual horseshoe vortices are helicoidal and their pitch is aligned with the flow only at the lifting line (moderately loaded propeller assumption). Menéndez Arán and Kinnas (2013) [40] abandoned this assumption and included into the optimization process a full wake alignment model in order to better model its influence on the efficiency of a hydrokinetic turbine.

2.2 Vortex Lattice Method (VLM)

The code used in this thesis is called MPUF-3A (Mid-chord cavity detachment - Propeller Unsteady Flow). It solves the potential flow around a rotor by placing sources and vortices on a lattice describing the rotor blades' mean camber surface and the wake, and calculating their strength so that all kinematic and dynamic boundary conditions are satisfied. The Vortex Lattice Method has proven very successful at the analysis of propellers, and has been commonly used in hydro- and aerodynamic applications for decades. This method was first applied to fully wetted propeller analysis by Kerwin and Lee (1978) [24]. It was extended by Lee (1979) [32] and Breslin et al. (1982) [7] to model unsteady sheet cavitating propeller flows, and Fine and Kinnas (1989) [14] improved the numerical scheme in order to introduce the possibility of midchord cavity detachment. Kerwin et al (1986) [21] and Kinnas (1991) [25] implemented a leading-edge correction to include the non-linear effects on the blade loading caused by the blade thickness. Kinnas and Pyo (1999) [28] included an image model to consider the effects of the propeller hub and a geometric wake alignment to account for shaft inclination. More recently, Kinnas et al (2012) [29] applied the model to hydrokinetic turbines.

2.3 Boundary Element Method (BEM)

The boundary element model used is called PROPCAV (PROPeller CAVitation). It is a low-order perturbation potential based panel method, with piecewise constant dipole and source distributions. The model was first

developed for non-cavitating propeller flows by Lee (1987) [34] and Kerwin et al. (1987) [23]. It was extended to treat cavitating hydrofoils and propellers by Kinnas and Fine (1993) [27] and Fine and Kinnas (1993) [14]. The code had been frequently updated through the years. A significant addition was carried out by Lee and Kinnas [33], who included an unsteady wake alignment model and the effects of tip vortex cavitation. The latest version includes the wake alignment model developed by Tian and Kinnas (2012), also used for the LLOPT-FWA model presented in Section 3.3.2. Kinnas et al (2012) [29] used the model to analyze hydrokinetic turbines.

Chapter 3

Methodology

3.1 Turbines

3.1.1 Actuator Disk Theory

Turbines generate energy by extracting part of the kinetic energy contained in a stream tube, thus slowing it down below free-stream speed. If all the energy is used, then the water speed behind the turbine would be zero, which would block any new water from crossing the plane of the turbine. The speed behind the turbine must then be a finite non-zero value, and the derivation of the optimum value was performed by Betz [6].

The presence of the turbine also causes an expansion of the stream tube and an increase in the pressure immediately downstream. Far downstream, the pressure slowly drops back toward the free-stream pressure, and it is assumed that frictional forces are negligible when compared with momentum flux and pressure changes. Betz's theory is based on the representation of the turbine as an open *actuator disk*, an infinitely thin ideal rotor over whose surface both loading and velocity are uniform. Figure 3.1 shows a schematic of the model described, where V is the inflow velocity, α is the coefficient of velocity deficit immediately downstream from the disk and u_w is the deficit velocity in the stream tube far downstream.

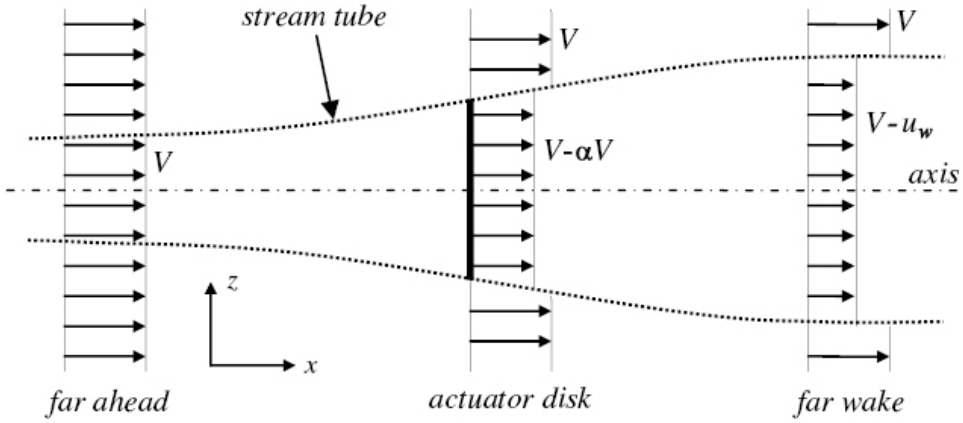

Figure 3.1: Schematic of actuator disk model, turbine case (based on original figure by www.offshoremoorings.org)

Momentum theory can be used to determine the maximum amount of power that can be extracted from the flow, as shown by Burton et al [9]. To that effect a simple expression for the ratio of power extracted C_{pow} can be used:

$$C_{pow} = \frac{P}{\frac{1}{2}\rho V^3 A} = \eta \tag{3.1}$$

where P is the total power extracted, ρ is the density of the fluid and A is the area of the actuator disk. This expression can also be interpreted as the efficiency of the actuator disk, represented in this thesis by the Greek letter η. Burton et al [9] prove that the power P generated by the rotor is a function of the coefficient α, as given by:

$$P = 2\rho V^3 A\alpha(1-\alpha)^2 \tag{3.2}$$

Replacing P in Equation 3.1, we obtain an expression for the power

coefficient C_{pow} as a function of only one parameter, α. To maximize the efficiency of the actuator disk we then differentiate C_{pow} with respect to α and find the value for which the first derivative is equal to 0.

$$C_{pow} = 4\alpha(1-\alpha)^2 \tag{3.3}$$

$$\frac{dC_{pow}}{d\alpha} = 4(1-\alpha)(1-3\alpha) = 0 \tag{3.4}$$

The maximum value for $C_{pow} = \eta$ occurs for $\alpha = 1/3$, which means that the magnitude of the velocity induced by the rotor must be equal to one third of the free stream velocity. The optimum efficiency is $\eta_{max} = 16/27 \approx 0.5926$, know as *Betz's limit*. It is to be expected that our numerical models should asymptotically approach this limit, for an inviscid case, as the Tip Speed Ratio (TSR) and the number of blades increase.

3.1.2 Lifting Line Theory

The turbine is represented through a lifting line model, in which the cross section presents a vanishing chord length. Thus each one of the rotor blades is represented by a radial concentrated line vortex of varying strength $\Gamma(r)$ (bound vortex), which generates a more or less helical wake (free vortex sheet). We select one of the blades for the analysis (key blade) and assume that all the blades have the same circulation distribution. The wake produced by the rotating turbine induces axial and tangential velocities on the key blade, modifying the pitch angle β_i.

The bound vortex is discretized into M horseshoe vortices with varying

distributions of vortex and control points. Figure 3.2 shows the resulting system, in which the strength of an intermediate vortex is given by the strength variation $\Delta\Gamma$ with respect to its adjacent vortices.

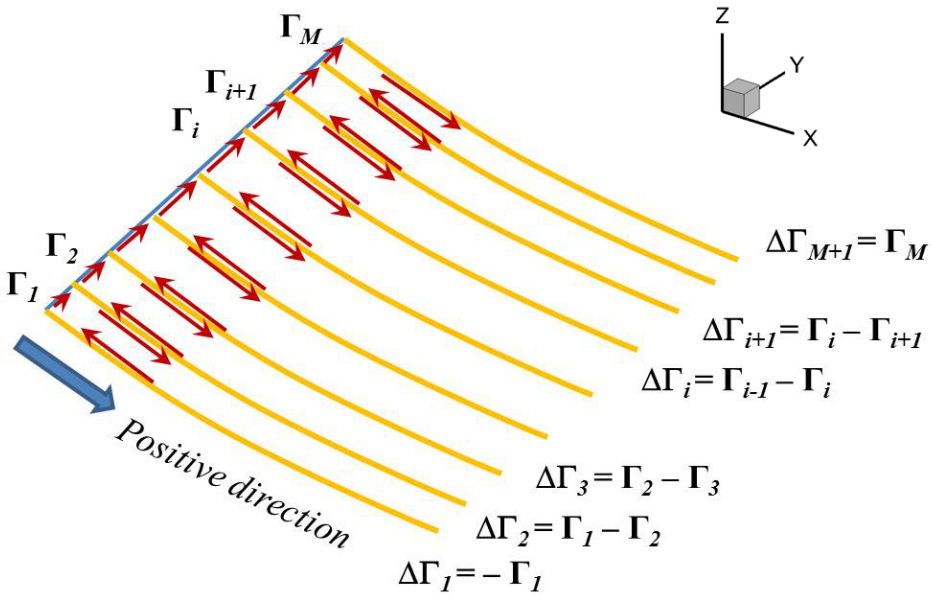

Figure 3.2: Discretization scheme for the lifting line model, where the line vortex on the key blade is represented by M horseshoe vortices (Xu, 2010 [52])

The distribution of the vortices can be performed according to different spacing strategies: in the case of *uniform spacing*, both the initial and final vortices are inset 25% of the panel length Δr; *cosine spacing* is used for most of the figures included in this thesis, since it provides higher accuracy near the tip and the hub, where changes in the circulation distribution $\Delta\Gamma$ are most significant; *half-cosine spacing* must be chosen when a hub model is included. A series of control points, where the flow parameters are calculated, is also

distributed according to the spacings described above.

3.1.3 Optimization Formulation

The optimization analysis starts with the study of one of the blades, as illustrated in Figure 3.3. The combined velocity and force diagram for a blade or length R at a given radius r is shown, with u_a^* and u_t^* representing the induced axial and tangential velocities, respectively. The induced velocities combine with the current speed V to form a new total inflow velocity V^*.

$$V^* = \sqrt{(V - u_a^*)^2 + (\omega r + u_t^*)^2} \tag{3.5}$$

This total velocity V^* forms an angle β_i with the angle of rotation, which varies as a function of r.

$$\tan \beta_i(r) = \frac{V - u_a^*}{\omega r + u_t^*} \tag{3.6}$$

To calculate the torque produced by the turbine, the pitch angle β_i is used to project the lift and drag forces (L and D respectively) generated by the flow on the blade's cross section. An expression for the differential torque dQ generated for by a length of blade dr at a distance r from the axis can be thus obtained from the force diagram.

$$dQ = [L \sin(\beta_i) dr - D \cos(\beta_i) dr] r \tag{3.7}$$

The lift and drag forces per unit span are defined as:

$$L = \rho V^* \Gamma \tag{3.8}$$

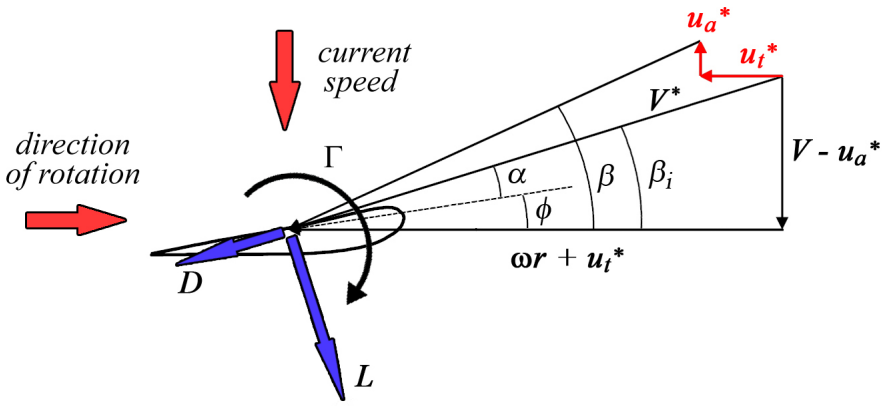

Figure 3.3: Combined velocity and force diagram on blade section at radius r, turbine case

$$D = \tfrac{1}{2}\rho(V^*)^2 c C_D \tag{3.9}$$

where Γ is the circulation at the given section, and c is the sectional chord length. The lift and drag coefficients are defined as follows:

$$C_L = \frac{L}{\frac{1}{2}\rho(V^*)^2 c} \tag{3.10}$$

$$C_D = \frac{D}{\frac{1}{2}\rho(V^*)^2 c} \tag{3.11}$$

As proposed by Falcão de Campos [13], the viscous effects are introduced into the formulation by means of a sectional drag-to-lift ratio $\kappa(r)$. The formulation for an independent drag coefficient was carried out by Zan [54], but involves some additional complexity by incorporating a non-linear term into Equation 3.21.

$$\kappa(r) = \frac{C_D(r)}{C_L(r)} = \frac{D(r)}{L(r)} \tag{3.12}$$

It it worth noting that C_D is constant for a family of airfoils regardless of the camber ratio and thus C_L, so keeping $\kappa(r)$ constant through the optimization process can be equivalent to performing chord length optimization such that $CL = \frac{2\Gamma}{V^* c}$ is constant.

The total torque Q for the turbine can thus be calculated by replacing 3.8, 3.9 and 3.11 into Equation 3.7, and integrating over the total length of the blade:

$$Q = \rho Z \int_{r_h}^{R} [V^* \Gamma \sin(\beta_i) - \kappa(r) V^* \Gamma \cos(\beta_i)] r \, dr \tag{3.13}$$

where r_h is the hub radius and Z the total number of blades in the turbine. The influence of the hub is not considered in this equation, and is treated in section 3.1.4. From Figure 3.3:

$$V^* \sin(\beta_i) = V - u_a^* \tag{3.14}$$

$$V^* \sin(\beta_i) = \omega r + u_t^* \tag{3.15}$$

The total torque is then expressed as a function of known parameters, the induced velocities along the key blade, and the circulation distribution.

$$Q = \rho Z \left[\int_{r_h}^{R} (V - u_a^*) \Gamma r \, dr - \int_{r_h}^{R} \kappa(r)(\omega r + u_t^*) \Gamma r \, dr \right] \tag{3.16}$$

We solve this equation numerically, discretizing the lifting line into M contiguous horseshoe vortices as explained in Section 3.1.2 (Kerwin et al, 1986 [21]). Equation 3.16 can then be expressed as follows:

$$Q = \rho Z \left\{ \sum_{m=1}^{M} [V - u_a^*(m)] \Gamma_m r_m \Delta r_m - \sum_{m=1}^{M} \kappa_m [\omega r_m + u_t^*(m)] \Gamma_m r_m \Delta r_m \right\} \tag{3.17}$$

Equation 3.17 can be further simplified by normalizing the parameters with respect to the current speed and the total blade radius:

$$\Delta\overline{r}_m = \frac{\Delta r_m}{R} \qquad \overline{r}_m = \frac{r_m}{R} \qquad \overline{\Gamma}_m = \frac{\Gamma_m}{VR} \tag{3.18}$$

Then:

$$Q = \rho Z V^2 R^3 \left\{ \sum_{m=1}^{M} \left[1 - \frac{u_a^*(m)}{V} \right] \overline{\Gamma}_m \overline{r}_m \Delta\overline{r}_m - \sum_{m=1}^{M} \kappa_m \left[\frac{\omega r_m}{V} + \frac{u_t^*(m)}{V} \right] \overline{\Gamma}_m \overline{r}_m \Delta\overline{r}_m \right\} \tag{3.19}$$

If κ_m is equal to zero, the second term of this equation disappears, and we are left with an expression for the no-drag inviscid case. The induced velocities are calculated at the control points according to the following:

$$\frac{u_a^*(m)}{V} = \sum_{n=1}^{M} \overline{\Gamma}_n \overline{u_a}(m,n) \qquad \frac{u_t^*(m)}{V} = \sum_{n=1}^{M} \overline{\Gamma}_n \overline{u_t}(m,n) \tag{3.20}$$

where $\overline{u_a}(m,n)$ is the axial velocity induced at the m^{th} control point by a helical horseshoe vortex surrounding the n^{th} control point. Replacing Equation 3.20 into Equation 3.19, we obtain the final expression for the turbine's torque:

$$Q = \rho Z V^2 R^3 \left\{ \sum_{m=1}^{M} \left[1 - \sum_{n=1}^{M} \overline{\Gamma}_n \overline{u_a}(m,n) \right] \overline{\Gamma}_m \overline{r}_m \Delta\overline{r}_m - \sum_{m=1}^{M} \kappa_m \left[\frac{\omega r_m}{V} + \sum_{n=1}^{M} \overline{\Gamma}_n \overline{u_t}(m,n) \right] \overline{\Gamma}_m \overline{r}_m \Delta\overline{r}_m \right\} \tag{3.21}$$

The induced velocities (axial and tangential) can be evaluated by two methods: the *induction factor method*, first proposed by Lerbs (1952) [35] and

Wrench (1957) [50], and the *numerical calculation* of the induced velocities combined with a full wake alignment procedure. Both methods are covered in detail in Section 3.3, but it can be assumed that given a wake the induced coefficients on the key blade are known. To maximize Q, we take its derivative with respect to the circulation Γ:

$$\frac{\partial Q}{\partial \overline{\Gamma}_i} = 0 \qquad i = 1, \ldots, M \tag{3.22}$$

As proposed by Zan (2008) [54], we linearize the problem by disregarding the higher order terms, which is equivalent to making the following assumption for the induced velocity coefficients:

$$\frac{\partial \overline{u_a}(m,n)}{\partial \overline{\Gamma}_n} \approx 0 \qquad \forall\ m, n \tag{3.23}$$

This linearization is typical in the case of propeller design (Kerwin et al, 1986 [21]), but has not yet been validated for turbines. An attempt has been made to extend the formulation in order to evaluate the derivatives given in Equation 3.23, with inconclusive results. The complete formulation, alternatives studied and results for a Lerbs-Wrench type approach can be found in Appendix B.

Given the assumption in Equation 3.23, the system of differential equations becomes a system of linear equations and can be solved for the circulation values in each control point:

$$\sum_{m=1}^{M} \left\{ \left[\overline{r}_i \Delta\overline{r}_i \overline{u_a}(i,m) + \overline{r}_m \Delta\overline{r}_m \overline{u_a}(m,i) + \kappa_i \overline{r}_i \Delta\overline{r}_i \overline{u_t}(i,m) + \kappa_m \overline{r}_m \Delta\overline{r}_m \overline{u_t}(m,i) \right] \overline{\Gamma}_m \right\}$$
$$= \overline{r}_i \Delta\overline{r}_i - \kappa_i \frac{\omega r_i \overline{r}_i \Delta\overline{r}_i}{V} \qquad i = 1, \ldots, M \tag{3.24}$$

Once the circulation distribution is known, the torque Q can be determined through equation 3.21. The turbine's efficiency η is equal to the power coefficient C_{pow}, and is defined as:

$$\eta = C_{pow} = \frac{Q\omega}{\frac{1}{2}\rho\pi V^3 R^2} \tag{3.25}$$

The problem is solved through an iterative algorithm detailed in Sections 3.3.1 and 3.3.2. The optimization model is used to lead the wake alignment towards the configuration associated with the maximum efficiency, and it is based on classical lifting line theory.

It is worth mentioning that this method does not follow the assumptions of classical optimization theory. Betz (1919) [5] determined that for a propeller with optimum circulation distribution in uniform inflow the induced pitch angle is constant along the radius far downstream. Lerbs (1952) [35] modified this condition in the case of non-uniform inflow. It receives the name of *Betz's Condition*, and can be written as:

$$\frac{\tan(\beta)(r)}{\tan(\beta_i)(r)} = \text{constant} \tag{3.26}$$

This assumption has been extended to turbines by Falcão de Campos [13]. Section 4 explores whether the LLOPT-LW and LLOPT-FWA models follow Betz's Condition.

As mentioned in Section 3.1.3, the linearization assumption given by Equation 3.23 has not been validated. An attempt to extend the formulation

attempt to include those terms is included in Appendix B, based on the Lerbs-Wrench formulas. Section 4.1.1 shows that this limits the efficiency to no more than 50% for high-TSR, high-Z turbine parameters.

It can be proven that the optimization solution, for that combination of design parameters, tends towards a constant loading distribution. Thus we can try to derive the optimization formulation for a hubless constant-circulation turbine with infinite number of blades, a model akin to the actuator disk theory described in Section 3.1.1. This formulation was carried out by Kinnas in private correspondence (2012, not published), and is included in full in Appendix A.

3.1.4 Inclusion of Hub Effects

The formulation presented in Section 3.1.3 ignores the presence of the hub. As a consequence, the circulation distributions obtained goes to zero at both the hub and the tip, inducing roll-up at the hub once the wake is aligned as is explained in Section 3.3.2. In a boundary element method, the hub geometry can be modeled along with the blade, but for the lifting line model the method proposed by Kerwin and Hadler [22] is used. Alternatively, the hub can also be modeled by a panel method with the blade modeled as a lifting line (Kinnas and Coney, 1992 [26]).

The effects of the hub are included through an image model. For every vortex located at radius r_v, an image vortex r_{image} is created at the position determined by Equation 3.27, thus producing a null total velocity on the hub

surface.

$$r_{image} = \frac{r_h^2}{r_v} \tag{3.27}$$

This result is illustrated in Figure 3.4, which exemplifies the image model for the case of a 2D point vortex (Kerwin and Hadler, 2010 [22]). Numerical calculations show that this model works well for helical semi-infinite vortex as the ones used in the Lerbs-Wrench model (Section 3.3.1). The pitch of the image is taken to be equal to the pitch of the vortex, and thus the pitch angle is given by:

$$\tan(\beta_i^{image}) = \frac{r_v \ \tan(\beta_i)}{r_{image}} \tag{3.28}$$

where β_i^{image} is the pitch angle of the image vortex. In the case of full wake alignment (Section 3.3.2), it is necessary to find the image of the discretized wake. Equation 3.27 is used for every vortex lattice node, where r_v represents in this case the minimum distance between the node and an infinite cylinder of radius r_h coincident with the x axis.

When the hub model is included, the total induced coefficients used in the optimization formulas are a combination of the original wakes and the image wakes:

$$\overline{u_{a.total}}(m,n) = \overline{u_a}(m,n) + \overline{u_{a.image}}(m,n) \tag{3.29}$$

$$\overline{u_{t.total}}(m,n) = \overline{u_t}(m,n) + \overline{u_{t.image}}(m,n) \tag{3.30}$$

If the hub effects are included in the formulation, a half-cosine distribution should be selected for the control points. The use of other distributions can result in numerical instability in the zone close to the hub.

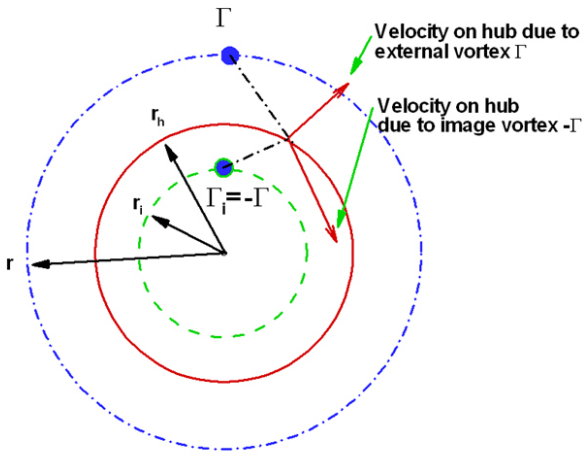

Figure 3.4: Image model for a 2D point vortex in a circle of radius r_h (Kerwin and Hadler, 2010 [22])

3.1.5 Glauert Series Representation

As is shown in Section 4.1.2, the LLOPT-FWA model produces in general jagged circulation distributions that present a spike near the tip of the blade. This singular behavior increases as TSR and Z grow, and as a consequence, most of the figures in this thesis are limited to two- or three-bladed rotors. To solve this problem, constraints must be imposed on the wake model or the circulation distribution.

The latter can be achieved by representing the circulation as a series of arbitrary functions, which subsequently is constrained as detailed on Section 3.1.7. One such possible representation is achieved by the use of the so-called Glauert series (Glauert, 1947 [16]), which describes the circulation as a sum of sines. First we need to carry out a coordinate transformation to a new

variable, $\tilde{r}$. In the case of a hub-less turbine, the transformation is given by Equation 3.31.

$$\tilde{r} = \arccos\left[\frac{(R + r_h) - 2\,r}{R - r_h}\right] \tag{3.31}$$

For the case of a turbine with a hub, the transformation is modified in order to ensure that the circulation distribution does not go to zero at the hub. The control points should be placed according to a half-cosine distribution, as in the original formulation.

$$\tilde{r} = \arccos\left[\frac{r - r_h}{r_h - R}\right] \tag{3.32}$$

The expression for the circulation is given in Equation 3.33. NG represents the number of modes that are chosen to represent the optimum distribution. As the rotational speed and the number of blades increase, more modes are necessary. Section 4.1.2 explores the effects of choosing different number of modes.

$$\overline{\Gamma}(r) = \sum_{k=1}^{NG} a_k\ \sin(k\tilde{r}) \tag{3.33}$$

The use of this function changes the optimization formulation described in Section 3.1.3. Replacing Equation 3.33 into Equation 3.19, we obtain:

$$Q = \rho Z V^2 R^3 \left\{\sum_{m=1}^{M}\left[1 - \frac{u_a^*(m)}{V}\right]\left[\sum_{k=1}^{NG} a_k\ \sin(k\tilde{r}_m)\right]\overline{r}_m \Delta\overline{r}_m\right\} \tag{3.34}$$

To maximize the torque Q generated we differentiate Equation 3.34 with respect to the coefficients a_k.

$$\frac{\partial Q}{\partial a_k} = 0 \qquad k = 1, \ldots, NG \tag{3.35}$$

This results in the following set of $NG \times NG$ equations:

$$\sum_{t=1}^{NG} \left\{ \sum_{i=1}^{M} \sin(t\widetilde{r_i}) \overline{r}_i \Delta \overline{r}_i \sum_{j=1}^{M} \sin(k\tilde{r}_j) \overline{u_a}(i,j) + \sum_{i=1}^{M} \sin(k\tilde{r}_i) \overline{r}_i \Delta \overline{r}_i \sum_{j=1}^{M} \sin(t\tilde{r}_j) \overline{u_a}(i,j) \right\} a_t = \sum_{i=1}^{M} \sin(k\tilde{r}_i) \quad (3.36)$$

3.1.6 Polynomial Representation

Another possible representation for the circulation distribution is through the use of polynomials. It can be proven that for the hub-less turbine case the circulation distribution behaves as the square root of the distance as it approaches the tip and the hub. In order to capture this behavior, the polynomials are multiplied by square root functions as shown in Equation 3.37. In this case NG is the order of the polynomial between parenthesis.

$$\overline{\Gamma}(r) = \sqrt{R - r}\sqrt{r - r_h} \left(a_0 + a_1\, r + a_2\, r^2 + \ldots + a_{NG}\, r^{NG} \right) \quad (3.37)$$

Given this new function we carry out as in Section 3.1.5, maximizing the torque according to Equation 3.35. The set of $NG \times NG$ linear equations can be solved for the unknown a_k coefficients that produce the optimum efficiency.

$$\sum_{t=1}^{NG}\left\{\sum_{i=1}^{M}\sqrt{R-r_i}\sqrt{r_i-r_h}\,r_i^{k-1}\sum_{j=1}^{M}\sqrt{R-r_j}\sqrt{r_j-r_h}\,r_j^{t-1}\,\overline{u_a}(i,j)\right.$$
$$\left.+\sqrt{R-r_i}\sqrt{r_i-r_h}\,r_i^{t-1}\sum_{j=1}^{M}\sqrt{R-r_j}\sqrt{r_j-r_h}\,r_j^{k-1}\,\overline{u_a}(i,j)\right\}a_t$$
$$=\sum_{i=1}^{M}\sqrt{R-r_i}\sqrt{r_i-r_h}\,r_i^{k-1}\qquad k=1,\ldots,NG \quad (3.38)$$

In the case when the hub image model is included, the formulation remains unchanged, but the square root singularity at the hub ($\sqrt{r_h - r}$) must be removed. The same treatment should be applied in the case of a duct with zero gap.

3.1.7 Constrained Optimization

Based on the results for LLOPT-LW, actuator disk theory and results presented by other specialists in turbine optimization, it is expected that the optimal circulation distributions will "flatten" as TSR and Z increase. LLOPT-FWA, however, presents an increase of the loading near the tip incompatible with this. Furthermore, it is presumed that a hydrodynamically and structurally optimal turbine blade will result in smooth circulations. Non-smooth circulations produce uneven blade surfaces when used as input on the blade design methodology detailed in section 3.4 (see Figure 3.18).

A constrained optimization model is thus proposed, looking to produce smoother circulation distributions while retaining the full wake alignment

model. The first constraint set determines that the second derivative of $\Gamma(r)$ must not change signs on the blade, thus avoiding inflection points.

$$\frac{d^2\overline{\Gamma}}{dr^2} \geq 0 \tag{3.39}$$

Figure 3.5 presents the results obtained for the inviscid case $Z = 2$, $TSR = 4$. It can be seen that constraining only the curvature results in circulation distributions that are heavily loaded at the tip. To prevent this, an additional constraint can be set: the first derivative of the function at the midpoint of the blade (r_{mp}) must match that of the unconstrained LLOPT-FWA. This constraint is somewhat arbitrary, but it produces efficiencies that fulfill the condition of reaching Betz's limit as TSR increases and distributes the load evenly along the blade.

To solve the constrained optimization problem we use a *Weighted Least Squares* (WLS) approach (see Myers, 2000 [42]). $M + 1$ new equations can be set by differentiating the circulation function given in Equation 3.37 with respect to r and evaluating the resulting expression at the control points:

$$\frac{d^2\overline{\Gamma}}{dr^2}(r_i) = \sum_{t=1}^{NG} a_t \, f_t^1(R, r_h, r_i) \geq 0 \qquad\qquad i = 1, \ldots, M \tag{3.40}$$

$$\frac{d\overline{\Gamma}}{dr}(r_{mp}) = \sum_{t=1}^{NG} a_t \, f_t^2(R, r_{mp}) = \frac{d\overline{\Gamma}_{unc}}{dr}(r_{mp}) \tag{3.41}$$

where f_t^1 and f_t^2 are functions that can be calculated analytically and depend only on the length of the blade and the location of the control points. Adding

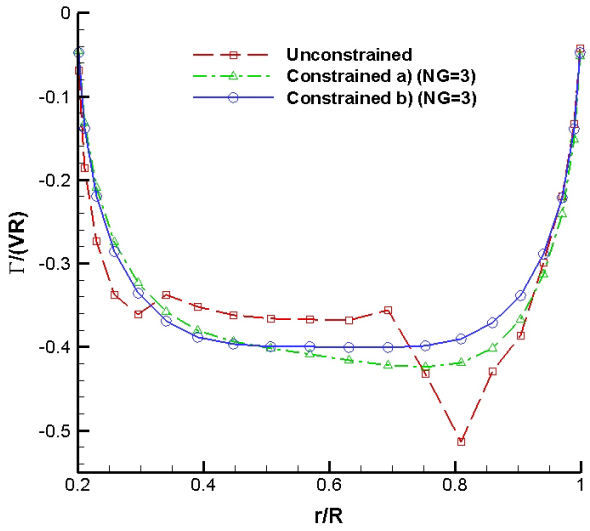

Figure 3.5: Two possible constrained optimization models: a) only imposing an inequality constraint on the curvature; b) adding a constraint on the slope ($Z = 2, TSR = 4$). Corresponding efficiencies: 1) unconstrained = 44.56%; 2) constrained curvature = 44.38%; 3) constrained curvature and slope = 44.56%. See Table 4.4.

these new equation to the existing system of equations given by Equation 3.38 leads to an over-determined linear system of equations, where the new equations can be thought of as penalty functions.

We can write the complete system of equations in matrix form as fol-

lows:

$$\overbrace{\begin{bmatrix} LHS_{1,1} & LHS_{1,2} & \cdots & LHS_{1,NG} \\ LHS_{2,1} & LHS_{2,2} & \cdots & LHS_{2,NG} \\ \vdots & \vdots & \ddots & \vdots \\ LHS_{NG,1} & LHS_{NG,2} & \cdots & LHS_{NG,NG} \\ f_1^1(r_1) & f_2^1(r_1) & \cdots & f_{NG}^1(r_1) \\ f_1^1(r_2) & f_2^1(r_2) & \cdots & f_{NG}^1(r_2) \\ \vdots & \vdots & \ddots & \vdots \\ f_1^1(r_M) & f_2^1(r_M) & \cdots & f_{NG}^1(r_M) \\ f_1^2(r_{mp}) & f_2^2(r_{mp}) & \cdots & f_{NG}^2(r_{mp}) \end{bmatrix}}^{\mathbf{M}} \overbrace{\begin{bmatrix} a_1 \\ a_2 \\ \vdots \\ a_{NG} \end{bmatrix}}^{\mathbf{a}} = \overbrace{\begin{bmatrix} RHS_1 \\ RHS_2 \\ \vdots \\ RHS_{NG} \\ 0 \\ 0 \\ \vdots \\ 0 \\ \frac{d\bar{\Gamma}_{unc}}{dr}(r_{mp}) \end{bmatrix}}^{\mathbf{b}} \tag{3.42}$$

where LHS and RHS are the left hand side and right hand side terms of Equations 3.35 and 3.38. In the case the constraint on the slope is not included, the last row in the matrix should be removed. We define the weighting matrix $\mathbf{W}$ as a diagonal matrix with weights w_{ii} initially determined as:

$$w_{ii} = \begin{cases} 1 & \text{if } i \leq NG, \\ 0 & \text{if } NG < i \leq NG + (M+1), \end{cases}$$

That is, the initial weights w_{ii} corresponding to the constraints are zero, so the WLS method recovers the original unconstrained solution. The constraints are checked for compliance, and in the case they are not met the corresponding weights are increased iteratively. The constrained solution $\hat{\mathbf{a}}$ can be found through the use of Weighted Least Squares theory as a function of the matrices defined above.

$$\mathbf{WMa} = \mathbf{Wb} \tag{3.43}$$

The normal equations can then be written as:

$$(\mathbf{M}^T\mathbf{WM})\hat{\mathbf{a}} = (\mathbf{M}^T\mathbf{W})\mathbf{b} \tag{3.44}$$

The solution can be found by inversing the $(\mathbf{M}^T\mathbf{WM})$ matrix. We will use instead the QR orthogonal decomposition method, in which the weighted matrix $\mathbf{WM}$ is decomposed into two matrices $\mathbf{Q}$ and $\mathbf{R}$ such that $\mathbf{WM} = \mathbf{QR}$. $\mathbf{Q}$ is an $(NG+M+1)\times(NG+M+1)$ orthogonal matrix and $\mathbf{R}$ is an $(NG+M+1)\times NG$ matrix which is partitioned into an $NG \times NG$ upper triangular block $\mathbf{R_n}$ and a $(M+1) \times NG$ zero block $\mathbf{0}$, such that:

$$\mathbf{R} = \begin{bmatrix} \mathbf{R}_n \\ \mathbf{0} \end{bmatrix} \tag{3.45}$$

We multiply Equation 3.43 by $(\mathbf{WM})^T$ and operate to obtain an expression for the solution in terms of $\mathbf{Q}$ and $\mathbf{R}$. Since $\mathbf{Q}$ is an orthogonal matrix, $\mathbf{Q}^{-1} = \mathbf{Q}^T$, then:

$$\begin{aligned} (\mathbf{WM})^T\mathbf{WM}\hat{\mathbf{a}} &= (\mathbf{WM})^T\mathbf{Wb} \\ \mathbf{R}^T\mathbf{Q}^T\mathbf{QR}\hat{\mathbf{a}} &= \mathbf{R}^T\mathbf{Q}^T\mathbf{Wb} \\ \mathbf{R}^T\mathbf{R}\hat{\mathbf{a}} &= \mathbf{R}^T\mathbf{Q}^T\mathbf{Wb} \\ \mathbf{R}\hat{\mathbf{a}} &= \mathbf{Q}^T\mathbf{Wb} \end{aligned}$$

Thereforme $\hat{\mathbf{a}}$ can be found by solving the linear system of equations:

$$\mathbf{R}_n\hat{\mathbf{a}} = (\mathbf{Q}^T\mathbf{Wb})_n \tag{3.46}$$

This formulation is carried out in detail in Gulliksson and Wedin (1992) [17]. The open-source weighted least squares solver included in LINPACK (www.netlib.org/linpack/) was used. The weight increase depends on the number of modes NG chosen, and should be chosen carefully.

The main advantage of the constrained optimization model is that it allows us to obtained smooth circulations that satisfy the optimization equations while still using the Full Wake Alignment routine. This results in more realistic wake shapes, as mentioned previously, with expansion and roll up.

This constrained methodology was only developed for the case of polynomial representation as described in Section 3.1.6. It can be extended to both Glauert series representation (Section 3.1.5) or to discrete optimization (Section 3.1.3) through the use of numerical derivatives.

3.2 Propellers

3.2.1 Actuator Disk Theory

As in the case of turbines covered in Section 3.1.1, the simplest ideal representation for a propeller is a permeable actuator disk with no thickness. Kerwin and Hadler (2010) [22] uses actuator disk theory to relate the thrust T generated to the increase in static pressure through the disk Δp. The theory is summarized next, for completeness.

$$T = \pi R^2 \Delta p \tag{3.47}$$

Figure 3.6 shows a schematic of the actuator disk model for the case of a propeller, where V is the inflow velocity, α is the coefficient of velocity increment immediately downstream from the disk and u_w is the increment velocity in the stream tube far downstream.

Using Bernoulli's equation between a point far upstream and another

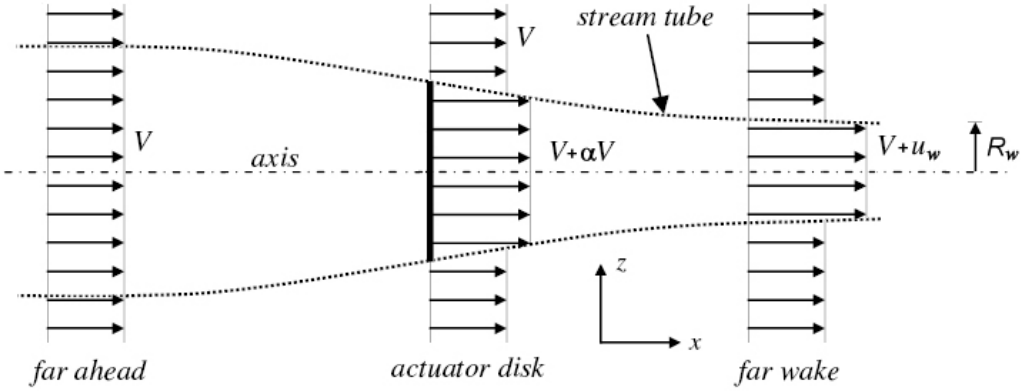

Figure 3.6: Schematic of actuator disk model, propeller case

far downstream the pressure increase can be expressed in terms of the total velocity. Replacing in Equation 3.47 a new equation for the thrust is found.

$$T = \pi R^2 \rho u_w \left(V + \frac{u_w}{2} \right) \tag{3.48}$$

Using the definition for the thrust coefficient C_T given in Equation 3.65 and operating, the following relation can be found:

$$\frac{u_w}{V} = \frac{1 - \sqrt{1 + C_T}}{2} \tag{3.49}$$

The efficiency of an actuator disk can be determined as the ratio between the useful work done W and the total energy used. We define δx as the total distance the disk will move in a time interval δt, seen from the perspective of a fixed coordinate system. The work will then be defined as $W = T\delta x$, and the total kinetic energy contained in the flow far downstream relative to an outside observer will be called E. Using the conservation of energy principle,

we write an expression for the efficiency:

$$\eta = \frac{T\delta x}{T\delta x + E} = \frac{T}{T + E/\delta x} \tag{3.50}$$

The increase in kinetic energy E is the kinetic energy (relative to an outside observer) contained in a stream tube of radius R_w, the radius of the slipstream far downstream. Obtaining an expression for R_w through the use of the conservation of mass principle, E can be written in terms of known parameters.

$$\frac{E}{\delta x} = \frac{1}{2}\rho u_w^2 \pi R^2 \frac{V + u_w/2}{V} \tag{3.51}$$

Replacing Equations 3.48 and 3.51 into Equation 3.50 we can then express the actuator disk's efficiency as a function of the C_T coefficient.

$$\eta = \frac{1}{1 + \frac{u_w}{2V}} = \frac{2}{1 + \sqrt{1 + C_T}} \tag{3.52}$$

The complete derivation of this equation can be found in Kerwin and Hadler (2010) [22]. As in the case of turbines, this value will be used as an upper limit for our lifting line model. As the advance coefficient J goes to zero and the number of blades Z increases, the efficiency obtained for a given C_T must approach the value given by Equation 3.52 asymptotically.

3.2.2 Optimization Formulation

The methodology that is used in this Section follows closely the optimization procedure developed by Kerwin (1996) [20], and is very similar to

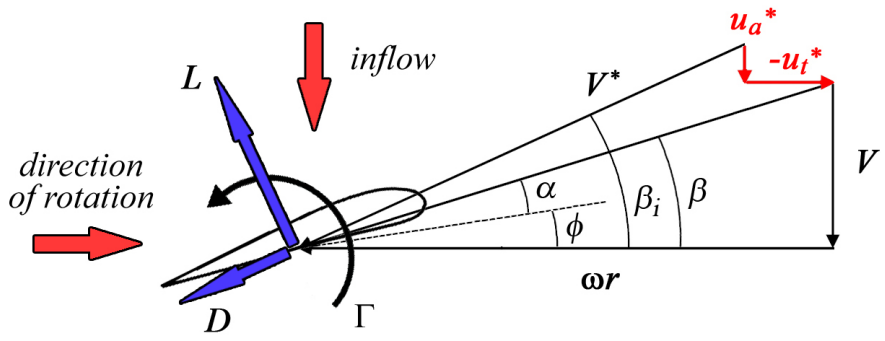

Figure 3.7: Combined velocity and force diagram on blade section at radius r, propeller case

the one developed for turbines in Section 3.1.3. The analysis starts with the study of one of the propeller blades, as illustrated in Figure 3.7.

The definition for the total inflow velocity V^* and the pitch angle of the disturbed flow β_i change slightly from those defined in the case of turbines, according to the new velocity diagram.

$$V^* = \sqrt{(V + u_a^*)^2 + (\omega r + u_t^*)^2} \tag{3.53}$$

$$\tan \beta_i(r) = \frac{V + u_a^*}{\omega r + u_t^*} \tag{3.54}$$

When optimizing a turbine the thrust generated T is not of particular interest. However, it is customary in the optimization and design of propellers to have the thrust as an input parameter, and thus it has to be included in the formulation. We use the angle β_i to project the lift and drag forces onto the rotational plane. The expressions for the differential torque dQ and the

differential thrust dT are:

$$dQ = (L\sin(\beta_i)dr + D\cos(\beta_i)dr)r \tag{3.55}$$

$$dT = L\cos(\beta_i)dr - D\sin(\beta_i)dr \tag{3.56}$$

We integrate from the start of the blade (hub radius r_h) to its total length R, and assuming as before that the drag force is proportional to the lift ($D = \kappa L$), the expressions for the total torque and thrust are obtained.

$$Q = \rho Z \left[\int_{r_h}^{R} (V + u_a^*)\Gamma r\, dr + \int_{r_h}^{R} \kappa(r)(\omega r + u_t^*)\Gamma r\, dr\right] \tag{3.57}$$

$$T = \rho Z \left[\int_{r_h}^{R} (\omega r + u_t^*)\Gamma\, dr - \int_{r_h}^{R} \kappa(r)(V + u_a^*)\Gamma\, dr\right] \tag{3.58}$$

These integrals are solved numerically, discretizing the bound vortex into M horseshoe vortices as detailed in Section 3.1.2. The discretized equations are normalized according to Equation 3.18.

$$Q = \rho Z V^2 R^3 \left\{\sum_{m=1}^{M} \left[1 + \frac{u_a^*(m)}{V}\right] \overline{\Gamma}_m \overline{r}_m \Delta\overline{r}_m + \sum_{m=1}^{M} \kappa_m \left[\frac{\omega r_m}{V} + \frac{u_t^*(m)}{V}\right] \overline{\Gamma}_m \overline{r}_m \Delta\overline{r}_m\right\} \tag{3.59}$$

$$T = \rho Z V^2 R^2 \left\{\sum_{m=1}^{M} \left[\frac{\omega r_m}{V} + \frac{u_t^*(m)}{V}\right] \overline{\Gamma}_m \Delta\overline{r}_m - \sum_{m=1}^{M} \kappa_m \left[1 + \frac{u_a^*(m)}{V}\right] \overline{\Gamma}_m \Delta\overline{r}_m\right\} \tag{3.60}$$

The induced velocities are expressed as a function of the induced axial and tangential coefficients for unit strength vortices, as shown in Equation 3.20. This allows us to express the equations in terms of only one unknown, the circulation distribution $\Gamma(r)$.

We need to find the circulation values $\overline{\Gamma}_1, \ldots, \overline{\Gamma}_M$ that minimize the torque Q constraint to a given thrust T_0, so we use a variational optimization approach. In order to meet the constraint set by 3.60, we form the quantity $H = Q + \lambda T$ and differentiate it with respect to the unknown circulation values.

$$\frac{\partial H}{\partial \overline{\Gamma}_i} = 0 \qquad i = 1, \ldots, M \tag{3.61}$$

The assumption presented in Equation 3.23 is also adopted in this model. This is an approximation that is assumed to be accurate for propellers, but has not yet been validated. The Lagrange multiplier λ is an additional unknown which must also be solved. Carrying out the differentiation for the *inviscid case* and adding an equation for the known torque T_0 we obtain a set of $M + 1$ equations:

$$R \sum_{m=1}^{M} \left\{ \left[\overline{r}_i \Delta\overline{r}_i \overline{u_a}(i,m) + \overline{r}_m \Delta\overline{r}_m \overline{u_a}(m,i) + \hat{\lambda} \left(\Delta\overline{r}_i \overline{u_t}(i,m) + \Delta\overline{r}_m \overline{u_t}(m,i) \right) \right] \overline{\Gamma}_m \right\} + \lambda \frac{\omega r_i \Delta\overline{r}_i}{V} = -R\overline{r}_i \Delta\overline{r}_i \qquad i = 1, \ldots, M \tag{3.62}$$

$$T_0 = \rho Z V^2 R^2 \left\{ \sum_{m=1}^{M} \left[\frac{\omega r_m}{V} + \frac{u_t^*(m)}{V} \right] \overline{\Gamma}_m \Delta\overline{r}_m \right\} \tag{3.63}$$

This is a non-linear system of equations, both in $\hat{\lambda}$ and in $u_t^*(m)$ in Equation 3.63. Following the procedure suggested by Kerwin [20], we linearize the system by assuming that and the induced tangential velocities in Equation 3.63 to be known, and reaching a solution iteratively.

The torque and thrust forces can be non-dimensionalized with respect to either the nominal rotational velocity (nR), which results in the K_T and K_Q coefficients, or to the ship speed V, resulting in the C_T and C_Q coefficients.

$$K_T = \frac{T}{16\rho n^2 R^4} \qquad K_Q = \frac{Q}{32\rho n^2 R^5} \tag{3.64}$$

$$C_T = \frac{T}{\frac{1}{2}\rho\pi V^2 R^2} \qquad C_Q = \frac{Q}{\frac{1}{2}\rho\pi V^2 R^3} \tag{3.65}$$

The efficiency of the propeller can be defined as a function of these coefficients. Both definitions presented in equation 3.66 are equivalent.

$$\eta = \frac{K_T}{K_Q}\frac{J}{2\pi} = \frac{C_T}{C_Q}\frac{J}{\pi} \tag{3.66}$$

3.2.3 Inclusion of Hub Effects

The influence of the hub can be included in the optimization formulation through the use of an image model, as explained in Section 3.1.4. Once again, a half-cosine distribution is chosen for the control points, since it has been determined that it improves the accuracy of the results. For details on the image model used, please refer to Section 3.1.4.

3.3 Wake Models

3.3.1 Lerbs-Wrench Model

The linear systems described in Sections 3.1.3 and 3.2.2, whose solution results in an optimum circulation distribution along the key blade, depends on the calculation of the corresponding induced coefficients. Once the shape of the rotor's wake is known, these coefficients can be calculated through the Biot-Savart law, which describes the velocity induced by an arbitrary 3D vortex line on a given point P.

$$\vec{V_P} = \frac{\Gamma}{4\pi} \int \frac{\vec{s} \times \vec{r}_P}{r_P^3} \, dl \tag{3.67}$$

where $\vec{s}$ is a unit vector tangent to the vortex line, $\vec{r}_P$ represents the distance between the point P and the vortex, Γ is the vortex strength, and dl represents a segment of the vortex of differential length. If we assume that the vortex forms a semi-infinite helix of constant pitch, this integral can be simplified to the asymptotic formulas proposed by Lerbs (1952) [35] and Wrench (1957) [50]. The formulas are functions of the pitch angle of the wake β_w, and calculate the velocity induced at radius r_c (control point) on the key blade by a set of Z unit-strength, radially-symmetrical helical vortices shed at radius r_v. The formula used thus depends on the distance between the control and vortex points. For a control point m and a vortex n, the induced velocities are given by the following equations (Lerbs, 1952 [35] and Wrench, [50] 1957):

For $r_c < r_v$:

$$\overline{u_a}^*(m,n) = \overline{u_a}(r_c, r_v) = \frac{Z}{4\pi r_c}(y - 2Zyy_0F_1) \tag{3.68}$$

$$\overline{u_t}^*(m,n) = \overline{u_t}(r_c, r_v) = \frac{Z^2}{2\pi r_c}(y_0 F_1) \tag{3.69}$$

For $r_c > r_v$:

$$\overline{u_a}^*(m,n) = \overline{u_a}(r_c, r_v) = \frac{Z^2}{2\pi r_c}(y y_0 F_2) \tag{3.70}$$

$$\overline{u_t}^*(m,n) = \overline{u_t}(r_c, r_v) = \frac{Z}{4\pi r_c}(1 - 2Z y_0 F_2) \tag{3.71}$$

Where:

$$F_1 \approx \frac{-1}{2Z y_0}\left(\frac{1+y_0^2}{1+y^2}\right)^{0.25}\left\{\frac{U}{1-U} + \frac{1}{24Z}\left[\frac{9y_0^2+2}{(1+y_0^2)^{1.5}} + \frac{3y^2-2}{(1+y^2)^{1.5}}\right]\ln\left(\frac{1}{1-U}\right)\right\}$$

$$F_2 \approx \frac{-1}{2Z y_0}\left(\frac{1+y_0^2}{1+y^2}\right)^{0.25}\left\{\frac{1}{U-1} - \frac{1}{24Z}\left[\frac{9y_0^2+2}{(1+y_0^2)^{1.5}} + \frac{3y^2-2}{(1+y^2)^{1.5}}\right]\ln\left(\frac{U}{U-1}\right)\right\}$$

$$U = \left[\frac{y_0\left(\sqrt{1+y^2}-1\right)}{y\left(\sqrt{1+y_0^2}-1\right)} exp\left(\sqrt{1+y^2} - \sqrt{1+y_0^2}\right)\right]^Z$$

$$y = \frac{r_c}{r_v \tan\beta_w} \qquad y_0 = \frac{1}{\tan\beta_w}$$

The induced coefficients for a horseshoe vortex can then be obtained by adding the effects of the line vortices that form it. Since the distance between the control point and the vortex that forms the lifting line is zero, it does not affect the results. The two remaining semi-infinite vortices have the same strength Γ_n, but opposite directions and thus opposite signs. The induced coefficients used in the optimization formulation are then:

$$\overline{u_a}(m,n) = \overline{u_a}^*(m,n+1) - \overline{u_a}^*(m,n) \tag{3.72}$$

$$\overline{u_t}(m,n) = \overline{u_t}^*(m,n+1) - \overline{u_t}^*(m,n) \tag{3.73}$$

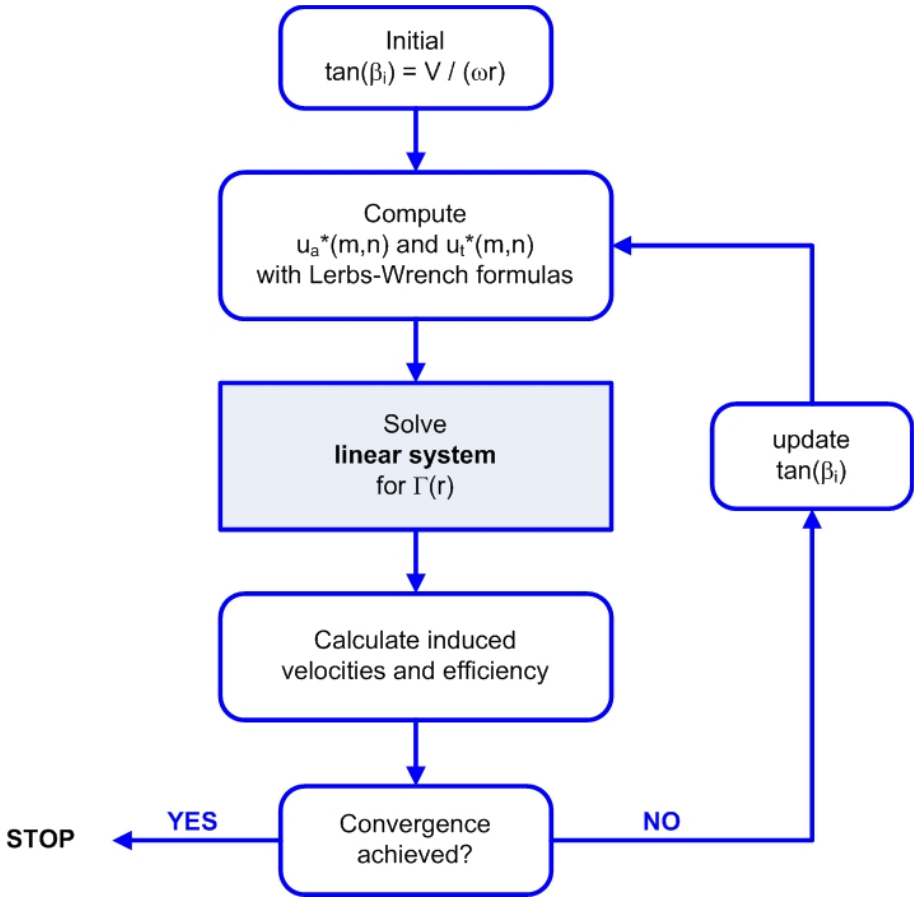

Figure 3.8: Flowchart of Lerbs-Wrench algorithm (LLOPT-LW)

As explained in Section 3.1.2, the wake generated by the lifting line is discretized into M horseshoe vortices. We can calculate the induced velocities on a given control point P by considering the effect on said point of all M vortices, and adding them. The Lerbs-Wrench formulas are used, with the additional assumption that the pitch angle of the wake β_w is equal to the pitch angle of the total induced velocity at the blade β_i. This assumption

carries the name *moderately loaded propeller theory*, as presented in Kerwin and Hadler (2010) [22].

The wake can then be aligned by iterating with respect to the pitch angle in order to reach the alignment angle that produces the optimum circulation, as originally proposed by Zan (2008) [22]. This code is called Lifting Line Optimization using Lerbs-Wrench formulas or *LLOPT-LW*, and its algorithm is shown in Figure 3.8.

3.3.2 Wake Alignment Model

The use of the Lerbs-Wrench formulas and the moderately loaded propeller assumption constrain the shape of the wake to those that can be formed by constant-pitch helical vortices, thus limiting the maximum efficiency that can be obtained through the LLOPT-LW algorithm. In order to evaluate the influence of a more realistic wake shape, a *Full Wake Alignment* model was adopted. It is based on the pseudounsteady alignment approach developed by Tian and Kinnas (2012) [48] within the framework of PROPCAV, a low-order panel code. As the TSR increases, the pitch of the wake shed from the turbines blade decreases. This might cause the wake shed from one of the blades to be close to the subsequent blade, affecting its loading and thus the efficiency of the turbine as a whole. The interaction between the wake and the inflow near the tip causes the wake to abandon its helicoidal shape, and expansion and roll up take place in the case of turbine optimization (contraction is expected in propeller optimization).

For a given aligned wake surface, the induced coefficients at the control points on the key blade can be calculated by the Biot-Savart law (Equation 3.67). The induced coefficients are a function then of the relative position of the wake panel (vortex) and of the control point (CP). The optimization formulation presented in Sections 3.1.3 and 3.2.2 can be used to calculate the associated circulation distribution, which determines the strength $\Delta\Gamma$ of the free vortices that form the wake, as illustrated in Figure 3.2. Once the strength of the vortices is updated, the alignment scheme can be used iteratively to modify the wake accordingly. This code is called Lifting Line Optimization using Full Wake Alignment or *LLOPT-FWA*, and its algorithm is shown in Figure 3.9.

In a general case, the resulting induced velocities calculated on each control point have projections in all three coordinates. To obtain the axial and tangential induced velocities used in the equations for the torque it is necessary to find the components of the induced velocity vector in those directions. The results by Kerwin and Hadler (2010) [22] for the velocity induced by a straight vortex segment is used, a basic application of the Biot-Savart law. The geometry of the wake has been discretized into a lattice of concentrated vortices, thus allowing us to calculate the influence of the entire wake as the sum of the influences of each panel. The analysis is developed for a given a vortex segment coinciding with the x axis and a point P on the y axis (Figure 3.10). If the segment and the line do not meet these assumptions, a coordinate transformation must be used, and the resulting induced velocity

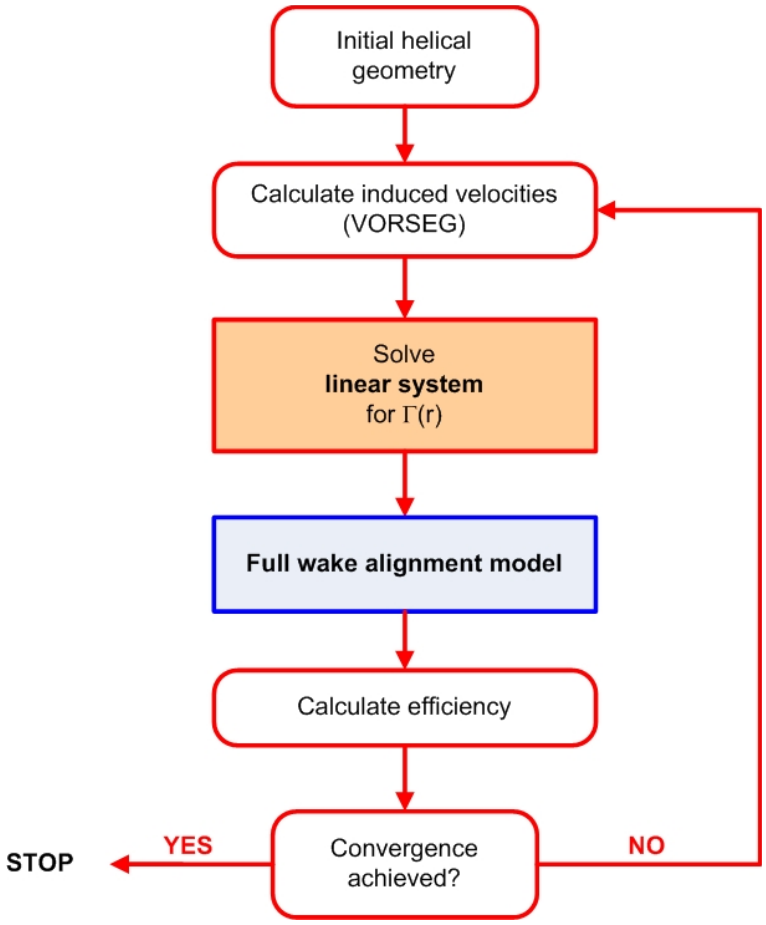

Figure 3.9: Flowchart of Full Wake Alignment algorithm (LLOPT-FWA)

must be transformed back into the original coordinate system. The VORSEG subroutine used calculates the velocities induced by every wake segment on the chosen control point with respect to the x, y and z coordinates. The final induced velocities are found by adding the results for every segment that forms the trailing wake.

The vector $s = (1, 0, 0)$ and $r = (-\zeta, y, 0)$ can then be inserted into the

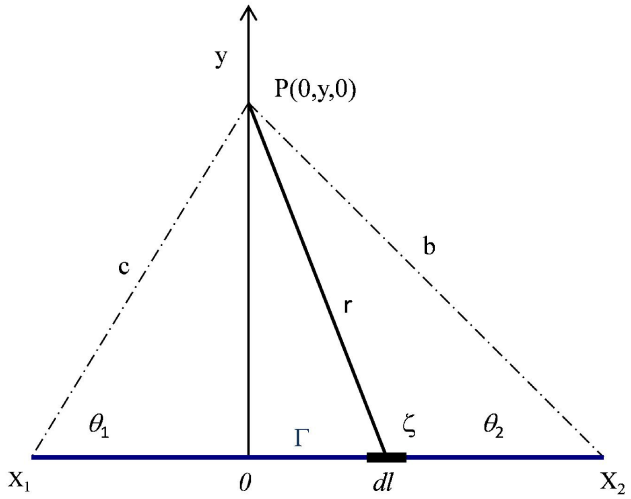

Figure 3.10: Velocity induced by a vortex segment $X1 - X2$ of strength Γ on a point P (Kerwin and Hadler, 2010 [22])

Biot-Savart law, which shows that the u and v components of the velocity are zero, and the only remaining velocity component is w. It can then be shown that:

$$w(y) = \frac{\Gamma}{4\pi}\left(\frac{x_2}{b} - \frac{x_1}{c}\right) \tag{3.74}$$

Where $b = \sqrt{x_2^2 + y^2}$ and $c = \sqrt{x_1^2 + y^2}$. The induced velocity w can also be expressed as a function of the angles θ_1 and θ_2.

$$w(y) = \frac{\Gamma}{4\pi y}\left(\cos\theta_2 + \cos\theta_1\right) \tag{3.75}$$

The total induced velocity coefficients $\overline{u_a}(m,n)$ and $\overline{u_t}(m,n)$ are thus the sum of the induced velocities w on the control point m for every segment

of the wake in the streamwise direction that corresponds to the vortex position n, for all Z turbine blades. The wake geometry depends on three basic geometrical parameters: the number of panels in the spanwise direction NRW, which must be equal to the number of M horseshoe vortices chosen previously; the number of panels in the streamwise direction MRW , which determine the total wake length, and the time step between panels th, which determines a representative grid size in the streamwise direction.

In the present model, the wake alignment is performed iteratively by updating the circulation after each iteration. This is necessary in order to ensure a stable progression towards the optimum point, and the iterative process ends when the velocity vectors induced on the wake are tangential to the ensuing wake geometry. Figure 3.11 illustrates the process, presenting the final result in which all the velocity vectors have been properly aligned.

The inclusion of a realistic wake alignment model creates complex wake geometries which can result in singular behavior near the hub and in particular the tip of the blades. As the TSR and the number of blades increase, the distance between the wake surfaces is reduced, and these effects are increased greatly. Solutions to this problem can be attempted by imposing constraints either on the optimization formulation, as explained in Section 3.1.7, or on the wake alignment procedure. The latter can be achieved through the the annulment of the radial component of the induced velocities in the wake ($U_r = 0$). This has the net result of preserving the overall shape of the wake surface, but avoiding both expansion and roll up in the wake. Tests have shown that

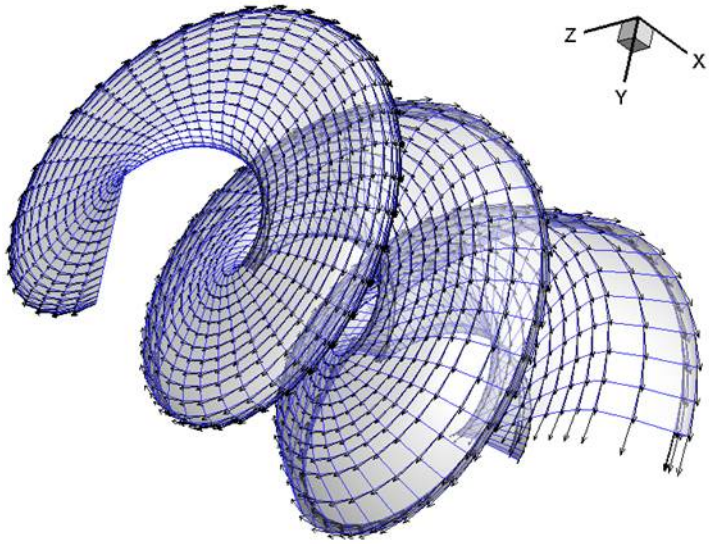

Figure 3.11: Alignment of the wake geometry and the induced velocity vectors induced on the wake panels (key blade coincident with y axis, inflow in the x-axis direction)

despite important differences of the wake structure in the far wake zone, the effect in the turbine's efficiency is limited to 0.5 to 1%. This model is called Simplified Wake Alignment LLOPT (LLOPT-SWA), and it is explained further in Section 4.1.2,

Figure 3.12 shows the wake surfaces for both alignment schemes, for the case of one blade ($Z = 1$) and TSR of 8. Figure 3.13 presents a comparison of the respective cross sections. The discretization of the far wake is not altered, so the definition of the roll up decreases further downstream from the turbine, located at the $x = 0$ plane.

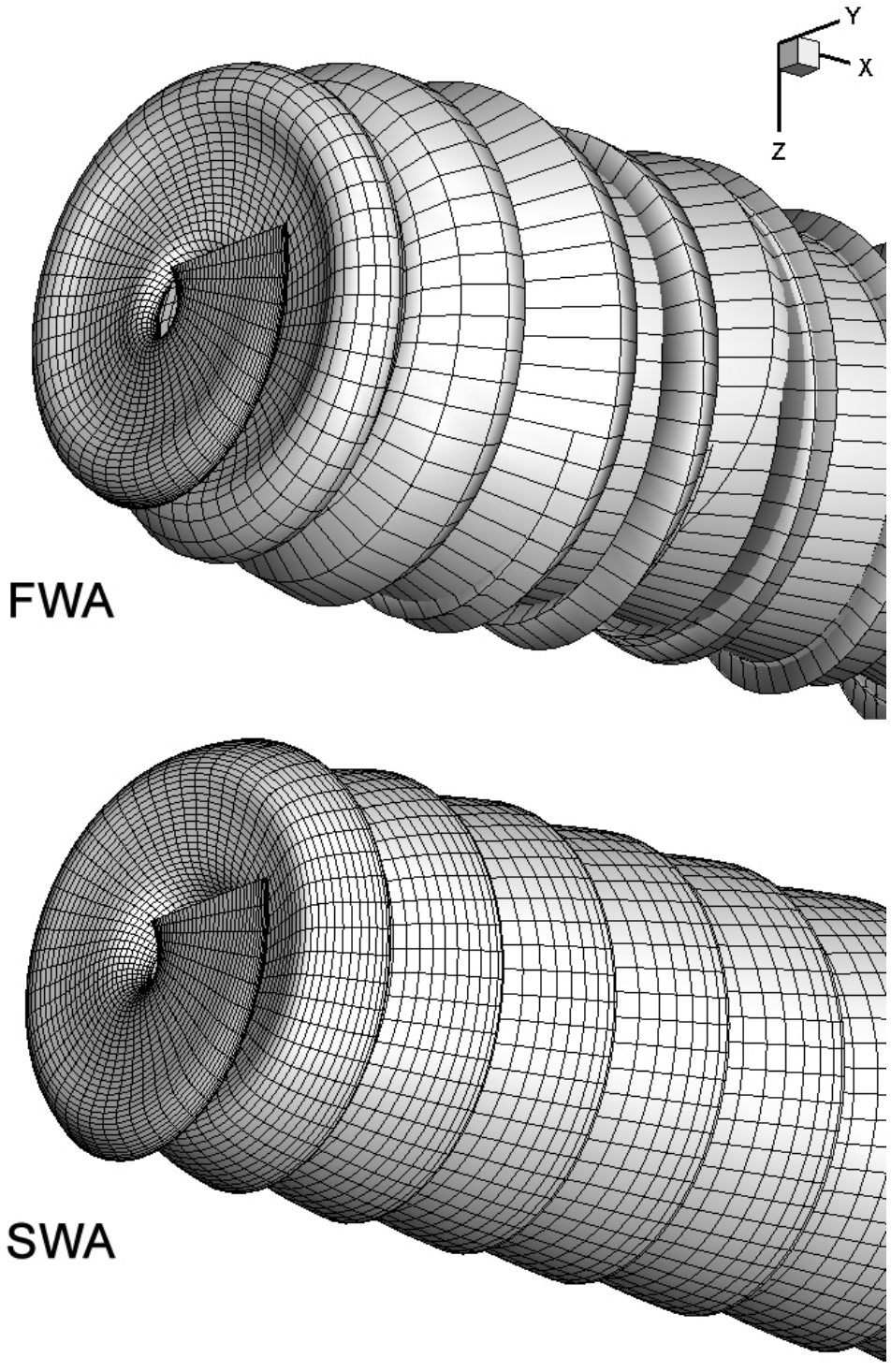

Figure 3.12: Comparison of wake shapes for two different alignment schemes: Full Wake Alignment (top) and Simplified Wake Alignment (bottom). $Z = 1$, $TSR = 8$

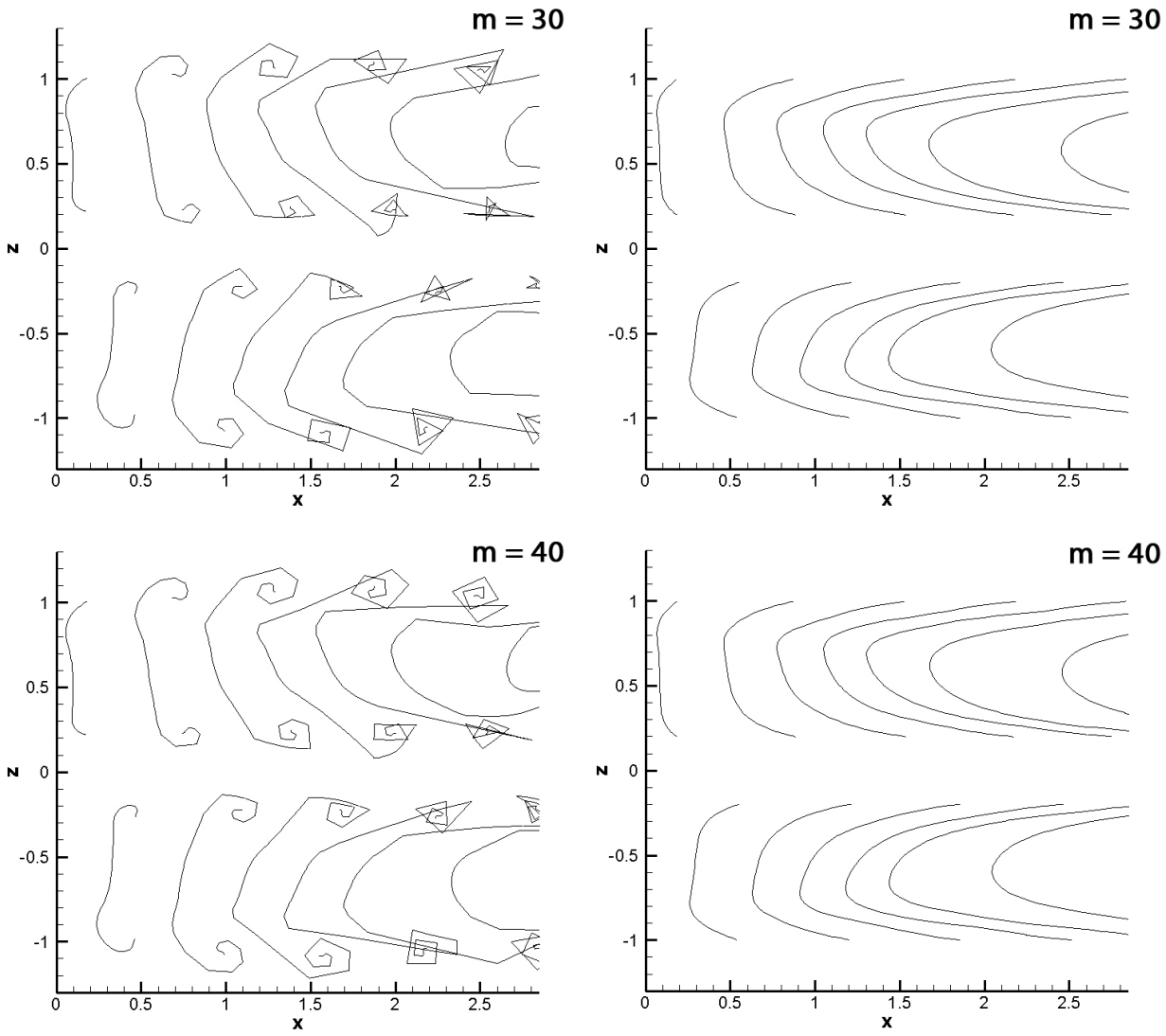

Figure 3.13: Comparison of wake cross sections for two different alignment schemes: Full Wake Alignment (left) and Simplified Wake Alignment (right). The curves are obtained through the intersection of the 3D wake surface with the xz plane (at $y = 0$). $Z = 1$, $TSR = 8$, varying number of radial elements (m)

3.3.3 Numerical Accuracy

Wrench (1957) [50] proved that the Lerbs-Wrench formulas have a great precision for semi-infinite helical vortices of constant pitch. These were used to validate the numerical method, comparing the results with those of an equivalent discretized wake with a time step of 6°. Figure 3.14 presents the comparison for four different cases: single vortices at the blade's mid-point and tip, and horseshoe vortices at the same locations. A pitch angle of 15° was chosen for the horseshoe vortices ($P/D = 0.49$ for vortex at mid-point, $P/D = 0.82$ for vortex at tip), and the single vortices were analyzed at varying pitch angles. The numerical method showed great accuracy, even in the proximities of the singularity as the control point approaches the vortex radius.

Having proven the good accuracy obtained for both a single vortex and a horseshoe vortex, the next step is the evaluation of the results for the complete wake. The discrete wake is generated from the pitch angles calculated by LLOPT-LW after its first iteration. Figure 3.15 shows the resulting wake geometry, where the discretization scheme is determined by three parameters: the total wake length L_w, the time step dth and the number of streamwise panels nc.

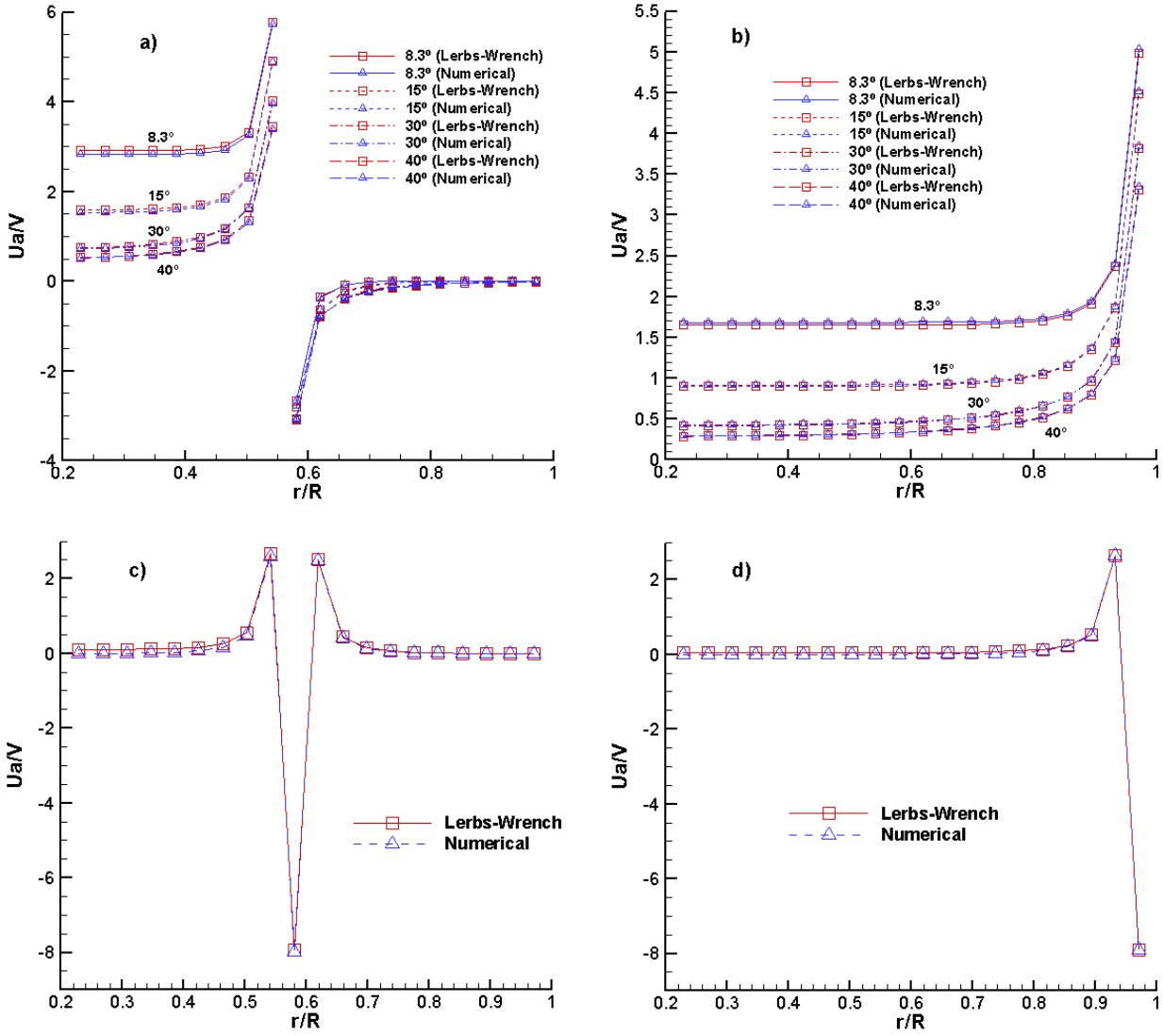

Figure 3.14: Normalized axial velocity. Validation of the numerical method by comparison with Lerbs-Wrench formulas: a) single vortex at the blade's mid-point, for different pitch angles; b) single tip vortex, for different pitch angles; c) horseshoe vortex at the blade's mid-point ($\beta_w = 15°$); d) horseshoe vortex at the blade's tip ($\beta_w = 15°$)

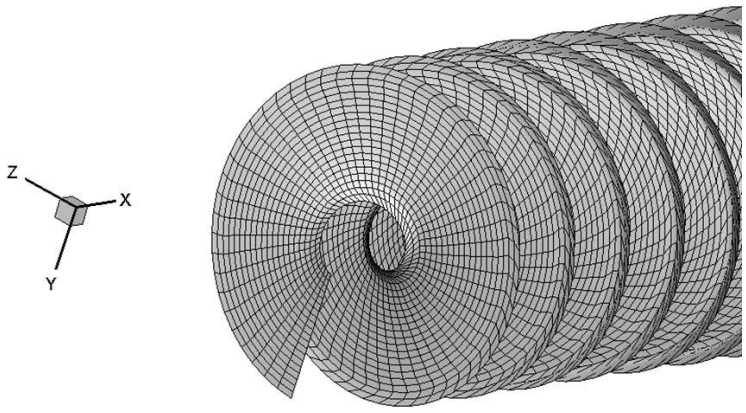

Figure 3.15: Constant-pitch wake used to simulate the use of the Lerbs-Wrench formulas ($L_w = 15$, $dth = 1$, $nc = 1500$)

In general, good agreement with the Lerbs-Wrench formulas is only achieved for a very fine panel grid, and the computational effort required to achieve an acceptable precision is considerable. To illustrate this, 8 different cases were evaluated for the first iteration of LLOPT-LW ($Z = 2$, $TSR = 10$, $V = 1$), and the results were compared with both those obtained from the use of the Lerbs-Wrench formulas and from a very fine discrete wake ($L_w = 35$, $dth = 0.25$, $nc = 80000$). The latter was deemed necessary to account for possible propagation of numerical errors, since LLOPT-LW and LLOPT-FWA contain a vastly different treatment variables and subroutines in their codes. The mean relative error on the turbine's control points between these circulation distributions was of only 0.06%, and they will serve as a basis for comparison with the results from more coarse discretizations. The cases analyzed are summarized in Table 3.1, and two criteria were used: A) Constant time step,

with different number of streamwise panels and thus different wake lengths; B) Constant wake length, different time steps and thus different number of streamwise panels.

	Contant time step				Constant wake length			
Parameter	A.1	A.2	A.3	A.4	B.1	B.2	B.3	B.4
Wake length (L_w)	17.5	8.75	4.38	1.75	17.5	17.5	17.5	17.5
Time step (dth)	1	1	1	1	0.5	1	5	10
Streamwise panels (nc)	10,000	5,000	2,500	1,000	20,000	10,000	2,000	1,000

Table 3.1: Wake geometry discretization parameters for the cases analyzed

The results are presented in Figure 3.16. The main conclusion drawn from these graphs is that the wake length L_w is the most important parameter to ensure appropriate accuracy. The benefits obtained through the use of smaller time steps are noticeable, but not as significant.

Table 3.2 summarizes the mean relative error on all the blade control points for all the cases studied, with respect to the base results described above. Case b.3) represents a good compromise between computational effort required and accuracy, and a similar discretization has in general been chosen for the graphs included in Section 4.

To further validate the use of the numerical scheme, the LLOPT-FWA model was modified in order to align the wake according to the assumptions of the Lerbs-Wrench formulas: constant-pitch helical vortices and alignment only at the lifting line. Given these constraints on the alignment routine, it is expected that the results will match the ones obtained through the LLOPT-

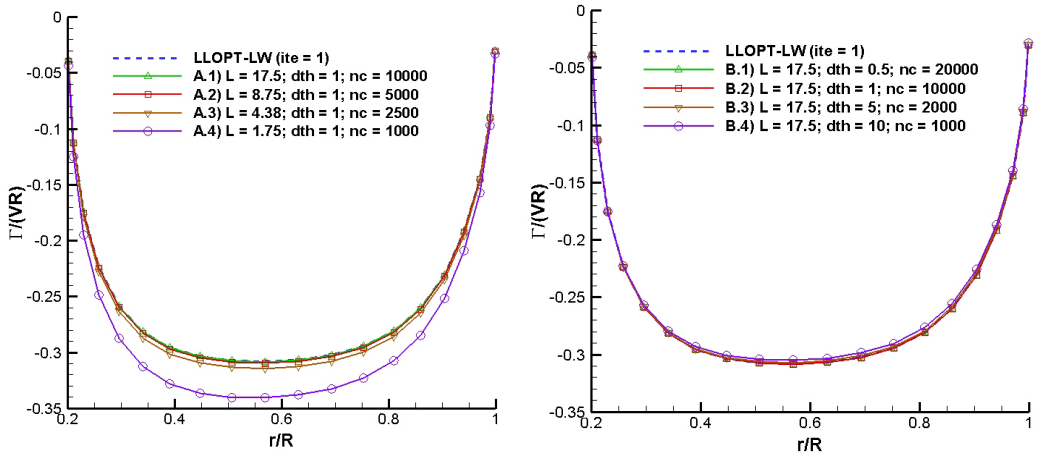

(a) Case A)

(b) Case B)

Figure 3.16: Circulation distributions for the first iteration of the optimization code, for different wake discretization schemes ($Z = 2$, $TSR = 10$)

LW model. Figure 3.17 shows the results for the first three iterations of both methods, for the case $Z = 2$, $TSR = 4$.

It can be seen that the instabilities common in the LLOPT-LW code, primarily caused by the extrapolation of $\tan(\beta)$ at the hub and tip of the key blade, are exacerbated by the use of numerical coefficients. The induced velocities at the tip and hub thus diverge for the fourth iteration in the numerical method. Convergence can be improved by the use of a finer discretization scheme on the wake, but this increases the computational effort required to solve the system when full wake alignment is used. The use of Betz's condition (Equation 3.26), which eliminates the need to use extrapolation to calculate the pitch and the hub and the tip, fixes these convergence issues without a noticeable loss in efficiency for the Lerbs-Wrench model.

	With respect to LLOPT-LW				With respect to numerical wake			
Case	1	2	3	4	1	2	3	4
A	0.13%	0.47%	1.94%	10.24%	0.09%	0.41%	1.88%	10.18%
B	0.13%	0.13%	0.72%	1.81%	0.07%	0.09%	0.77%	1.85%

Table 3.2: Relative error of different wake discretizations with respect to the results obtained through the use of the Lerbs-Wrench formulas and a very precise numerical wake ($dth = 0.5$, $nc = 80000$, $L_w = 35$). Average values of relative error for all control points on the blade

These results emphasize the importance of the far wake on the results, but computational time considerations limit the number of panels that can be used for a practical optimization process. The use of larger time steps is a possible partial solution, but also shows limitations since it can misrepresent the important near wake geometry. This appears to suggest that a mixed model with a variable time step could represent an efficient compromise between accuracy and swiftness. A smaller time step could be used closer to the rotor in order to capture the near wake, and a larger time step would be chosen one or two diameters downstream. The wake alignment procedure can also be modified such that the entire wake is not updated in each iteration, and instead the far wake's pitch is kept constant for several iterations, thus reducing the number of calculations needed.

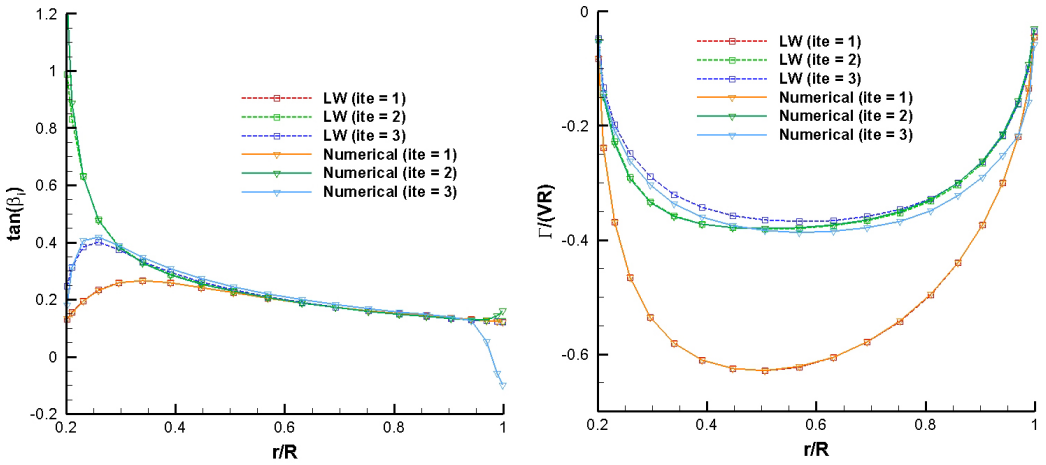

(a) Pitch angle (b) Circulation

Figure 3.17: Comparison of LLOPT-LW using Lerbs-Wrench formulas to a model using a discretized wake, results for the first three iterations ($Z = 2$, $TSR = 4$)

3.4 Generation of Blade Geometry

A preliminary method for the design of a turbine blade based on the optimum circulation distribution and Prandtl's lifting line equation (Kerwin and Hadler, 2010 [22]) is presented next. We carry out the generation of a base geometry for the blade following the methodology indicated in Kinnas et al (2012) [29]. The dimensionless circulation can be related to the sectional lift coefficient by the Kutta-Joukowski law according to:

$$C_L(i) = \frac{L(i)}{\frac{1}{2}\rho \left(V^*(i)\right)^2 c(i)} = \frac{2\Gamma(i)}{V^*(i)c(i)} \qquad i = 1, \ldots, M \tag{3.76}$$

Given a chord distribution $c(i)$ and a blade section profile, the optimal circulation distribution found previously determines the lift coefficient for each control point. The sectional blade pitch angle ϕ, on the other hand, relates

to the modified pitch angle β_i of the total inflow by the following expression. Figure 3.3 shows the angles mentioned and the corresponding velocities and forces with respect to the blade section at a given r.

$$\phi(i) = \beta_i(i) - \alpha_i(i) \tag{3.77}$$

where $\alpha_i(i)$ is the sectional ideal angle of attack. Both the angle of attack and the sectional maximum camber with be a function of the corresponding lift coefficient, as shown in equations 3.78 and 3.79. α_0 and f_0 are the ideal angle of attack and ideal maximum camber for a certain section when $C_L = 1.0$.

$$\alpha_i(i) = \alpha_0 C_L(i) \tag{3.78}$$

$$f_{max}(i) = f_0 C_L(i) \tag{3.79}$$

The finished geometry can then be analyzed using a vortex lattice model, MPUF-3A (Lee, 1979 [32] and He, 2010 [19]), or a low-order panel method, PROPCAV. Both allow us to determine the pressure on the blades, an accurate measure for the efficiency and the radial circulation distribution. Comparing this to the original circulation used to calculate the blade geometry can also function as a simple validation of the design methodology.

As noted before, the use of the unconstrained LLOPT-FWA produces non-smooth optimum circulation distributions. If used to generate a blade geometry, they result in very uneven blade surfaces incompatible with optimum hydrodynamic and structural design. To produce a realizable blade geometry, the optimization has been constrained to smooth circulations. Figure 3.18

presents a comparison for two geometries generated from the unconstrained and constrained variations of the LLOPT-FWA model, in the case of a two-bladed turbine with an infinite hub model.

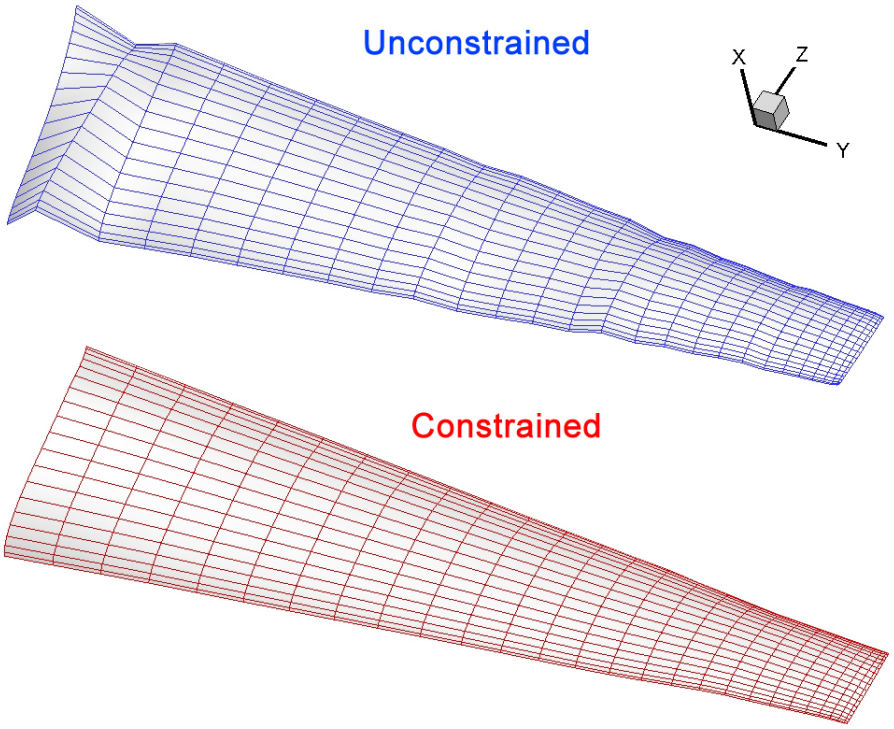

Figure 3.18: Comparison of blade geometries as generated from unconstrained and constrained LLOPT-FWA models for a turbine with a hub ($Z = 2, TSR = 4$)

Chapter 4

Results

4.1 Turbines

4.1.1 LLOPT-LW

Although the formulation presented in Section 3.1.3 appears to be valid a priori for the optimization of turbines, the circulation distributions obtained through this method produce efficiencies that are significantly lower than the Betz limit. Furthermore, the solutions for high number of blades and high TSR do not approach this limit, as was expected for an accurate turbine optimization tool. The induced axial velocities on the blade u_a^* oscillate around the value $-\frac{1}{2}V$ for the optimum solution, far removed from the actuator disk solution $u_a^* = -\frac{1}{3}V$ as shown in Section 3.1.1.

Figure 4.1 shows the efficiencies obtained for different rotational speeds, number of blades and values for the drag-to-life ratio κ. As expected, the turbine's efficiency decreases as the viscous drag becomes significant. In addition, the optimum efficiency takes place at lower values of TSR for increasing drag-to-lift coefficients. The inviscid solution ($\kappa = 0$) asymptotically approaches a value smaller than 50%.

This result has been reproduced by other authors who have worked

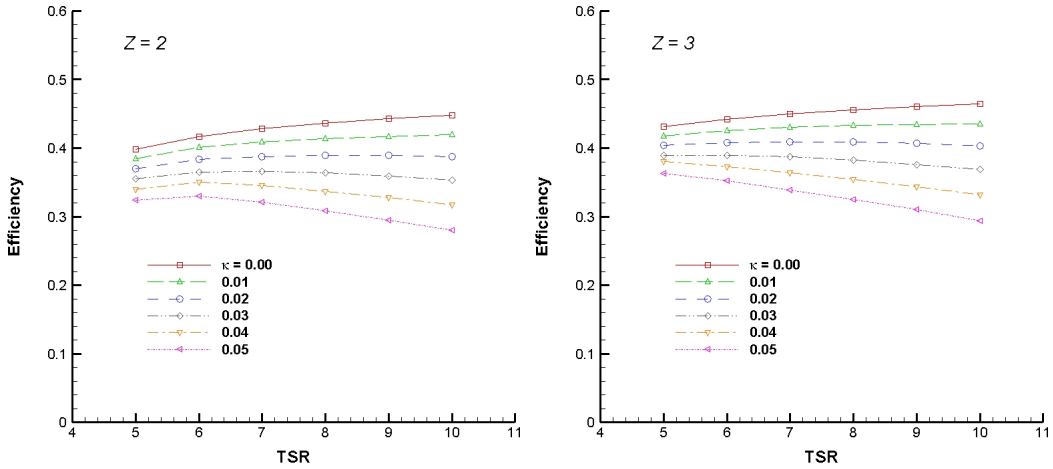

(a) $Z = 2$ (b) $Z = 3$

Figure 4.1: Optimum efficiency as a function of tip speed ratio for different values of drag-to-lift ratio κ, LLOPT-LW model, different number of blades Z

on turbine lifting line optimization, such as Falcão de Campos (2007) [13] and Epps (2010) [10]. Epps (2010) proposed a work-around to this problem through the use of actuator-disk-with-swirl-and-viscous-losses (ADS) theory (Stewart, 1976 [45]). He applies an ADS-based optimizer, initially setting the tangential induced velocity to the ADS value. The optimization equations are then solved iteratively in order to obtain a set of flow parameters consistent with this assumption. This method, used in the open source code OpenProp, produces efficiencies that approach actuator disk theory.

Only three assumptions are made during the derivation of the optimization equations in Section 3.1.3:

- *Linearity.* As described by Equation 3.23, higher order terms have been discarded. Appendix B explores a possible extension of the method in

order to include these second-order terms, but the results obtained have not been satisfactory.

- *Constant pitch.* The use of the Lerbs-Wrench formulas effectively limits the type of wake geometries that can result from this optimization procedure to those that can be described by constant-pitch helical vortices. The use of linear inter- and extrapolation to calculate the pitch angles at the vortex points further constrains the geometry.

- *Alignment at lifting line.* The "moderately loaded propeller" assumption has not been validated for turbines.

In order to generalize the optimization procedure for all wake shapes, a full wake alignment model was implemented. The Lerbs-Wrench model, as described in Section 3.1.3, is thus assumed insufficient for turbine optimization, although it can still be used for propellers with good accuracy, as shown in Section 4.2.2. It is worth noting that Epps and Kimball (2013) obtained higher efficiencies within the Lerbs-Wrench methodology by applying a "design constraint", as described in Section 2.1.

The optimum circulation distribution as determined by LLOPT-LW can be used an an input for the alignment routine described in Section 3.3.2. This will produce a new trailing wake that will differ considerably from the constant-radius, constant-pitch one assumed by the Lerbs Wrench model, and thus modify the induced velocities u_a^* and u_t^* on the key blades. The efficiency calculated based on these new induces velocities and the original circulation

is substantially higher than the one from LLOPT-LW. This result seems to suggest that wake alignment has at least a significant effect on the prediction of efficiency in the case of turbines.

Sections 3.1.5 and 3.1.6 describe the representation of the circulation distribution as a series of functions, as a necessary step towards constraining the solution. To test the validity of the formulation, however, they can also be used within the Lerbs-Wrench model. Figure 4.2 shows the solution obtained for the same turbine and flow parameters through both formulations, with increasing number of modes NG. It can be seen that the results converge to the original LLOPT-LW solution as the number of modes increases, as expected. Another important conclusion drawn from Figure 4.2a is that the numerical scheme can be unstable for very high NG and certain flow parameters.

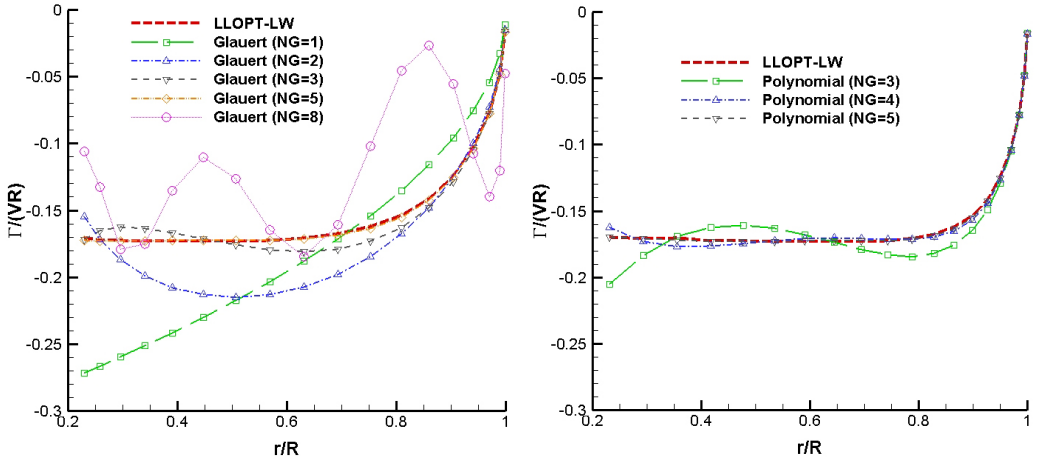

(a) Glauert series (b) Polynomial

Figure 4.2: Glauert series and polynomial representation with Lerbs-Wrench model, $Z = 3, TSR = 6$, turbine with hub

4.1.2 LLOPT-FWA

It was discussed in Section 3.3.2 how the use of an unconstrained full wake alignment model leads to non-smooth circulation distribution. An example can be seen on Figure 4.4, and the loading spike near the tip is exacerbated as Z and TSR increase. Although the efficiencies obtained are considerably higher than those obtained with the LLOPT-LW model, it is expected that this solution is not compatible with a hydrodynamically and structurally optimum design.

Despite this, convergence with number of elements is good. Figure 4.3 presents the optimum circulation distribution for 10, 20 and 30 radial elements and three different values of the κ ratio, for LLOPT-FWA. The local increase in the circulation distribution near the tip becomes smaller as viscosity increases, but it never disappears even for unrealistically high drag-to-lift ratio.

κ	η
0	52.65%
0.04	43.21%
0.08	32.15%

Table 4.1: Comparison of efficiencies for the unconstrained LLOPT-FWA model, varying values of the drag-to-lift ratio κ. ($Z = 3$, $TSR = 5$)

Two solutions have been attempted: constraining the wake to reduce the impact of roll-up and expansion, or constraining the circulation in order to ensure smooth variations in loading.

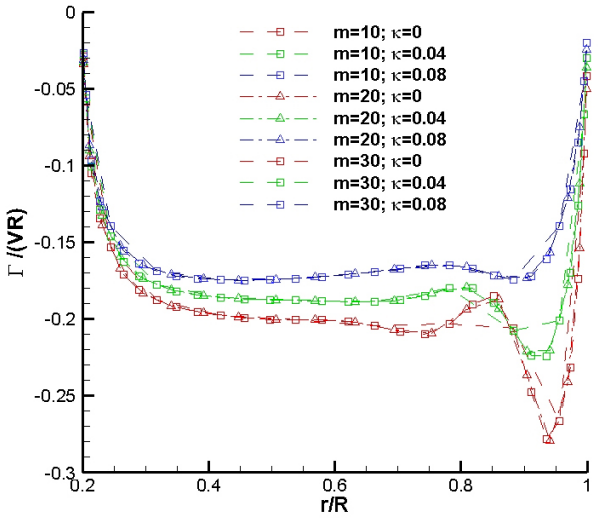

Figure 4.3: Convergence analysis for the optimal circulation distribution, for different number of radial sections, simplified wake alignment and varying drag-to-lift ratio κ ($TSR = 5$, $Z = 3$). The corresponding efficiencies are presented in Table 4.1.

4.1.2.1 Constraints on Alignment

The most immediate way to simplify the wake geometry is to cancel both expansion and roll-up, two phenomena that were not present in the Lerbs-Wrench model. The Simplified Wake Alignment (SWA) results in a smoother circulation distribution, but it still presents a spike near the tip that is more pronounced as the turbine's rotational speed and the number of blade increase. Figure 4.4 shows a comparison of the optimum circulation for both alignment models, using inviscid formulation. The increase of optimum circulation towards the tip is reminiscent of the findings of Loukakis (1971) [37]. This result is also discussed in detail in Kerwin et al (1986) [21].

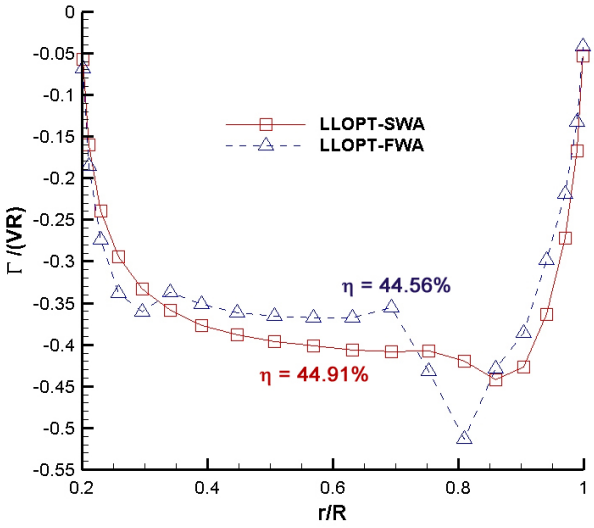

Figure 4.4: Comparison of optimum circulation distributions for Full and Simplified Wake Alignments ($TSR = 4$, $Z = 2$)

Figure 4.5 present a comparison between the results obtained with the

simplified wake alignment model and LLOPT-LW. The axial velocities induced with the new method are significantly lower on the majority of the blade, but present a spike near the tip that coincides with the singular behavior in that zone.

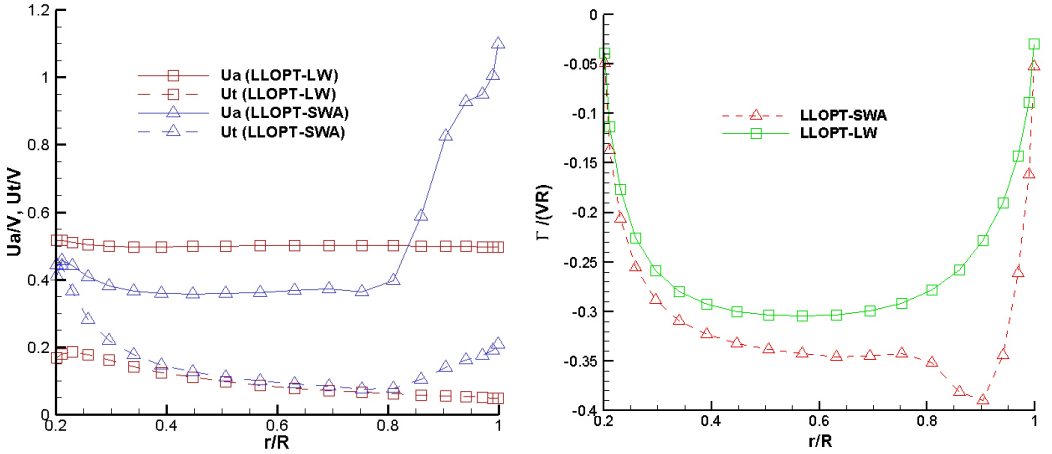

(a) Axial and tangential velocities

(b) Circulation

Figure 4.5: Comparison of results for LLOPT-SWA and LLOPT-LW models ($TSR = 5$, $Z = 2$)

Convergence with number of elements is in general very good for Simplified Wake Alignment. Figure 4.6 presents the optimum circulation distribution for 10, 20 and 30 radial elements and three different values of the κ ratio, for LLOPT-SWA. The number of streamwise panels must be sufficient to accurately represent the effects of the far wake on the induced velocities. The streamwise discretization chosen depends largely on the TSR of the turbine being analyzed. It is also important to note how, as was the case for Full Wake Alignment, the local increase in the circulation distribution near

the tip becomes smaller and disappears once viscosity is introduced to the formulation.

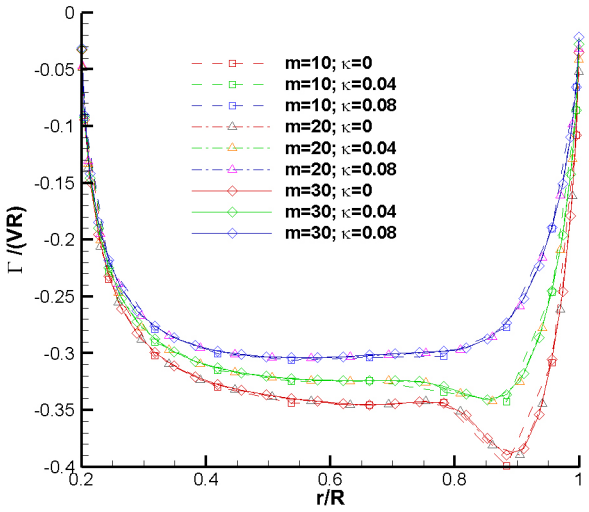

Figure 4.6: Convergence analysis for the optimal circulation distribution, for different number of radial sections, simplified wake alignment and varying drag-to-lift ratio κ ($Z = 2$, $TSR = 5$). The corresponding efficiencies are presented in Table 4.2.

κ	η
0	48.50%
0.04	39.78%
0.08	29.33%

Table 4.2: Comparison of efficiencies for the unconstrained LLOPT-SWA model, varying values of the drag-to-lift ratio κ. ($Z = 2$, $TSR = 5$)

Figure 4.7 present the resulting efficiencies for the SWA model for varying values of the drag-to-lift ratio κ and two and three blades. As was the case for the LLOPT-LW model, the efficiency of the turbines decreases as the vis-

cous drag becomes significant. For the case of a 3-bladed turbine, $TSR = 6$ and $\kappa = 0.02$, the efficiency is 49%. For the same parameters but increased drag ($\kappa = 0.04$), the efficiency is reduced to 42.3%. Once again, the optimum efficiency takes place at lower values of TSR for increasing drag-to-lift ratios.

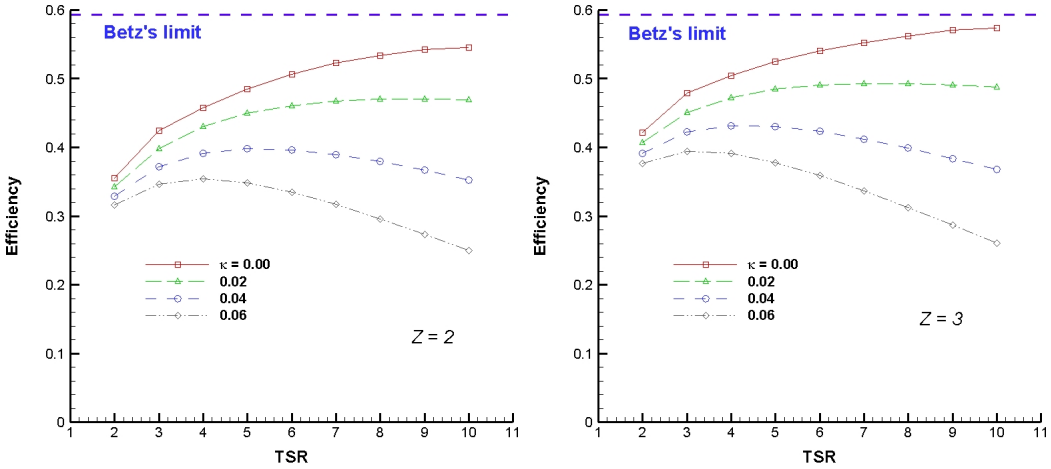

(a) $Z = 2$ (b) $Z = 3$

Figure 4.7: Optimum efficiency as a function of tip speed ratio for different values of drag-to-lift ratio κ, LLOPT-SWA model, different number of blades Z

The analysis detailed in this chapter can be extended to the case of turbines with hub by including the hub model described in Section 3.1.4. Once again the unconstrained Full Wake Alignment model results in non-smooth circulations that are incompatible with a realizable, optimum blade geometry. Cancelling the expansion and roll-up on the aligned wake produces a smoother circulation, but there is still an increase of the loading near the tip. Figure 4.8

compares the results for both models, in the case of the two-bladed propeller analyzed in Figure 4.4.

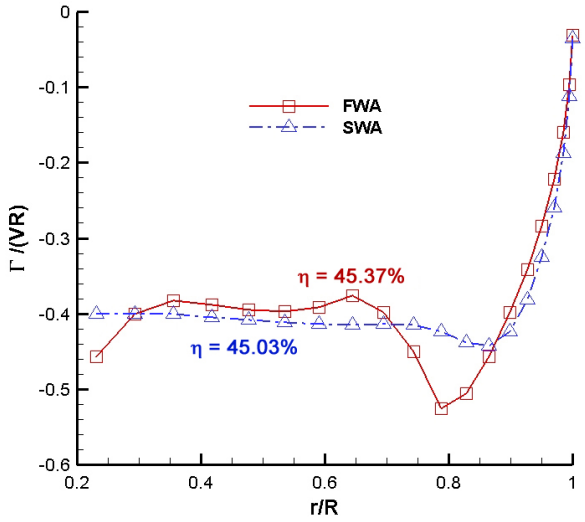

Figure 4.8: Optimum circulation distributions for the case of a turbine with hub, Full and Simplified Wake Alignments. ($TSR = 4$, $Z = 2$)

Even though the SWA model improves the smoothness of the circulation distribution, the increased loading near the tip persisted. In addition, the elimination of the wake expansion and roll-up cancels a large part of the benefits sought by introducing wake alignment in the formulation. For these reasons, the possibility of constraining the circulation without modifying the wake alignment routine was analyzed.

4.1.2.2 Constraints on Loading

The functional representations described in Sections 3.1.5 and 3.1.6 can constrain the solution just through the choice of the NG parameter, which

represents the order of the polynomial in polynomial representation and the number of modes in Glauert series representation. The lower NG is, the more limited the shapes that can be represented through the use of the circulation function.

Figure 4.9 shows a comparison between the unconstrained LLOPT-FWA model and two different values of NG for both representations. Table 4.3 compares the efficiencies corresponding to each circulation distribution, and calculates the absolute error with respect to the original unconstrained model.

A number of problems arise from the use of these functions:

- The higher the number of modes selected is, the more the solution approaches the original unconstrained optimization, showing both the increase near the hub and near the tip that we were trying to correct. In general, the efficiencies obtained with the functional models approach the unconstrained LLOPT-FWA solution as NG increases.

- As Z and TSR grow, the optimum circulation distribution becomes increasingly flatter and the transition between the square root singularity near the tip and the hub and the constant loading through the majority of the blade's length becomes harder to represent with a low number of modes. (In the limit, the constant loading of an actuator disk would require infinite number of modes to represent.) However, a high number of modes leads to circulation distributions that oscillate around a constant

value, with several inflection points and incompatible with our intended result.

- Representations with a high number of modes are often numerically unstable, even in the case that they are used within the LLOPT-LW model.

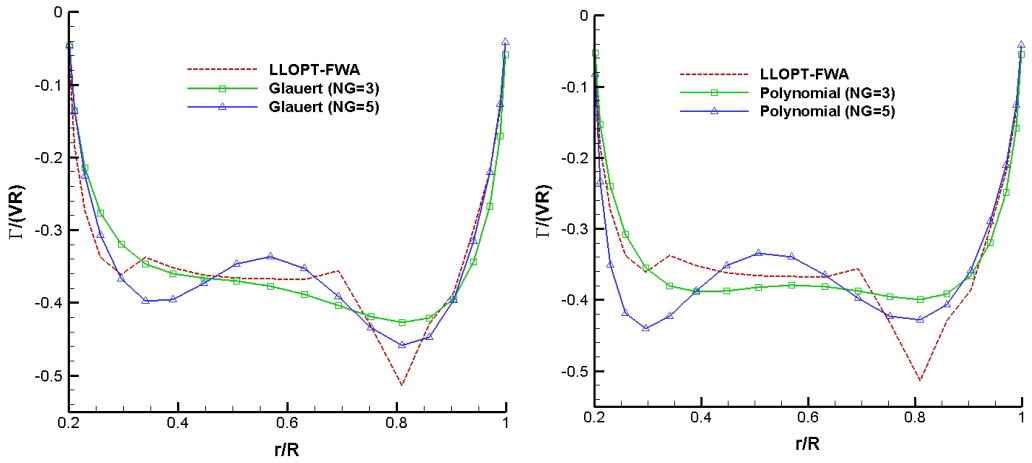

(a) Glauert series

(b) Polynomial

Figure 4.9: Comparison between unconstrained LLOPT-FWA and functional representations, different values of NG parameter ($Z = 2$, $TSR = 4$). The corresponding efficiencies are presented in Table 4.3.

For these reasons, it was decided to focus on the use of low-order representations (in general, $NG = 3$), and add additional constraints in order to ensure the lack of inflection points along the optimum circulation distribution. The results presented correspond to low-order representations, but the analysis can be extended to solve the optimization problem with higher number of modes.

Representation	NG	η	Absolute difference
Original FWA	-	44.56%	-
Glauert series	3	44.80%	0.24%
	5	44.57%	0.01%
Polynomial	3	44.83%	0.27%
	5	44.61%	0.04%

Table 4.3: Comparison of efficiencies with respect to number of modes and functional representation. Absolute difference with respect to original unconstrained LLOPT-FWA model. ($Z = 2$, $TSR = 4$)

As explained in Section 3.1.7, two constraints are imposed on the circulation distributions. The first one ensures that the curvature of the loading will not change along the blade, preventing those loading spikes near the tip. The second one preserves the slope of the loading at the blade midpoint from the original unconstrained solution. Without it, the optimization tends to result in optimum blades heavily loaded near the tip. However, it is possible to remove this ad-hoc constraint on the slope if the distribution of the loading is not at issue, since the smoothness of the solution does not depend on it.

Figure 4.10 compares the results for LLOPT-LW and the constrained LLOPT-FWA method, for two different numbers of blades. It is worth noting that in order to better capture the loading near the tip and the hub it is necessary to increase the number of modes. It will be necessary to further study the variation of loading with number of nodes for cases with high number of blades.

In both optimization alternatives, convergence with regards to number

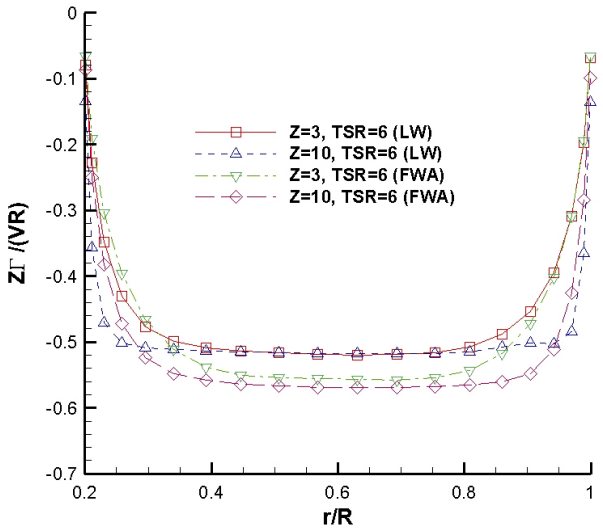

Figure 4.10: Comparison of circulation distribution multiplied by number of blades ($Z\Gamma$) for LLOPT-LW and constrained LLOPT-FWA. ($TSR = 6$, varying number of blades)

of elements and with number of coefficients (order of the polynomial) is good. Figures 4.11 and 4.12 present convergence studies for both optimization alternatives, in the case of a two-bladed turbine rotating at $TSR = 4$. Table 4.4 compares the efficiencies of the constrained optimization models to the one obtained for the original unconstrained solution.

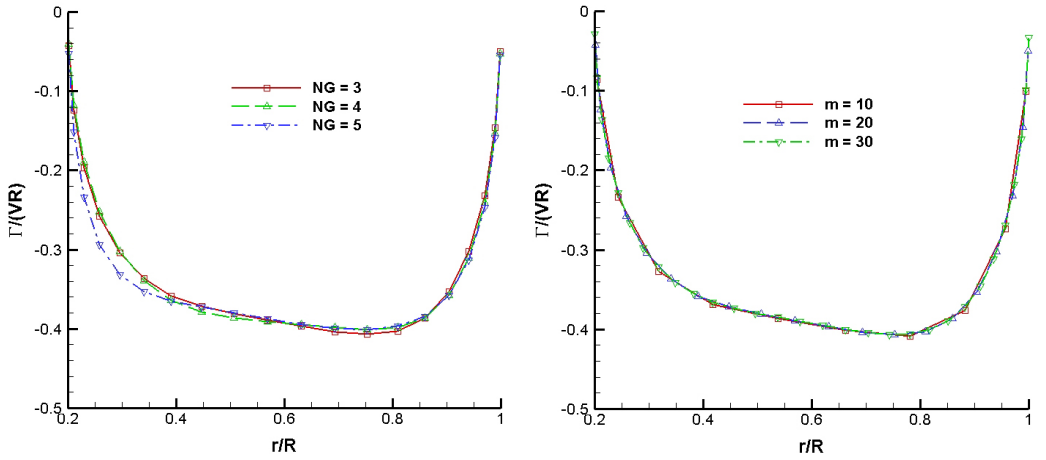

(a) With number of coefficients (b) With number of elements

Figure 4.11: Convergence analysis of the constrained optimization method, curvature-only case ($Z = 2, TSR = 4$). The corresponding efficiencies are presented in Table 4.4.

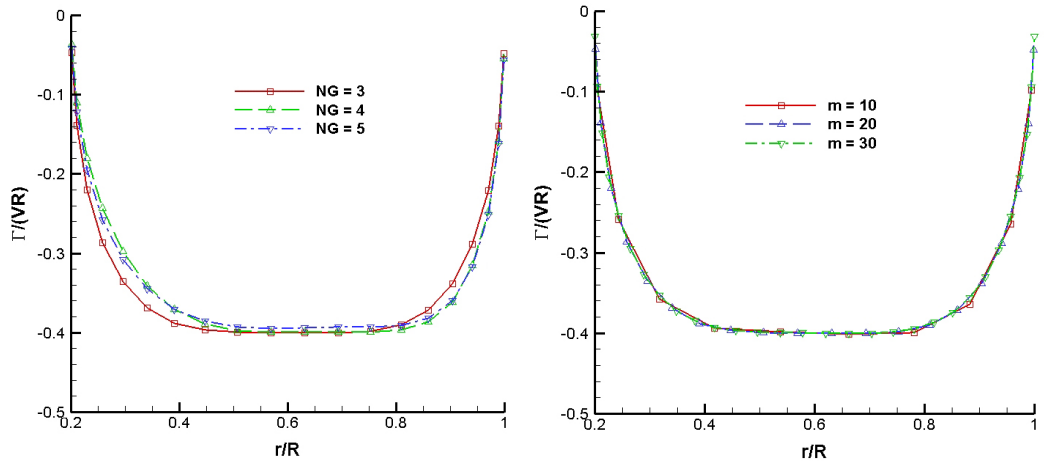

(a) With number of coefficients (b) With number of elements

Figure 4.12: Convergence analysis of the constrained optimization method, curvature and slope case ($Z = 2, TSR = 4$). The corresponding efficiencies are presented in Table 4.4.

Representation	M	NG	η	Absolute difference
Unconstrained FWA	20	-	44.56%	-
Curvature only	20	3	44.38%	-0.18%
	20	4	44.29%	-0.27%
	20	5	44.36%	-0.20%
	10	4	44.47%	-0.09%
	30	4	44.37%	-0.19%
Curvature and slope	20	3	44.56%	0.00%
	20	4	44.04%	-0.52%
	20	5	44.12%	-0.44%
	10	4	44.64%	0.08%
	30	4	44.53%	-0.03%

Table 4.4: Comparison of efficiencies with respect to number of modes and control points for constrained optimization models. Absolute difference with respect to original unconstrained LLOPT-FWA model. ($Z = 2$, $TSR = 4$)

Both constrained optimization alternatives completely remove the singular behavior near the tip of the blade, while maintaining a similar loading on the rest of the blade. Figure 4.13 compares the optimum circulation given by the unconstrained and constrained LLOPT-FWA models.

The constrained LLOPT-FWA model results in induced axial velocities that are considerable lower than for the equivalent LLOPT-LW results, approximating the actuator disk solution $u_a^* = \frac{1}{3}V$. The tangential velocities are slightly increased, and towards the hub and the tip of the blade the sudden increase in the magnitude of the velocities is most likely caused by the wake expansion and roll-up.

As mentioned in Section 3.1.3, the classical optimization approach is

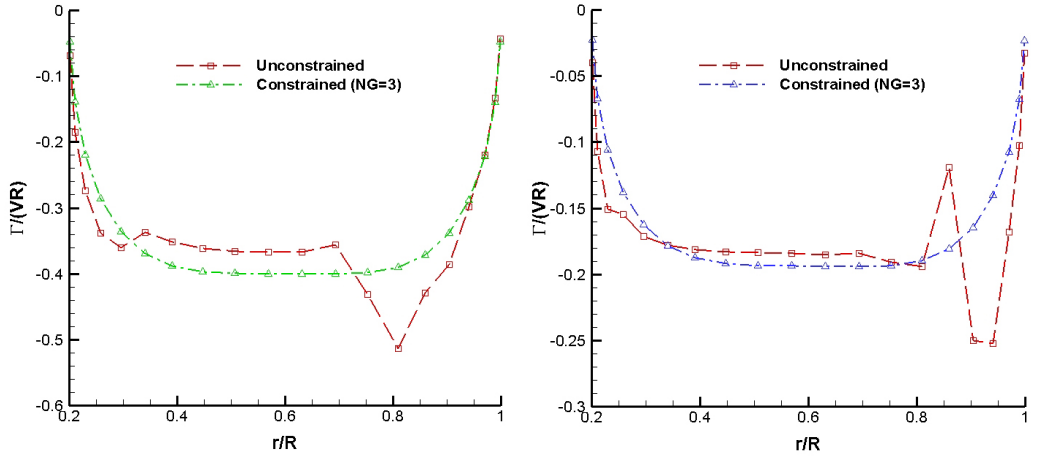

(a) $Z = 2, TSR = 4$ (b) $Z = 3, TSR = 6$

Figure 4.13: Comparison of circulation distributions between constrained and unconstrained LLOPT-LWA, different Z and TSR

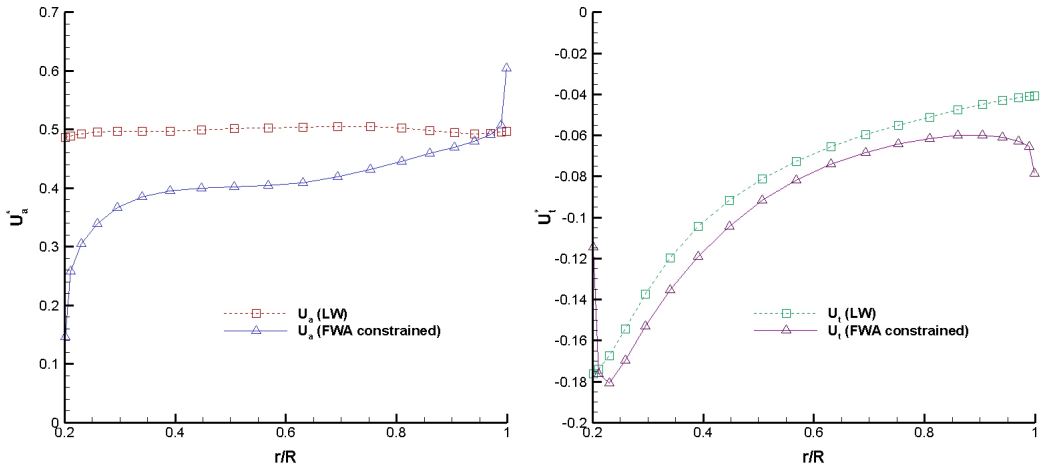

(a) Induced axial velocity u_a^* (b) Induced tangential velocity u_t^*

Figure 4.14: Comparison between constrained and unconstrained LLOPT-LWA. ($Z = 2$, $TSR = 4$)

based on Betz's condition as defined by Equation 3.26. Figure 4.15 compares this ratio as calculated for the optimum solutions of LLOPT-LW and the constrained LLOPT-FWA models. It can be seen that the Lerbs-Wrench model approximates a constant ratio, in particular as TSR increases. On the other hand, the Full Wake Alignment model differs considerably near the hub and the tip of the blade.

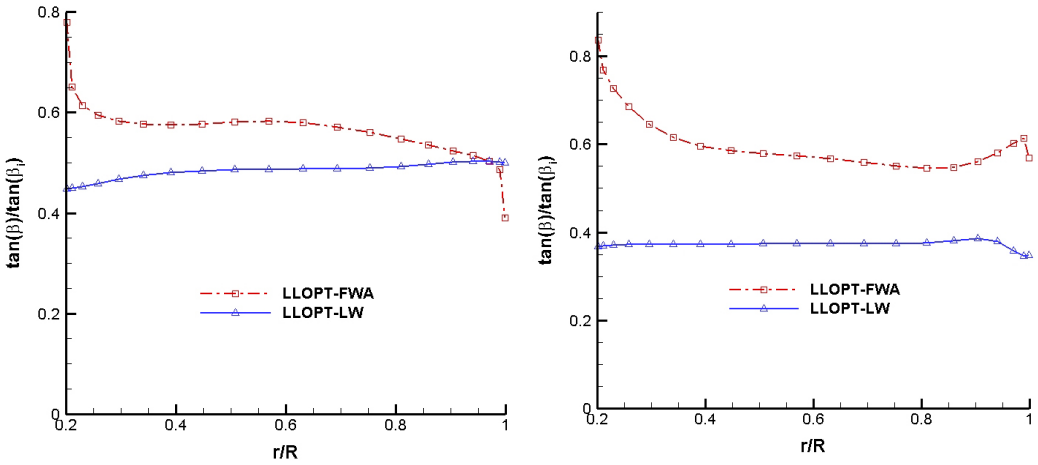

(a) $Z = 3, TSR = 6$ (b) $Z = 3, TSR = 15$

Figure 4.15: Ratio between the aligned pitch angle β_i and the geometric pitch angle β, for different values of Z and TSR

Once more, this analysis can be extended to the case of turbines with hub by including the hub model detailed in Section 3.1.4. Figure 4.16a compares the unconstrained Full Wake Alignment solution with the one obtained from polynomial representation of second and fourth degree. Figure 4.16b shows the results obtained from the two constrained optimization models described in this section. Table 4.5 presents a comparison of the efficiencies as

calculated with each model, using Full Wake Alignment in all cases.

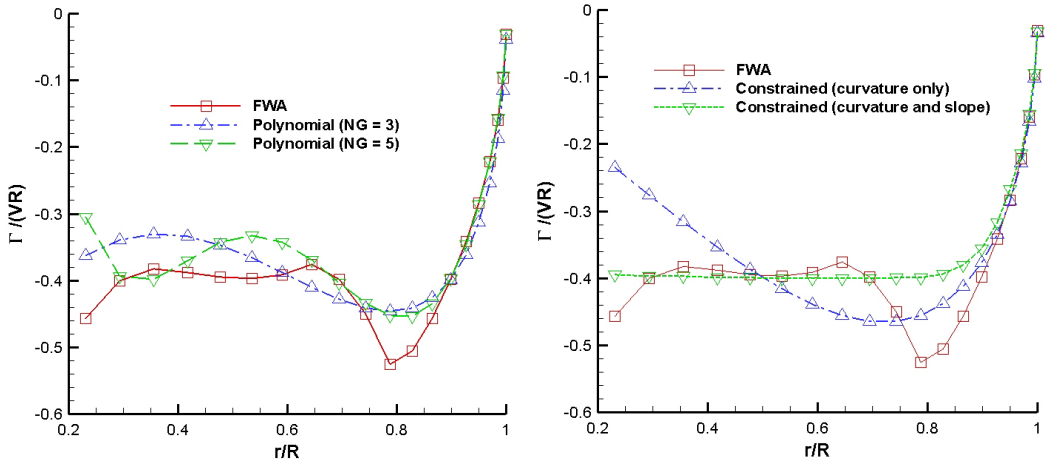

(a) Polynomial representation (b) Constrained optimization

Figure 4.16: Optimum circulation distributions for turbines with hubs. Comparison of solution for unconstrained optimization with both unconstrained polynomial representation and constrained optimization distributions ($Z = 2$, $TSR = 4$). The corresponding efficiencies are presented in Table 4.5.

Representation	η	Absolute difference
Unconstrained FWA	45.37%	-
Unconstrained SWA	45.03%	-0.34%
Unconstrained polynomic (NG = 3)	44.42%	-0.95%
Unconstrained polynomic (NG = 5)	45.25%	-0.12%
Constrained (Curvature only)	44.58%	-0.79%
Constrained (Curvature and slope)	45.12%	-0.25%

Table 4.5: Comparison of efficiencies between constrained and unconstrained optimization models, for the case of a turbine with hub. Absolute difference with respect to original unconstrained LLOPT-FWA model. ($Z = 2$, $TSR = 4$)

4.1.3 Comparison of Results

The use of a wake alignment model allows for a considerable increase in the efficiencies obtained from the lifting line optimization formulation. Figure 4.17 compares the efficiencies for the LLOPT-LW, LLOPT-SWA and constrained LLOPT-FWA models, as well as for the database-search method LLOPT-BASE developed by Xu (2010) [52] based on analysis runs using the LLOPT-LW model.

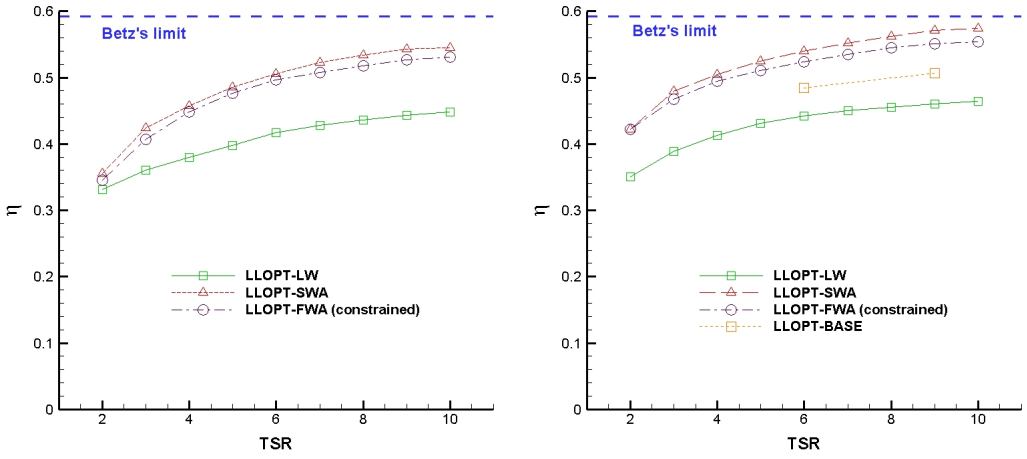

(a) $Z = 2$ (b) $Z = 3$

Figure 4.17: Comparison of efficiencies obtained through different lifting line optimization methods, different number of blades Z

It can be seen that the SWA and constrained FWA models produce almost identical efficiencies, with the former being slightly higher. However, unlike the SWA model, the constrained FWA model produces smoother circulations for any combination of parameters, and is based on a more realistic wake shape that accounts for roll-up and expansion. The efficiencies of the

constrained FWA model asymptotically approach Betz's limit as TSR and Z increase.

It is important to note that the calculation of the torque and thus the efficiency depends on both the circulation distribution and the induced velocities. Two different wake shapes will thus produce a different efficiency, for a given circulation. The efficiencies obtained through the SWA and FWA wake alignment routines thus cannot be directly compared, and the latter should be preferred if possible. For the comparison to be possible, the circulation distributions obtained with the LLOPT-SWA model should be used as an input to the FWA routine, but this has not yet been done.

The Lerbs-Wrench model suffers from numerical stability issues for most combinations of flow and turbine parameters. Regardless of the convergence criterion used, the algorithm achieves good convergence within the initial three to seven iterations and afterwards diverges. One of the possible sources this numerical instability in the extrapolation of the pitch angle from the outermost control points to the first and last vortex in the scheme presented in Figure 3.2. Epps and Kimball (2013) [11] solve this problem by assuming that each horseshoe vortex has constant pitch, disconnected from the pitch of the neighboring horseshoes.

All of the efficiencies included in Figure 4.17 are taken from the iteration for which convergence is optimum. The Full Wake Alignment models, in all their versions, do not present this issue. Figure 4.38a presents a typical case, for the two-bladed propeller previously used.

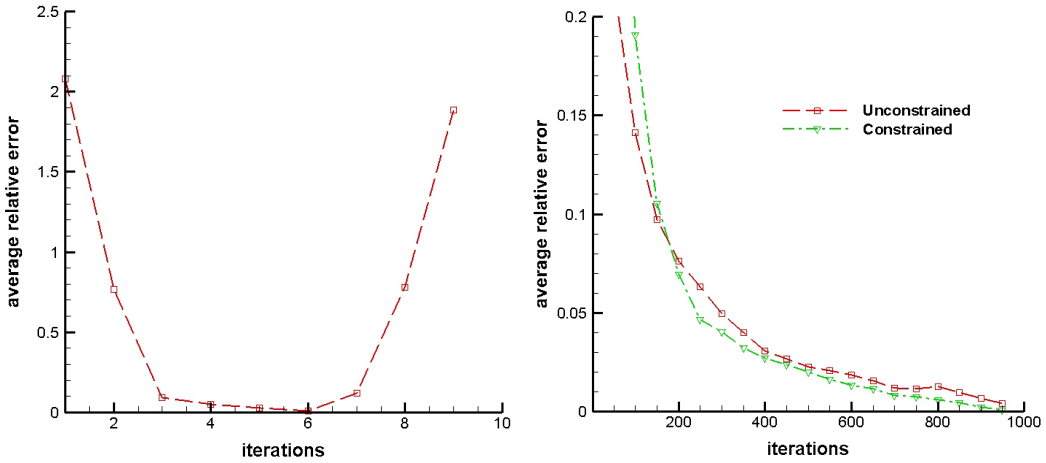

(a) LLOPT-LW (b) LLOPT-FWA

Figure 4.18: Convergence of both models with number of iterations. The LLOPT-FWA results include both the unconstrained and constrained versions. ($Z = 2$, $TSR = 4$)

The efficiency values included in Table 4.8 were taken from the iteration for which the convergence criterion utilized (root mean square of circulation difference vector) was minimum. The Full Wake Alignment model does not present from these convergence issues, as shown in Figure 4.38b.

4.1.4 Blade Geometry

For the generation of the blade geometry, it is necessary to choose an arbitrary sectional maximum thickness and chord distribution. These will be later on corrected to account for hydrodynamic and structural reasons, but should in all cases return similar loading distributions when analyzed with the vortex-lattice method MPUF-3A and the boundary element method PROPCAV for an inviscid no-drag case.

The blade geometries presented in Figure 4.19 were based on the results of the unconstrained LLOPT-FWA model, for the case $Z = 1$ and $TSR = 8$. A NACA $a = 0.8$ mean line distribution was assumed for the camber, and a table with the data associated to this camber distribution has been included in Appendix C.1. The camber and maximum thickness distributions were adopted to match the criteria used in an experiment with a 3-bladed marine current turbine carried out in the University of Southhampton in the United Kingdom (Bahaj et al., 2007, [4]). This geometry was also used by Xu (2010) [52], who analyzed the turbine using several CFD models. Finally, the thickness distribution chosen was NACA 66, and the its data can be found in Appendix C.2.

No hub model was used for the LLOPT-FWA model, so both the input circulation and the one calculated with the VLM and BEM models go to zero at the hub. The geometry is generated in PROPCAV with 20 spanwise and 60 chordwise elements. The blade sections' dimensions are interpolated from 17 input control points. MPUF's geometry is formed by 27 spanwise and 20 chordwise panels, unless otherwise indicated. Figure 4.19 presents the geometries generated by both models. The MPUF-3A geometry coincides with the mean camber line of the PROPCAV geometry.

A two-bladed hub-less case has also been analyzed with the MPUF-3A and PROPCAV models, and the results are presented in Figure 4.23. The same case has been analyzed for a turbine with an infinite hub using the VLM model, and the resulting geometry is presented in Figure 4.20. It is not possible

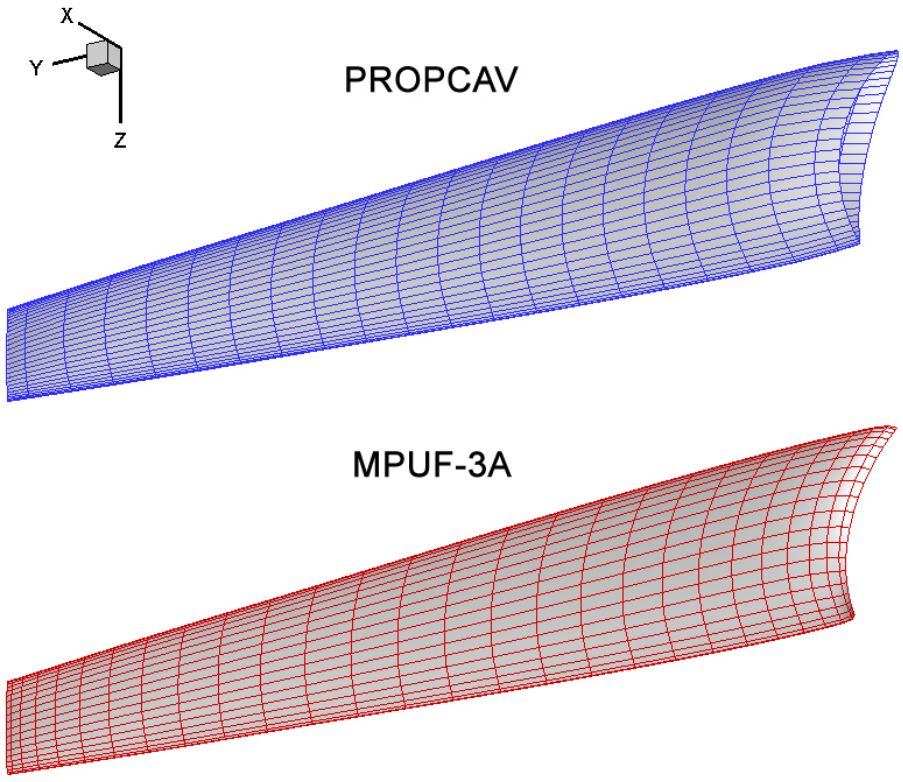

Figure 4.19: Comparison of blade geometries; vortex-lattice method (MPUF-3A) and boundary element method (PROPCAV); $Z = 1$, $TSR = 8$, based on optimum loading as determined by unconstrained LLOPT-FWA.

at the moment to analyze a turbine with a hub with PROPCAV, because its wake alignment routine has yet to be updated for turbines.

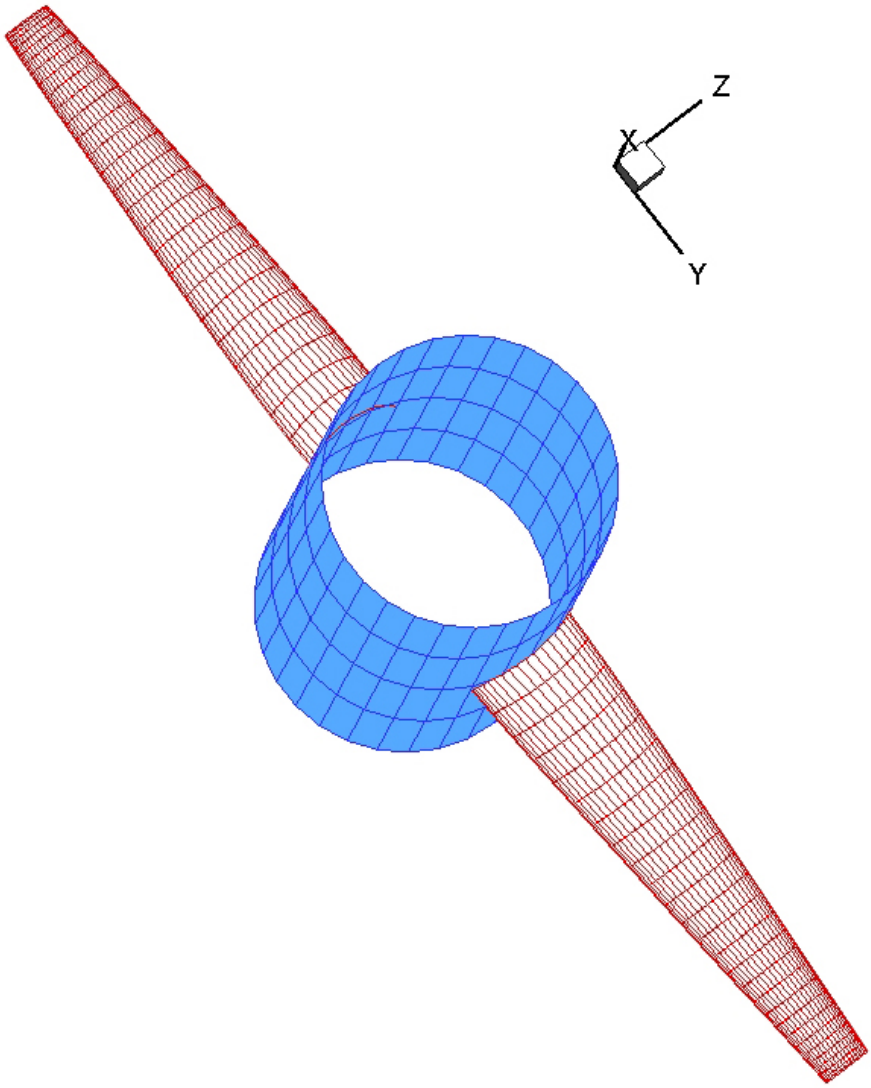

Figure 4.20: Blade geometry for a two-bladed turbine with hub, based on optimum loading as determined by constrained LLOPT-FWA. ($Z = 2, TSR = 4$)

4.1.5 Analysis with VLM and BEM

PROPCAV's alignment routine is comparable to that used by LLOPT-FWA, but the final wake shape depends on the circulation distribution obtained through the analysis of the input geometry. Thus, differences are expected, in particular in the zones of the wake located far from the rotor. MPUF-3A uses a simpler wake alignment, and it can only represent up to two revolutions of the turbine. Figure 4.21 shows the intersection of the different wakes with an xz plane at $y = 0$. The unaligned wake (geometric pitch alignment) is depicted in blue.

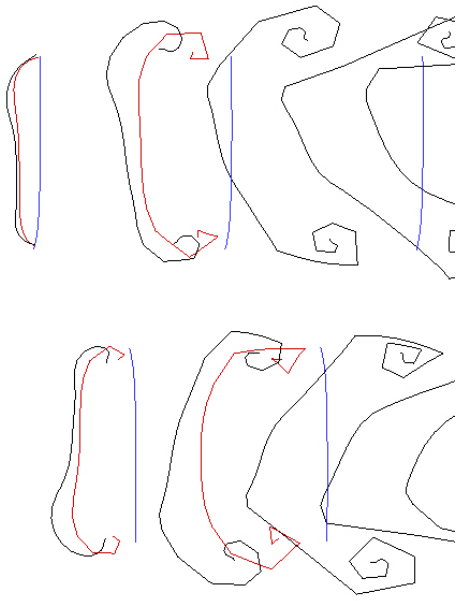

Figure 4.21: Comparison of wake geometries; slice of the wake at an xz plane at $y = 0$. LLOPT-FWA wake in black; PROPCAV aligned wake in red, MPUF-3A unaligned wake (geometric pitch) in blue.

The MPUF-3A model has the capability of considering the effect of thickness on the blade loading, but it has not been included in the results presented in this section. To measure the effect of the blade thickness on the PROPCAV results, the overall thickness can be modified through the use of the thickness coefficient t_f. A thickness factor of 0.25, for instance, represents a reduction of 75% of the blade thickness.

Figure 4.22 presents a comparison of circulation distributions for LLOPT-FWA and the PROPCAV and MPUF-3A models.

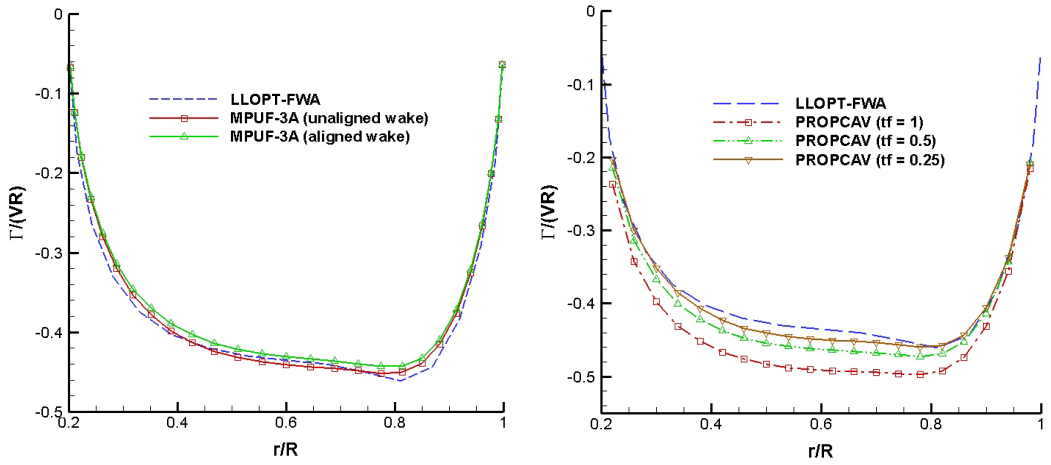

(a) MPUF-3A, with and without alignment

(b) PROPCAV, with alignment and varying t_f

Figure 4.22: Comparison of circulation distributions between the input optimal circulation (unconstrained LLOPT-FWA) and the one calculated from the designed blade (MPUF-3A and PROPCAV). ($Z = 1$, $TSR = 8$). The corresponding efficiencies are presented in Table 4.6.

MPUF-3A recovers the original circulation distribution with significant accuracy, both with or without wake alignment. PROPCAV's loading is con-

siderably higher for the full-thickness alternative, but approaches MPUF-3A's solution as t_f decreases, as expected. In general terms, the results appear to validate the methodology used for the design of the blade geometry.

The efficiencies obtained with MPUF-3A and PROPCAV are in all cases lower than the one calculated with LLOPT-FWA. Table 4.6 summarizes the results, as well as the absolute difference with respect to LLOPT-FWA.

Numerical model	Efficiency	Absolute difference
LLOPT-FWA	46.71%	
MPUF-3A (unaligned)	45.16%	-1.55%
MPUF-3A (aligned)	43.21%	-3.50%
PROPCAV ($t_f = 1$)	43.08%	-3.63%
PROPCAV ($t_f = 0.5$)	43.58%	-3.13%
PROPCAV ($t_f = 0.25$)	44.99%	-1.72%

Table 4.6: Comparison of efficiencies as calculated by different models. Absolute difference with respect to LLOPT-FWA model. ($Z = 1$, $TSR = 8$)

For the two-bladed hub-less case, MPUF3A produces a slightly lower loading, but recovers the overall shape. Figure 4.23a presents the circulation distribution for two different discretizations. Even though there is no significant change in the loading, the value obtained for the K_Q parameter (and thus the overall efficiency) varies significantly depending on the number of panels used. This is a known issue of the MPUF-3A model, and should be analyzed further.

Figure 4.23b shows the results for the blade as analyzed by the PROPCAV model, for three different values of the thickness factor t_f. As before,

the results approach the loading for the zero-thickness model as the thickness decreases. However, for the case $t_f = 0.25$ the model failed for low number of panels, and it was necessary to use a finer panel grid. The convergence of the results for different discretization alternatives is shown in Figure 4.24.

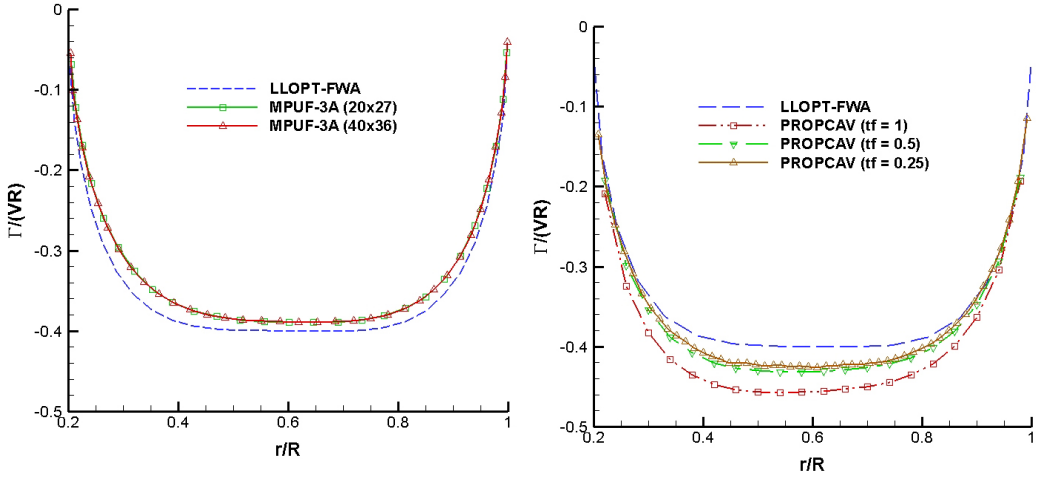

(a) MPUF-3A, varying number of panels

(b) PROPCAV, varying t_f

Figure 4.23: Comparison of circulation distributions between the input optimal circulation (constrained LLOPT-FWA) and the one calculated from the designed blade (MPUF-3A and PROPCAV). ($Z = 2$, $TSR = 4$)

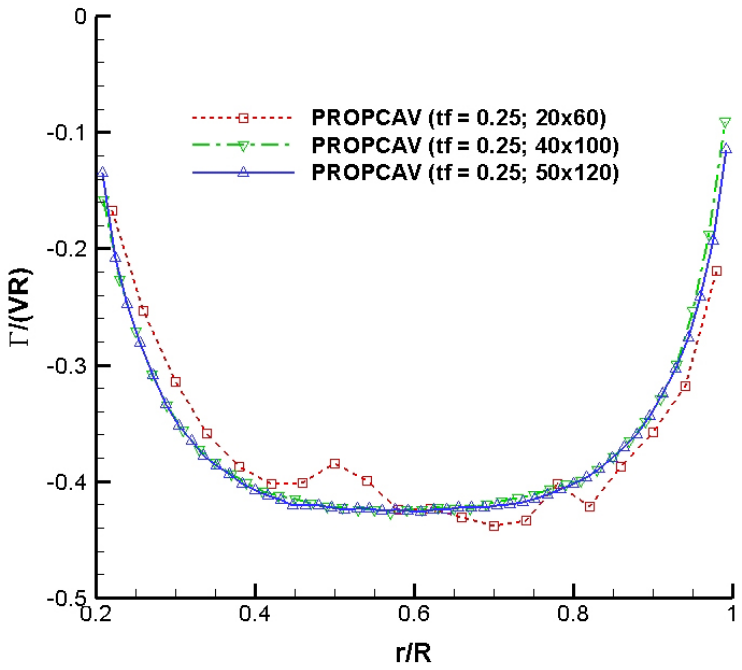

Figure 4.24: Comparison of circulation distributions for thickness factor $t_f = 0.25$ and varying number of panels

As mentioned in Section 4.1.4, the aligment subroutine used by PROPCAV is not at the moment compatible with turbine with hub, so only MPUF-3A was used to analyze the geometry presented in Figure 4.20. An infinite hub model was used, and results are shown in Figure 4.25. Once more the use of a finer grid of panels on the blade produces an efficiency that is closer to the one calculated by the constrained LLOPT-FWA model, as summarized in Table 4.7.

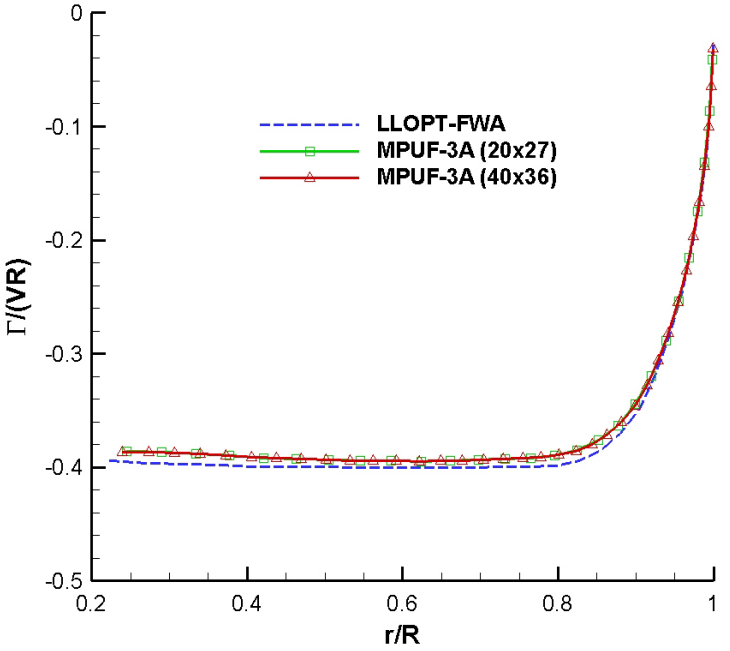

Figure 4.25: Comparison of circulation distributions between the input optimal circulation (constrained LLOPT-FWA) and the one calculated from the designed blade using the MPUF-3A model for a turbine with hub ($Z = 2$, $TSR = 4$). The corresponding efficiencies are presented in Table 4.7.

Numerical model	Efficiency	Absolute difference
LLOPT-FWA	45.12%	
MPUF-3A (20×27)	40.98%	-4.14%
MPUF-3A (40×36)	43.62%	-1.50%

Table 4.7: Comparison of efficiencies as calculated by MPUF-3A for the case of a two-bladed turbine with hub. Absolute difference with respect to LLOPT-FWA model. ($Z = 2$, $TSR = 4$)

4.2 Propellers

4.2.1 LLOPT-LW

To verify the accuracy of the method the results were compared to those presented in Kerwin's class notes (2001) [20] for his PLL model. The results presented in Figure 4.26 have been normalized with respect to the maximum circulation value, and show a good agreement for all cases. It is worth pointing out that Kerwin used constant spacing, so the accuracy of the solution near the tip and the hub is low.

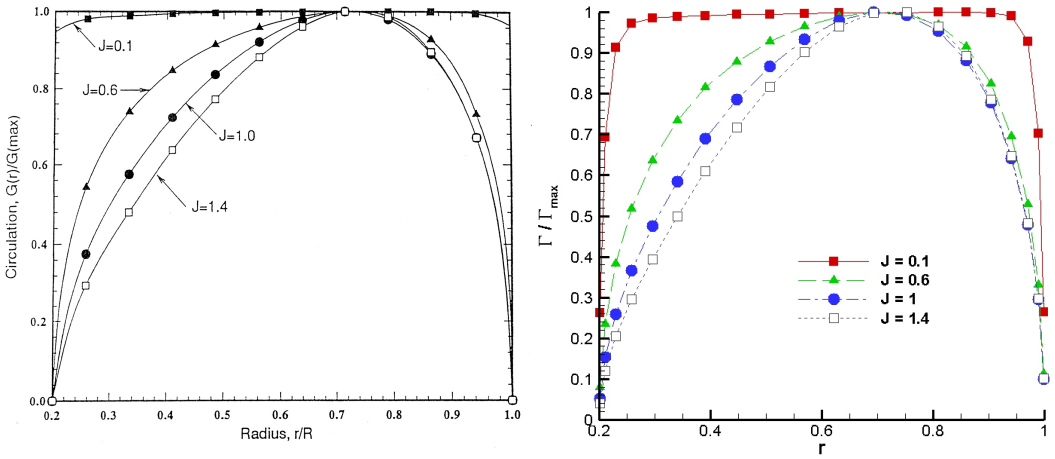

(a) PLL

(b) LLOPT-LW

Figure 4.26: Comparison of results for circulation distribution ($C_T = 0.512$, $Z = 5$). PLL results from class notes by Kerwin [20]

The convergence of the LLOPT-LW model with regards to the number of spanwise elements was studied. Even though some small differences can be seen in the induced velocities distributions, the resulting circulation distributions converge with great accuracy even for $M = 10$. Figure 4.27 compares

the results for three values of M (10, 20 and 30) for each model, both with or without the hub model.

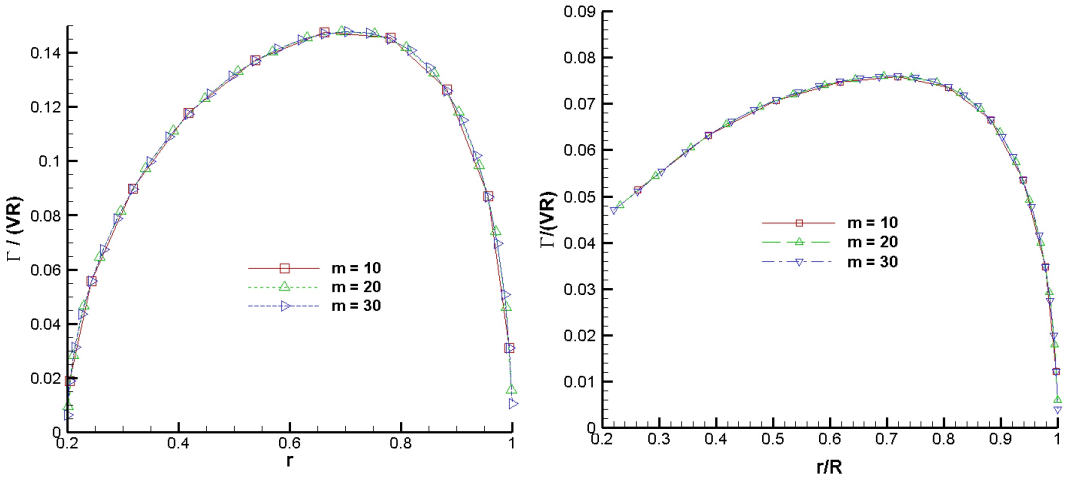

(a) No hub
($J = 0.7$, $Z = 5$, $C_T = 0.8$)

(b) With hub
($J = 0.6$, $Z = 5$, $C_T = 0.512$)

Figure 4.27: Comparison of circulation distributions for different M, LLOPT-LW model

Table 4.8 gathers the propeller efficiencies for the LLOPT-LW method and different combinations of the thrust and advanced coefficients. The Lerbs-Wrench model does not converge for high-C_T, high J cases, so no efficiency can be estimated. It might be possible to solve the convergence issues in these cases through under-relaxation or the use of non-linear solvers, but no such solution has been attempted. Table 4.9 presents the equivalent results for the case of a propeller with hub. It is worth noting that these efficiencies do not consider the additional drag caused by the presence of the hub vortex.

	C_T								
J	0.6	0.8	1.0	1.2	1.4	1.6	1.8	2.0	2.2
0.1	87.66%	84.62%	81.81%	79.35%	77.12%	75.06%	73.16%	71.39%	69.74%
0.2	87.23%	84.12%	81.37%	78.91%	76.69%	74.67%	72.83%	71.13%	69.56%
0.3	86.74%	83.50%	80.63%	78.06%	75.74%	73.63%	71.69%	69.90%	68.25%
0.4	86.14%	82.74%	79.74%	77.04%	74.60%	72.38%	70.33%	68.45%	66.72%
0.5	85.43%	81.85%	78.68%	75.83%	73.24%	70.88%	68.71%	66.70%	64.83%
0.6	84.61%	80.81%	77.44%	74.39%	71.63%	69.10%	66.76%	64.58%	62.55%
0.7	83.68%	79.62%	76.00%	72.72%	69.73%	66.98%	64.43%	62.03%	59.78%
0.8	82.61%	78.25%	74.34%	70.78%	67.51%	64.47%	61.62%	58.93%	56.36%
0.9	81.42%	76.70%	72.44%	68.53%	64.90%	61.47%	58.21%	55.05%	51.95%
1.0	80.08%	74.95%	70.26%	65.90%	61.77%	57.79%	53.86%	49.86%	45.54%
1.1	78.58%	72.95%	67.73%	62.78%	57.93%	53.01%	47.66%		
1.2	76.91%	70.68%	64.77%	58.95%	52.87%				
1.3	75.04%	68.07%	61.21%	53.93%					
1.4	72.93%	65.00%	56.67%						

Table 4.8: Efficiencies for LLOPT-LW model, hub-less propeller ($Z = 5$)

	C_T								
J	0.6	0.8	1.0	1.2	1.4	1.6	1.8	2.0	2.2
0.1	87.68%	84.60%	81.89%	79.45%	77.22%	75.17%	73.28%	71.52%	69.87%
0.2	87.33%	84.23%	81.49%	79.05%	76.86%	74.86%	73.04%	71.37%	69.83%
0.3	86.86%	83.65%	80.80%	78.25%	75.94%	73.84%	71.91%	70.13%	68.47%
0.4	86.30%	82.93%	79.95%	77.27%	74.85%	72.64%	70.61%	68.74%	67.00%
0.5	85.62%	82.07%	78.93%	76.10%	73.53%	71.19%	69.03%	67.02%	65.18%
0.6	84.83%	81.07%	77.72%	74.71%	71.96%	69.45%	67.12%	64.96%	62.94%
0.7	83.92%	79.91%	76.32%	73.08%	70.11%	67.38%	64.84%	62.46%	60.23%
0.8	82.88%	78.58%	74.71%	71.18%	67.94%	64.93%	62.10%	59.43%	56.88%
0.9	81.72%	77.07%	72.85%	68.99%	65.39%	62.00%	58.78%	55.66%	52.62%
1.0	80.41%	75.35%	70.72%	66.42%	62.35%	58.43%	54.57%	50.64%	46.47%
1.1	78.96%	73.41%	68.27%	63.39%	58.63%	53.82%	48.66%		
1.2	77.33%	71.20%	65.39%	59.68%	53.77%				
1.3	75.50%	68.66%	61.94%	54.89%					
1.4	73.46%	65.69%	57.60%						

Table 4.9: Efficiencies for LLOPT-LW model, propeller with hub ($Z = 5$)

4.2.2 LLOPT-FWA

The effect of numerical error has been analyzed in Section 3.3.3, modeling a dummy wake geometry that meets the assumptions of the Lerbs-Wrench formulas. The induced velocities calculated with this method are very similar to those obtained through the asymptotic formulas, which can be considered an exact solution for that particular case.

Like for the model LLOPT-LW in Section 4.2.1, the convergence of the LLOPT-FWA model when used for turbine optimization has been studied. Figure 4.28 compares the results for the optimum circulation distribution for different number of spanwise elements. It can be seen that the results are very similar, even using as few as 10 control points.

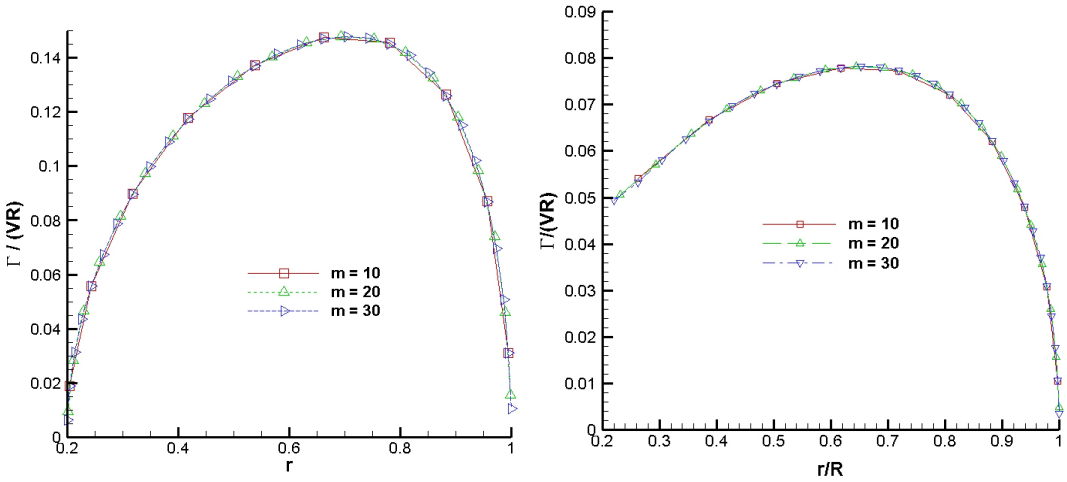

(a) No hub
($J = 0.7$, $Z = 5$, $C_T = 0.8$)

(b) With hub
($J = 0.6$, $Z = 5$, $C_T = 0.512$)

Figure 4.28: Comparison of circulation distributions for different M, LLOPT-FWA model

Table 4.10 summarizes the efficiencies for the Full Wake Alignment model, for the same combination of parameters used in Table 4.8. Even though this model does converge to a solution for some of the high-C_T, high-J cases that the LLOPT-LW model failed at, those results are not included in order to simplify the comparison. Table 4.11 presents the results for the case of propellers with hub, not taking into account the increased drag originated by the hub vortex.

The use of the full wake alignment model results in aligned geometries that differ considerably from the constant-pitch helix that the Lerbs-Wrench formula assumes. Figure 4.29 shows the 3D geometry of the key blade's wake and a vertical slice of the complete wake for a five-bladed hub-less propeller and two different values of the advance coefficient J. As J becomes higher, the variation of the pitch along the blade and the strength of the roll-up grows increase. Choosing a larger design thrust also causes the roll-up to be magnified, thus moving further away from the theoretical helical wake surface.

	C_T								
J	0.6	0.8	1.0	1.2	1.4	1.6	1.8	2.0	2.2
0.1	87.58%	84.44%	81.64%	79.11%	76.81%	74.70%	72.76%	70.95%	69.27%
0.2	87.04%	83.77%	80.85%	78.21%	75.80%	73.59%	71.55%	69.66%	67.89%
0.3	86.44%	83.03%	79.97%	77.21%	74.70%	72.39%	70.26%	68.28%	66.44%
0.4	85.78%	82.19%	78.98%	76.08%	73.43%	71.00%	68.76%	66.67%	64.73%
0.5	84.98%	81.17%	77.75%	74.66%	71.83%	69.23%	66.82%	64.58%	62.49%
0.6	84.07%	80.00%	76.33%	72.99%	69.94%	67.12%	64.52%	62.09%	59.82%
0.7	83.02%	78.63%	74.66%	71.04%	67.72%	64.64%	61.77%	59.08%	56.56%
0.8	81.83%	77.08%	72.77%	68.81%	65.16%	61.76%	58.57%	55.56%	52.70%
0.9	80.50%	75.33%	70.61%	66.25%	62.20%	58.39%	54.80%	51.38%	48.10%
1.0	79.01%	73.37%	68.17%	63.33%	58.78%	54.46%	50.32%	46.29%	42.29%
1.1	77.37%	71.17%	65.41%	59.97%	54.77%	49.71%	44.70%		
1.2	75.55%	68.70%	62.24%	56.02%	49.90%				
1.3	73.52%	65.91%	58.57%	51.25%					
1.4	71.27%	62.72%	54.18%						

Table 4.10: Efficiencies for LLOPT-FWA model, hub-less propeller ($Z = 5$)

	C_T								
J	0.6	0.8	1.0	1.2	1.4	1.6	1.8	2.0	2.2
0.1	87.49%	84.34%	81.52%	78.98%	76.66%	74.54%	72.58%	70.76%	69.07%
0.2	86.97%	83.69%	80.76%	78.11%	75.70%	73.49%	71.45%	69.56%	67.79%
0.3	86.37%	82.93%	79.86%	77.08%	74.56%	72.22%	70.08%	68.06%	66.07%
0.4	85.66%	82.04%	78.79%	75.85%	73.15%	70.70%	68.41%	66.24%	64.43%
0.5	84.85%	81.00%	77.55%	74.42%	71.57%	69.98%	66.53%	64.24%	62.13%
0.6	83.92%	79.81%	76.11%	72.73%	69.66%	66.83%	64.21%	61.76%	59.49%
0.7	82.88%	78.45%	74.46%	70.82%	67.48%	64.38%	61.52%	58.84%	56.33%
0.8	81.70%	76.93%	72.59%	68.63%	64.97%	61.58%	58.40%	55.39%	52.55%
0.9	80.39%	75.21%	70.48%	66.12%	62.07%	58.28%	54.71%	51.31%	48.07%
1.0	78.93%	73.28%	68.09%	63.26%	58.73%	54.44%	50.32%	46.34%	42.41%
1.1	77.32%	71.13%	65.38%	59.97%	54.80%	49.82%	44.87%		
1.2	75.53%	68.71%	62.28%	56.11%	50.06%				
1.3	73.55%	65.97%	58.68%	51.47%					
1.4	71.34%	62.85%	54.41%						

Table 4.11: Efficiencies for LLOPT-FWA model, propeller with hub ($Z = 5$)

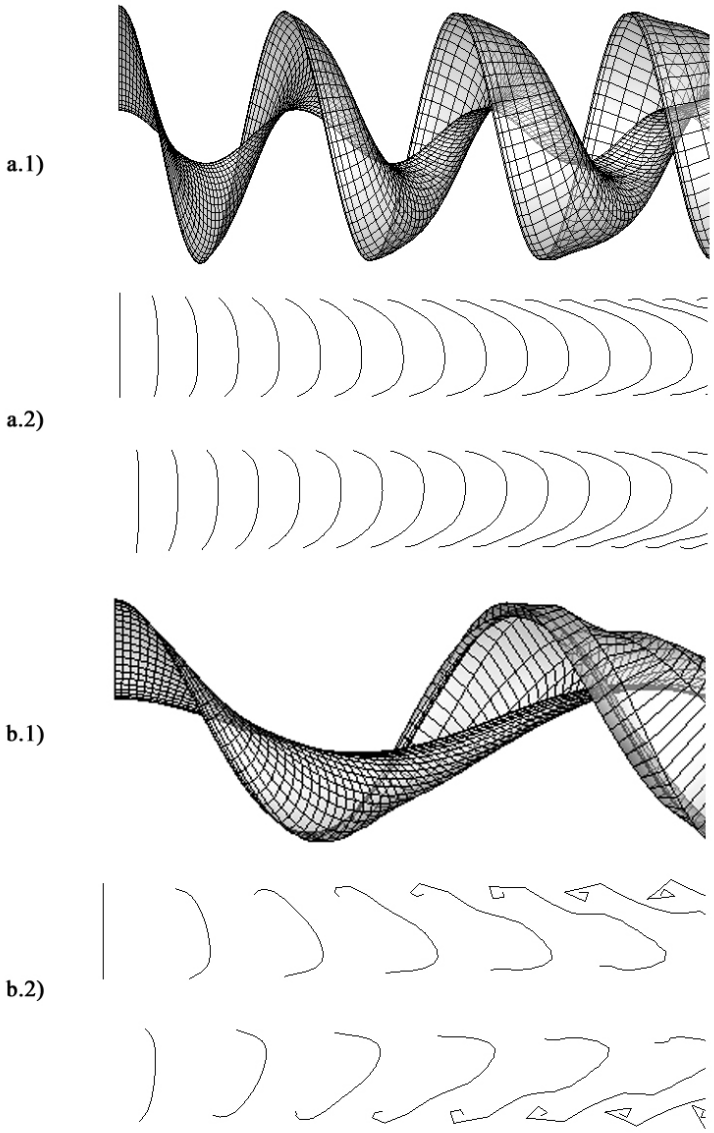

Figure 4.29: Wake geometry corresponding to the optimum circulation distribution for a propeller, $Z = 5$, $C_T = 0.512$, different J. a.1) $J = 0.6$, key blade; a.2) $J = 0.6$, all blades (cross section with respect to y axis); b.1) $J = 1.4$, key blade; b.2) $J = 0.6$, all blades (cross section with respect to y axis)

4.2.3 Comparison of Results

Unlike for turbines, the optimum circulation distributions obtained with both methods are in general markedly similar. For high advance ration J and/or low thrust coefficient, the moderately loaded propeller assumption proves more accurate, and as expected the circulation distributions corresponding to these combinations of parameters are very close for both methods.

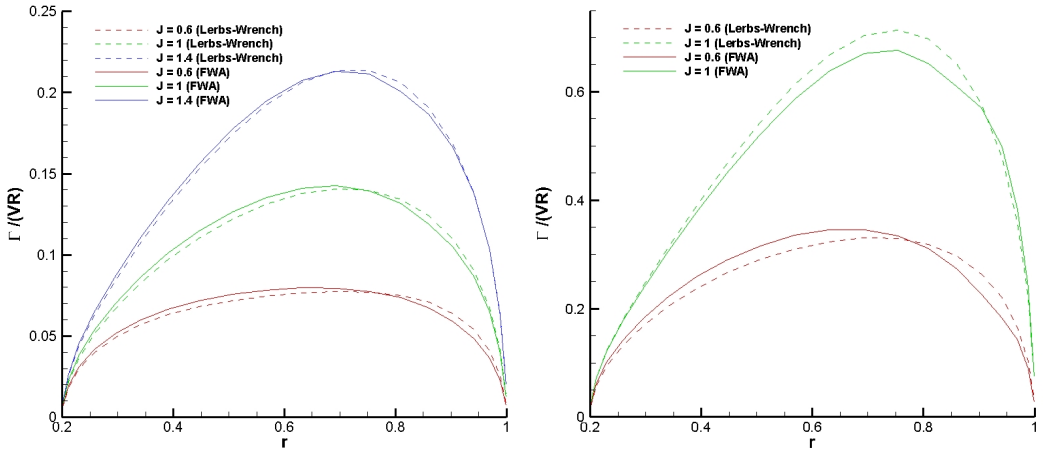

(a) $C_T = 0.512$ (b) $C_T = 2$

Figure 4.30: Comparison of optimum circulation distributions for different advance ratios J and design thrust C_T; $Z = 5$

As can be observed in Figure 4.30, in almost all cases the loading for the LLOPT-LW model is distributed slightly more towards the tip of the blade. The differences observed in the circulation distribution also increase as the number of blades grows, with all other parameters kept constant (see Figure 4.31).

The FWA model results as shown in Section 4.2.2 in a wake shape far

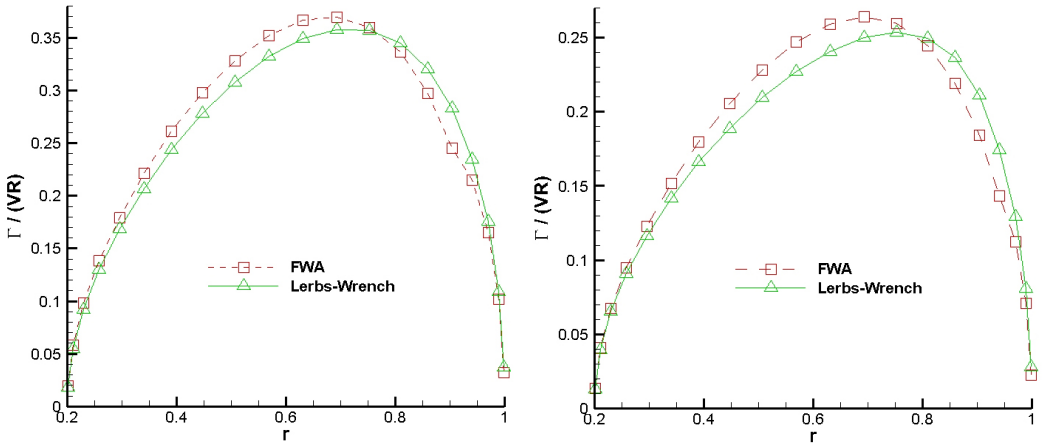

(a) $Z = 5$ (b) $Z = 7$

Figure 4.31: Comparison of optimum circulation distributions for different number of blades Z

removed from the original assumption of helicoidal, constant-pitch wake used for the Lerbs-Wrench model. As a direct consequence, the axial and tangential induced velocities on the key blade are not as smooth as in the previous model (see Figures 4.32 and 4.33), in particular near the tip. The bigger differences are in the axial induced velocities, and they are largely responsible for the variations in the estimated efficiencies.

The differences in the induced velocities are more significant for high values of the C_T coefficient. Furthermore, as the thrust increases the peak in the tangential velocities moves towards the tip of the blade, as can be seen in Figure 4.33.

It has been found that the Lerbs-Wrench model returns negative values of induced axial velocity at the hub for high-thrust, high-advance coefficient

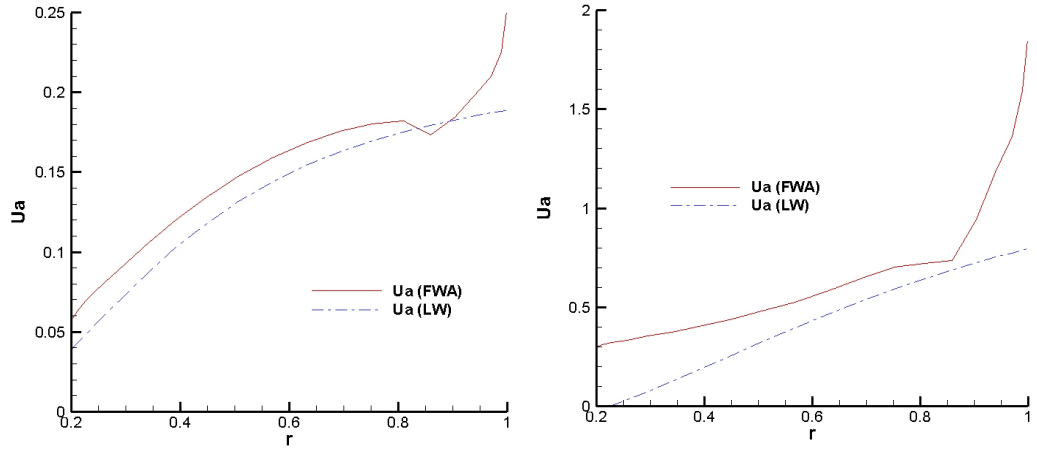

(a) $C_T = 0.512$ (b) $C_T = 2$

Figure 4.32: Comparison of induced axial velocities u_a on the key blade, $J = 1$, $Z = 5$, different C_T

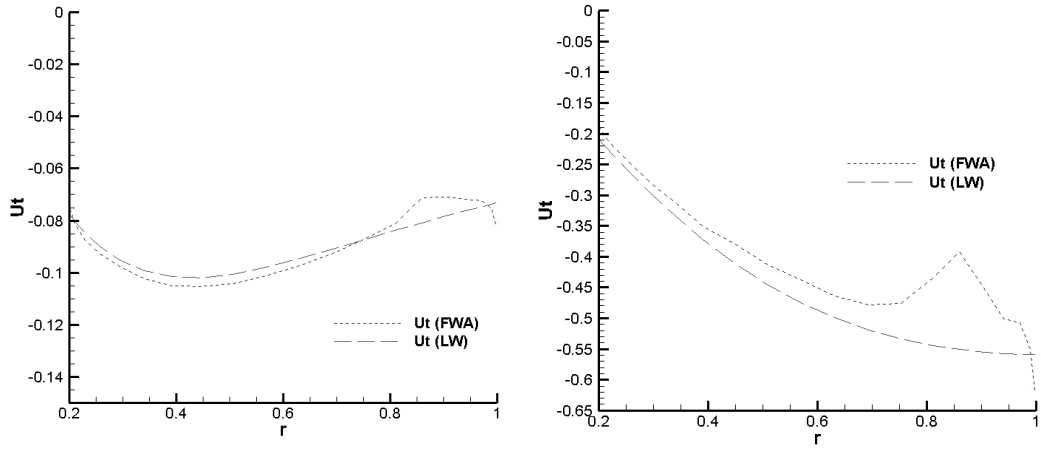

(a) $C_T = 0.512$ (b) $C_T = 2$

Figure 4.33: Comparison of induced tangential velocities u_t on the key blade, $J = 1$, $Z = 5$, different C_T

cases. This behavior is not present in the converged solutions for the LWA model.

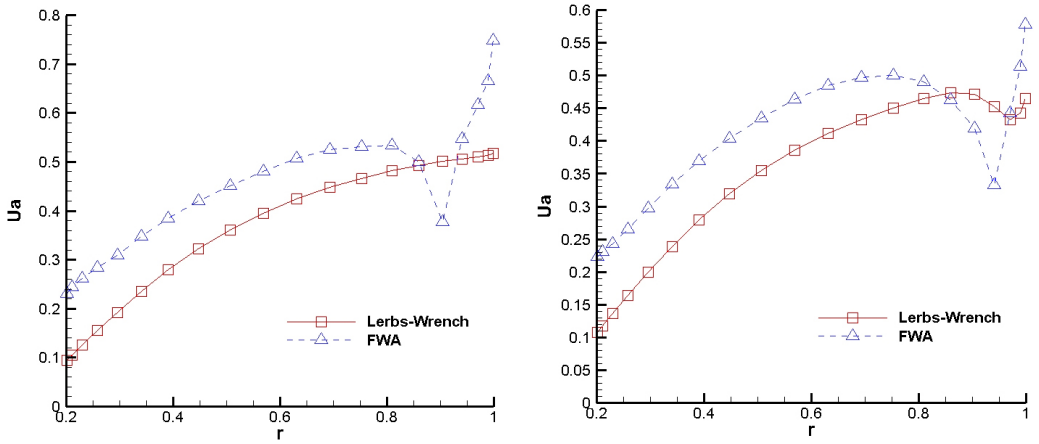

(a) $Z = 5$ (b) $Z = 7$

Figure 4.34: Comparison of induced axial velocities u_a on the key blade, $J = 0.7$, $C_T = 1.8$, different Z

Figure 4.34 compares the induced axial velocities obtained through both methods. Two propellers were with equivalent design parameters were analyzed, varying the number of blades Z. In both cases the results varied greatly between both methods, and the 5-blade propeller appears to have more constant velocities along the key blade.

At very low advance coefficients, the optimum circulation distribution resembles that of the actuator disk. As J approaches 0, both models turn out almost equivalent solutions, and they approach the Betz limit as defined in equation 3.52. Figure 4.35 shows that the differences in estimated efficiency increase as the thrust coefficient chosen grows.

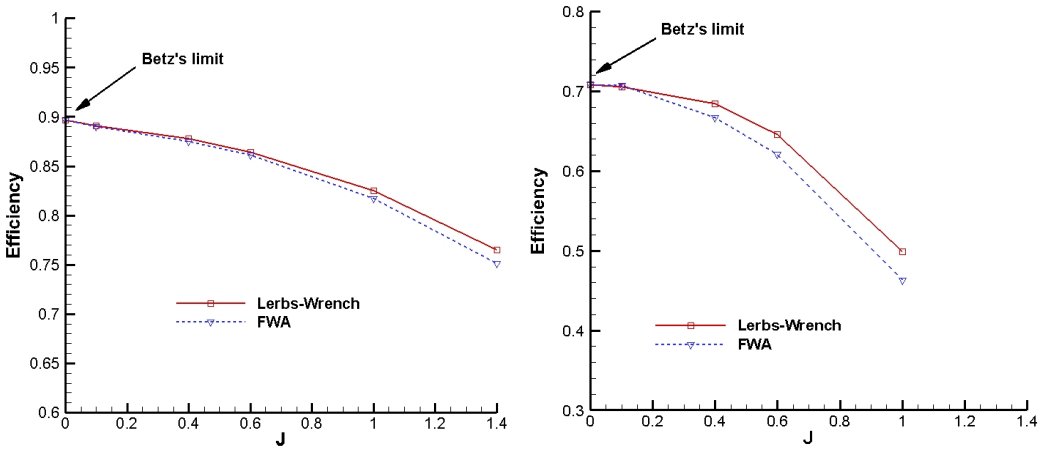

(a) $C_T = 0.512$ (b) $C_T = 2$

Figure 4.35: Comparison of efficiencies for both methods at different J, $Z = 5$, different C_T

The results obtained for both models suggest that the use of the Lerbs-Wrench formulas causes an overestimation of the propeller efficiency. The prediction obtained through the simpler model becomes progressively worse as the thrust and advance coefficients increase.

Figure 4.36 shows the relative error as calculated by both methods, assuming that the FWA model provides a more accurate value. In order to present a smooth profile, the results have been interpolated with a cubic surface. Figure 4.37 shows the corresponding relative errors in the case a hub model is used.

The absolute differences in efficiency range from 0 to 4% for five bladed propellers up to $C_T = 2.2$. The use of surface maps such as the one presented in Figure 4.36 could become an useful tool in determining whether the use of

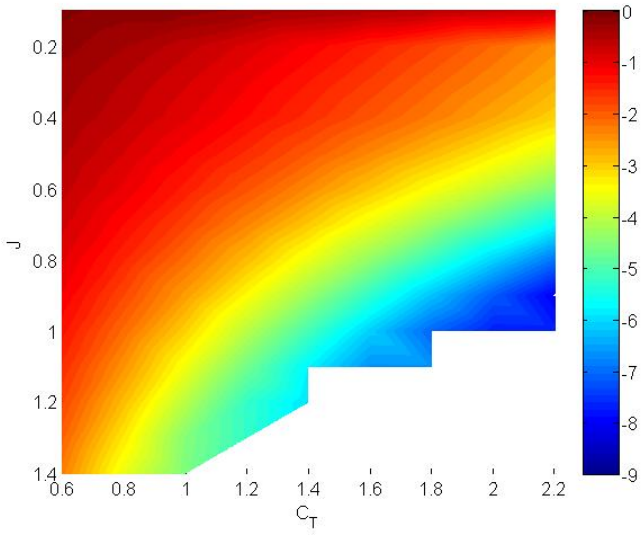

Figure 4.36: Relative error of efficiencies as calculated by both methods. Values expressed in percentages (%), for a hub-less five-bladed propeller

full-wake alignment is justified for a given set of flow and propeller geometry parameters.

Just as the turbine optimization Lerbs-Wrench model does, the propeller LLOPT-LW model suffers from stability issues for certain combinations of flow and turbine parameters. Even though good convergence can be achieved in many cases within three or four wake alignment iterations, attempting further refinement of the solution can lead to instability. Figure 4.38a presents a typical case, in which every iteration after the sixth moves farther away from the converged solution.

The efficiency values included in Table 4.8 were taken from the iteration for which the convergence criterion utilized (root mean square of circulation

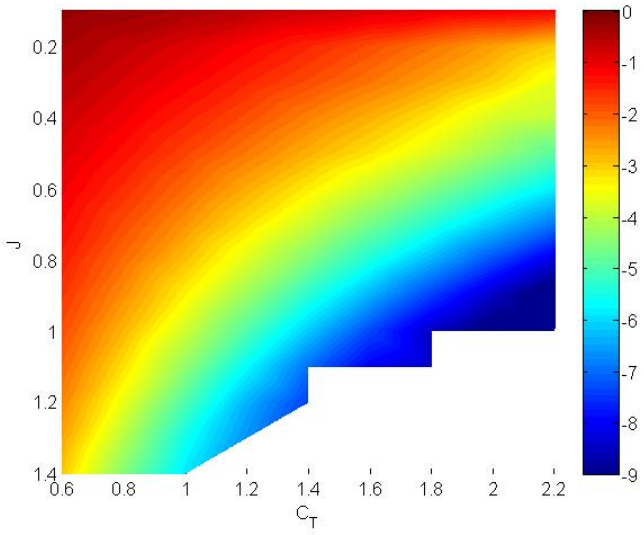

Figure 4.37: Relative error of efficiencies as calculated by both methods. Values expressed in percentages (%), for a five-bladed propeller with infinite hub

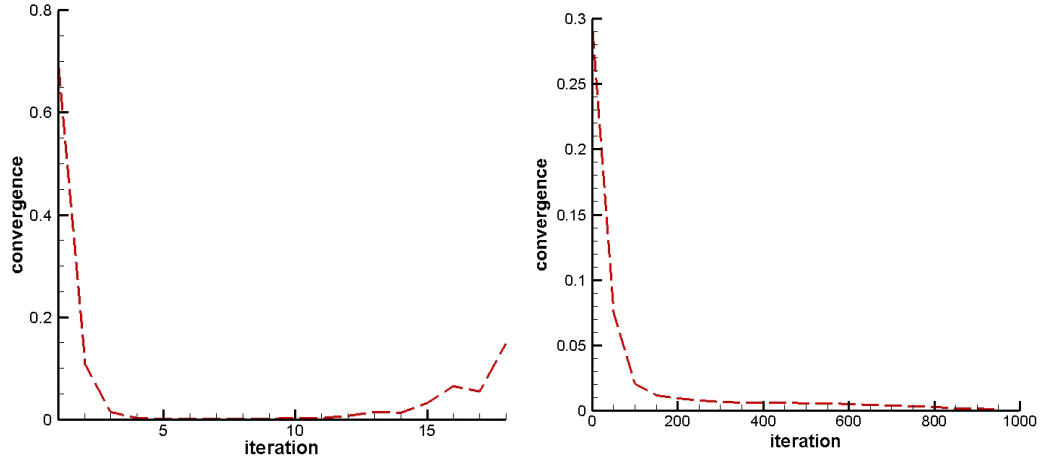

(a) LLOPT-LW

(b) LLOPT-FWA

Figure 4.38: Convergence of both models with number of iterations ($J = 0.4$, $Z = 5$, $C_T = 2$)

difference vector) was minimum. The Full Wake Alignment model does not present from these convergence issues, as shown in Figure 4.38b.

As in the case of turbines, classical propeller optimization is based on Betz' condition as defined in Section 3.1.3 by Equation 3.26. Figure 4.39 compares this ratio as calculated for the optimum solutions of LLOPT-LW and the LLOPT-FWA models, for a five-bladed propeller with hub and different values of the parameters C_T for a given advance ratio J. It can be seen that the Lerbs-Wrench model approximates a constant ratio, in particular as C_T decreases. On the other hand, the Full Wake Alignment model shows a significant variation from the mean value, in particular near the hub and the tip of the blade for high C_T.

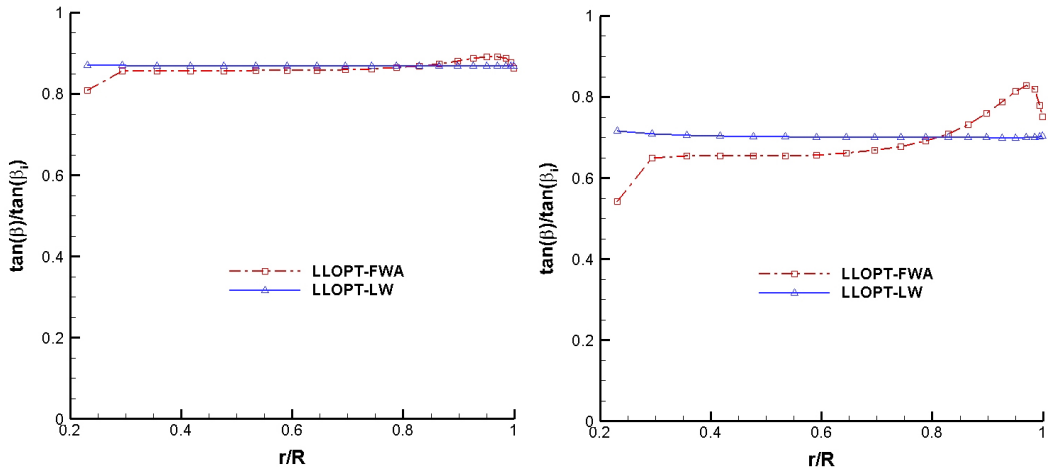

(a) $C_T = 0.6$ (b) $C_T = 2$

Figure 4.39: Ratio between the aligned pitch angle β_i and the geometric pitch angle β, for different values of C_T. ($Z = 5$, $J = 0.3$)

Chapter 5

Conclusions and Recomendations

5.1 Conclusions

This thesis presents a lifting line optimization model for marine current turbines and propellers, coupled with two different wake alignment models: a simple alignment based on the Lerbs-Wrench formulas (LLOPT-LW) and an iterative full wake alignment procedure (LLOPT-FWA). The numerical calculation of influence coefficients is verified by comparison with simple cases for which a solution is known. It has been shown that the use of an aligned wake geometry produces results that differ considerably from those obtained through the classical Lerbs-Wrench model. Furthermore, while a reasonable assumption for propellers, the use of a moderately loaded propeller approach appear to be insufficient for the optimization of turbines.

The wake alignment procedure generates a local increase in the circulation near the tip, potentially not compatible with optimum structural and hydraulic design. The inclusion of viscosity in the formulation results in the improvement or outright removal of this singular behavior. The use of Glauert series or polynomials in order to represent circulation distributions achieves increased stability of the alignment procedure for low-TSR, low-Z cases. How-

ever, it proves insufficient for high-TSR cases. Constrained optimization results in smoother circulation distributions, but further validation of the results is necessary. Unlike the original linear formulation, the LLOPT-FWA model, in all its variants, approaches the Betz limit for large number of blades and for high tip speed ratios. The model is also stable for low TSR cases, and shows good convergence for increasing number of elements.

A preliminary design procedure is then presented and the specified optimum circulation distribution is compared to that from applying more complex methods on the designed blade geometry. The use of a vortex lattice method (MPUF-3A) and a boundary element method (PROPCAV) allows us to corroborate the geometry generated and analyze complex flow conditions. Pressure distributions on the blade and a more accurate prediction of the turbine's performance can also be obtained, as well as the effect of different thickness and camber distributions.

In the case of propellers, the effects of wake alignment on the optimization procedure are tested for different combinations of design parameters. It is shown that the impact of wake alignment increases as advance coefficient, number of blades and design thrust coefficient increase. The use of full wake alignment also partially solves the convergence stability issues that the simpler model suffers from for certain combinations of parameters. Surface maps were created in order to better illustrate the precision of the moderately loaded propeller assumption.

5.2 Recommendations

The constrained optimization algorithm presented in this thesis has yet to be extended to target functions $\Gamma(r)$ with more than five modes. The selection of weight increments needs to be studied in order to better approximate the unconstrained solution near the tip and the hub in hubless turbines, or just near the tip in turbines with hub. The use of functional representations such as Glauert series or polynomials is also not strictly necessary, and a similar approach could be achieved for the discrete optimization alternative through numerical derivatives.

Furthermore, the computational time required for each run of the LLOPT-FWA model can reach approximately 24 CPU hours in a modern computer. For an 8-CPU node, this represents 3 hours of real time. In order to optimize this process, alternatives for the alignment procedure must be analyzed. One such alternative could be the modification of the code so that the entire wake is not updated in each iteration, and instead the far wake's pitch is kept constant for several iterations, thus reducing the number of calculations needed. Another idea would be the use a coarser grid in the wake, regardless of the number of control points on the blade, and this has already been included as an option for propellers on the latest version of the PROPCAV model. Finally, it would be possible to align a shorter wake and then complement these results with an actuator disk model downstream of the wake, forming an "ultimate wake". These potential improvements all fall under the category of *Partial Wake Alignment* models.

A non-linear formulation was proposed in Appendix A for the LLOPT-LW model. In cases when convergence is achieved with the linear optimization algorithm, the variation of the results when small changes of the circulation distribution are imposed should be studied. This would allow the development of a non-linear LLOPT-FWA model, although the total computational time required could be prohibitive.

The blade geometry generation routine can be expanded to consider the effects of cavitation in determining the blade chord distribution, via the blade optimization model of Mishima and Kinnas (1997) [41], as was most recently applied in the case of turbines by Xu and Kinnas (2010) [53]. It is expected that the avoidance of cavitation on the blade will lead to a further reduction of the loading.

The viscous effects can be included in both the MPUF-3A and PROP-CAV models through the use of a friction coefficient C_f, constant on the entire blade surface. Greater accuracy can be achieved by coupling the potential flow methods with a boundary layer solver (see Sun and Kinnas, 2008 [47]).

For the case of propeller optimization, the stability issues observed for both methods (but more so in the LLOPT-LW model) in the case of certain combinations of parameters could in part be caused by the linearized solving of the non-linear system of equations, since this process depends to some extent on the initial guess used. A non-linear solver should be used instead, such as Newton-Raphson.

Appendices

Appendix A

Maximum Efficiency for a Constant-Loading Turbine

This formulation was carried out by Kinnas in private correspondence (2012, not published). Instead of the Lerbs-Wrench formulas presented in Section 3.3.1 we use the formulas for an infinite bladed lifting line from Kerwin (2001) [20]. In order to compare the formulation to the case for a turbine with a finite number of blades, the strength of the continuous circulation distribution can be written as the *finite* magnitude $Z\Gamma$. The induced velocities will then be:

For $r_c < r_v$:

$$\overline{u_a}(r_c, r_v) = \frac{Z\Gamma}{4\pi r_v \tan\beta_i} \tag{A.1}$$

$$\overline{u_t}(r_c, r_v) = 0 \tag{A.2}$$

For $r_c > r_v$:

$$\overline{u_a}(r_c, r_v) = 0 \tag{A.3}$$

$$\overline{u_t}(r_c, r_v) = \frac{Z\Gamma}{4\pi r_c} \tag{A.4}$$

where β_i is the pitch angle, r_c is the radial position of the control point and r_v represents the location of the vortex. A constant-loading disk can be inter-

preted as only two vortices: one at the tip and another at the center of the disk ($r_v = 0$). For a point at a position r between both vortices, we can then find an expression for the pitch angle as follows:

$$\tan\beta_i = \frac{V - u_a^*}{\omega r + u_t^*} = \frac{V - \frac{Z\Gamma}{4\pi R\tan\beta_i}}{\omega r + \frac{Z\Gamma}{4\pi r}}$$

We can then find an implicit expression for the pitch angle at the tip ($r = R$):

$$\begin{aligned}
\tan\beta_i &= \frac{V - \frac{Z\Gamma}{4\pi R\tan\beta_i}}{\omega R + \frac{Z\Gamma}{4\pi R}} \\
\omega R\tan\beta_i + \frac{Z\Gamma}{4\pi R}\tan\beta_i &= V - \frac{Z\Gamma}{4\pi R\tan\beta_i} \\
\frac{\omega R}{V}\tan\beta_i + \frac{Z\Gamma}{4\pi V R}\tan\beta_i &= 1 - \frac{Z\Gamma}{4\pi V R\tan\beta_i}
\end{aligned}$$

We define the Tip Speed Ratio as λ and a new adimensional coefficient A as follows:

$$\begin{aligned}
\mathrm{TSR} = \lambda &= \frac{\omega R}{V} \\
A &= \frac{Z\Gamma}{4\pi V R}
\end{aligned}$$

An implicit aligment equation can then be determined for the vortex at the tip (Equation A.5).

$$\lambda\tan\beta_i + A\tan\beta_i = 1 - \frac{A}{\tan\beta_i}$$

$$(\lambda + A)\tan\beta_i + \frac{A}{\tan\beta_i} = 1 \tag{A.5}$$

Now we seek an expression for the torque Q, as a function of the adimensional parameter A.

$$\begin{aligned} Q &= \rho Z \int_0^R (V - u_a^*)\Gamma r \, \mathrm{d}r \\ &= \rho Z V \Gamma \int_0^R r \, \mathrm{d}r - \rho Z \Gamma \int_0^R u_a^* \, \mathrm{d}r \\ &= \rho Z V \Gamma \frac{R^2}{2} - \rho Z \Gamma \int_0^R \frac{Z\Gamma}{4\pi R \tan\beta_i} r \, \mathrm{d}r \\ &= \rho Z V \Gamma \frac{R^2}{2} - \rho \frac{Z^2\Gamma^2}{4\pi R} \frac{1}{\tan\beta_i} \frac{R^2}{2} \end{aligned}$$

Operating and defining the adimensional torque $\overline{Q}$:

$$Q = \rho V^2 R^3 2\pi \left(A - \frac{A^2}{\tan\beta_i} \right)$$

$$\overline{Q} = \frac{Q}{2\pi\rho V^2 R^3} = \left(A - \frac{A^2}{\tan\beta_i} \right) \tag{A.6}$$

To maximize the torque, we differentiate $\overline{Q}$ with respect to the adimensional circulation coefficient A. This is equivalent to the optimization procedure described in Equation 3.22.

$$\frac{\partial \overline{Q}}{\partial A} = 0 \tag{A.7}$$

$$1 - \frac{2A}{\tan\beta_i} + \frac{A^2}{\tan^2\beta_i} \frac{\partial \tan\beta_i}{\partial A} = 0 \tag{A.8}$$

Equation A.8 can be linearized by ignoring its third term, an assumption equivalent to the one in Equation 3.23. The constant circulation on the blade can be then determined as a function of the pitch angle of the tip vortex:

$$1 - \frac{2A}{\tan\beta_i} \approx 0$$

$$A = \frac{\tan \beta_i}{2} \tag{A.9}$$

Replacing this expression into Equation A.6, we obtain a very simple relationship between the adimensional torque $\overline{Q}$ and the pitch angle β_i.

$$\overline{Q} = \left(\frac{\tan \beta_i}{2} - \frac{\tan^2 \beta_i}{4 \tan \beta_i} \right)$$

$$\overline{Q} = \frac{\tan \beta_i}{4} \tag{A.10}$$

We can determine an expression for the efficiency η using Equation 3.25. The general result in terms of the adimensional variables previously defined will be:

$$\eta = C_{pow} = \frac{Q\omega}{\frac{1}{2}\rho\pi V^3 R^2}$$

$$\eta = 4\overline{Q}\lambda \tag{A.11}$$

For the optimum value defined in Equation A.10, the efficiency can now be determined as a function of the rotational velocity and the pitch angle β_i.

$$\eta = \tan \beta_i \lambda \tag{A.12}$$

Equation A.5 can be used to find an expression for efficiency as a function of only the pitch angle. In general:

$$\tan \beta_i \lambda = 1 - \frac{A}{\tan \beta_i} - A \tan \beta_i$$

Then, for the optimum point given by Equation A.9:

$$\tan\beta_i\lambda = 1 - \frac{1}{2} - \frac{\tan^2\beta_i}{2}$$

$$\tan\beta_i\lambda = \frac{1}{2}(1 - \tan^2\beta_i) \tag{A.13}$$

$$\eta = \frac{1}{2}(1 - \tan^2\beta_i) \tag{A.14}$$

We operate further on Equation A.13:

$$2\tan\beta_i\lambda = 1 - \tan^2\beta_i$$

$$\tan^2\beta_i + 2\tan\beta_i\lambda - 1 = 0$$

$$(\tan\beta_i + \lambda)^2 = \lambda^2 + 1$$

$$\tan\beta_i = -\lambda \pm \sqrt{\lambda^2 + 1}$$

$$\text{for } \tan\beta_i > 0 \qquad \tan\beta_i = -\lambda + \sqrt{\lambda^2 + 1}$$

We expand this equation in order to determine its behavior for large values of λ:

$$\tan\beta_i = -\lambda + \lambda\sqrt{1 + \frac{1}{\lambda^2}}$$

$$\tan\beta_i \approx -\lambda + \lambda\left[1 + \frac{1}{2}\frac{1}{\lambda^2} + \mathcal{O}\left(\frac{1}{\lambda^4}\right)\right]$$

$$\tan\beta_i \approx \frac{1}{2}\frac{1}{\lambda} + \mathcal{O}\left(\frac{1}{\lambda^3}\right)$$

$$\tan\beta_i \approx \frac{1}{2}\frac{1}{\lambda}$$

Then as $\lambda \to \infty$, $\tan\beta_i \to 0$. The maximum efficiency according to *linear theory* will be determined by Equation A.14:

$$\eta_{\text{MAX (linear)}} = \tfrac{1}{2} = 0.5 \tag{A.15}$$

An expression for the efficiency can also be found as $\lambda \to 0$:

$$\eta = \frac{1}{2}\left(1 - \frac{1}{4\lambda^2}\right)$$

However this analysis is based on the underlying assumption of constant circulation distribution along the blade. While the LLOPT-LW results presented in Section 4.1.1 seem to approach a constant-loading distribution for high TSR turbines, that is not the case for low TSR turbines.

An analysis that includes the non-linear coefficients has been attempted, but results are inconclusive. This derivation appears to prove that classical linear optimization based on the Lerbs-Wrench formulas cannot produce efficiencies higher than 50%. Epps and Kimball (2013) [11] use classical momentum theory in order to determine analytical expressions for the non-linear terms, which leads to efficiencies above the 50% limit.

Appendix B

Non-Linear Lifting Line Optimization

This appendix presents the formulation for a non-linear extension to the classical lifting line model in order to include higher order terms in the case of inviscid flow. Preliminary results are presented.

B.1 Formulation

As shown in Appendix B, it can be argued that the assumption of linearity followed in equation 3.23, given the use of the Lerbs-Wrench formulas, limits the maximum efficiency that can be obtained through that method to approximately 50%. Results obtained from analysis studies carried out by Falcão de Campos (2007) [13] seem to confirm this argument. Full wake alignment provides a path to overcoming this limitation, but an alternate solution within the boundaries of the classical Lerbs-Wrench formulas could be the inclusion of the non-linear terms. It is worth noting that Epps and Kimball (2013) [11] used momentum theory to derive analytical expressions for these terms, obtaining higher efficiencies.

We simplify the problem by assuming inviscid behavior ($\kappa = 0$). Equa-

tion 3.21 can then be expressed as:

$$Q = \rho Z V^2 R^3 \left\{ \sum_{m=1}^{M} \left[1 - \sum_{m=1}^{M} \overline{\Gamma_n} \overline{u_a}(m,n) \right] \overline{\Gamma_m} \overline{r_m} \overline{\Delta r_m} \right\} \tag{B.1}$$

We take the derivative of the torque with respect to the circulation once again, but in this case we do not neglect the non-linear terms. We obtain a system of M differential equations, as follows:

$$f_i = \frac{\partial Q}{\partial \overline{\Gamma_i}} = 0 \qquad i = 1, \ldots, M \tag{B.2}$$

$$f_i = \overline{r_i} \overline{\Delta r_i} - \sum_{m=1}^{M} \left\{ \left[\overline{r_i} \overline{\Delta r_i} \overline{u_a}(i,m) + \overline{r_m} \overline{\Delta r_m} \overline{u_a}(m,i) \right] \overline{\Gamma_m} \right\} - \sum_{m=1}^{M} \sum_{n=1}^{M} \left\{ \overline{r_m} \overline{\Delta r_m \Gamma_m \Gamma_n} \frac{\partial \left(\overline{u_a}(m,n) \right)}{\partial \overline{\Gamma_i}} \right\} \tag{B.3}$$

To solve this equation, we approximate the derivative $\frac{\partial(\overline{u_a}(m,n))}{\partial \overline{\Gamma_i}}$ by means of the finite difference $\frac{\Delta(\overline{u_a}(m,n))}{\Delta \overline{\Gamma_i}}$. The linear system is solved first, obtaining a base circulation distribution Γ_i. A small $\Delta\Gamma_i$ is added to each discrete circulation value, and an analysis run is executed in order to obtain the new $\overline{u_a}(m,n)$ for each $\Delta\Gamma_i$. The wake is aligned through the iterative process described in Figure 3.8 until it converges to a new hydrodynamic pitch angle β_i, which differs from the angle calculated for the undisturbed circulation distribution. M sets of $M \times M$ finite differences are calculated and assumed to be constant coefficients in the non-linear set of equations given by B.3. The error introduced by this assumption is assumed a priori to be of a second order of magnitude, and thus negligible in a preliminary formulation.

The non-linear equation is solved by using the Newton-Raphson method for systems of equations.

$$J\,\widetilde{\Delta\Gamma} = -\widetilde{f} \tag{B.4}$$

where J is the Jacobian of the system of equations f_i. In matrix form:

$$\begin{bmatrix} \frac{\partial f_1}{\partial \overline{\Gamma_1}} & \frac{\partial f_1}{\partial \overline{\Gamma_2}} & \cdots & \frac{\partial f_1}{\partial \overline{\Gamma_M}} \\ \frac{\partial f_2}{\partial \overline{\Gamma_1}} & \frac{\partial f_2}{\partial \overline{\Gamma_2}} & \cdots & \frac{\partial f_2}{\partial \overline{\Gamma_M}} \\ \vdots & \vdots & \ddots & \vdots \\ \frac{\partial f_M}{\partial \overline{\Gamma_1}} & \frac{\partial f_M}{\partial \overline{\Gamma_2}} & \cdots & \frac{\partial f_M}{\partial \overline{\Gamma_M}} \end{bmatrix}^{(\widetilde{\Gamma}_n)} \begin{bmatrix} \Delta\Gamma_1 \\ \Delta\Gamma_2 \\ \vdots \\ \Delta\Gamma_M \end{bmatrix} = - \begin{bmatrix} f_1 \\ f_2 \\ \vdots \\ f_M \end{bmatrix}^{(\widetilde{\Gamma}_n)} \tag{B.5}$$

The solution is approximated in successive iterations according to:

$$\widetilde{\Gamma}_{n+1} = \widetilde{\Gamma}_n + \widetilde{\Delta\Gamma} \tag{B.6}$$

and the derivates of the Jacobian can be calculated as:

$$\begin{aligned} \frac{\partial f_i}{\partial \overline{\Gamma_j}} = & -\overline{r_i}\overline{\Delta r_i}\overline{u_a}(i,j) - \overline{r_j}\overline{\Delta r_j}\overline{u_a}(j,i) \\ & - \sum_{n=1}^{M} \overline{r_j}\overline{\Delta r_j \Gamma_n} \frac{\partial\left(\overline{u_a}(j,n)\right)}{\partial \overline{\Gamma_i}} - \sum_{n=1}^{M} \overline{r_n}\overline{\Delta r_n \Gamma_n} \frac{\partial\left(\overline{u_a}(n,j)\right)}{\partial \overline{\Gamma_i}} \end{aligned} \tag{B.7}$$

B.2 Preliminary Results and Recommendations

The evaluation of the full equation B.3 leads to a highly asymmetric solution for the circulation distribution (i.e. higher values at the hub than at the tip) that had an efficiency which did appear reach Betz's limit for large values of tip speed ratio and large number of blades. Since no hub model was included in this method, it was expected that the circulation went to zero at the hub. This result has not yet been explained.

As an alternative, non-direct derivatives were excluded. That is, only $\frac{\Delta(\overline{u_a}(m,i))}{\Delta\overline{\Gamma}_i}$ were included in the formulation, forming only 1 set of $M \times M$ finite differences. The justification for this selection is based on: a) the fact that these terms are overall larger in magnitude, and b) they are directly originated by the increase in each section's circulation, $\Delta\Gamma_i$). With this assumption, a more rational result was obtained. In their analysis, Epps and Kimball (2013) [11] consider all off-diagonal terms to be negligible, a similar assumption. The results for the linear formulation (original LLOPT-LW), the non-linear formulation considering all terms and the non-linear formulation considering only the direct derivatives are presented in Figure B.1.

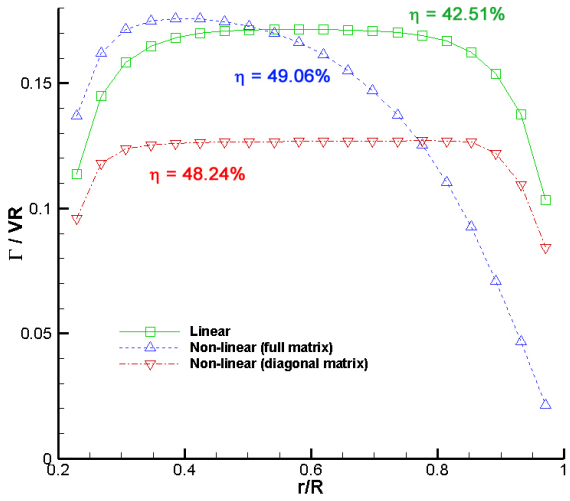

Figure B.1: Circulation distributions as a function of the normalized radius for a three-bladed turbine using inviscid linear (LLOPT-LW) and non-linear methods. ($Z = 3$; $M = 20$; $TSR = 6$; $r_h/R = 0.2$)

The non-linear method results in efficiencies that are considerably higher,

in both its versions, and convergence is good for the full-matrix case and moderately good for the partial-matrix method. The results are not however satisfactory and potentially indicate a lack of compatibility between a non-linear approach and the use of the Lerbs-Wrench formulas. It is suggested that this same approach be extended to the new LLOPT-FWA model, in order to ascertain the accuracy of the linear assumption made in Equation 3.23. The considerable computational effort required to align the complete wake makes the implementation of a partial wake alignment procedure a necessity if the non-linear formulation is to be explored.

Appendix C

NACA Data for Blade Geometry Design

C.1 NACA Mean Line a = 0.8

This data included in this section was published in Abbott (1959) [1].

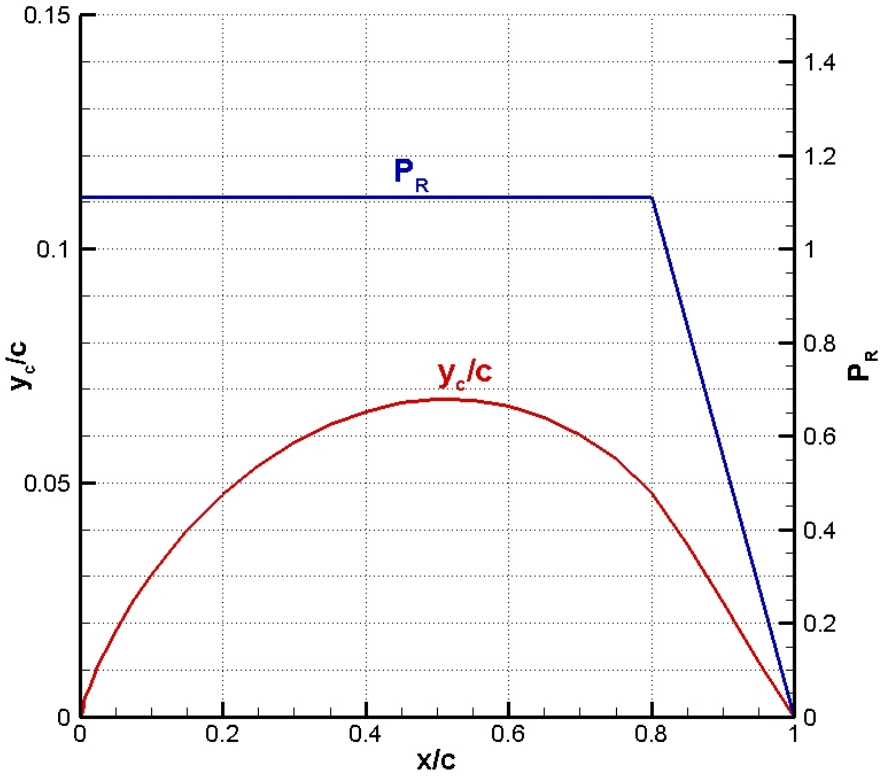

Figure C.1: Pressure distribution and camber line for NACA a=0.8

$C_{L_i} = 1.0$		$\alpha_i = 1.5\,^\circ$	$c_{m_{c/4}} = -0.202$	
x (per cent c)	y_c (per cent c)	dy_c/dx	P_R	$\Delta v/V = P_R/4$
0	0			
0.5	0.287	0.48535	1.111	0.278
0.75	0.404	0.44925	1.111	0.278
1.25	0.616	0.40359	1.111	0.278
2.5	1.077	0.34104	1.111	0.278
5.0	1.841	0.27718	1.111	0.278
7.5	2.483	0.23868	1.111	0.278
10	3.043	0.21050	1.111	0.278
15	3.985	0.16892	1.111	0.278
20	4.748	0.13734	1.111	0.278
25	5.367	0.11101	1.111	0.278
30	5.863	0.08775	1.111	0.278
35	6.248	0.06634	1.111	0.278
40	6.528	0.04601	1.111	0.278
45	6.709	0.02613	1.111	0.278
50	6.790	0.00620	1.111	0.278
55	6.770	-0.01433	1.111	0.278
60	6.644	-0.03611	1.111	0.278
65	6.405	-0.06010	1.111	0.278
70	6.037	-0.08790	1.111	0.278
75	5.514	-0.12311	1.111	0.278
80	4.771	-0.18412	1.111	0.278
85	3.683	-0.23921	0.833	0.208
90	2.435	-0.25583	0.556	0.139
95	1.163	-0.24904	0.278	0.069
100	0	-0.20385	0	0

Table C.1: Data for NACA a=0.8

C.2 NACA 66 Modified

The data for the modified NACA66 thickness distribution was obtained from Brockett (1966) [8].

	*$\rho_{LE} = 448\tau^2$	**Value at $x = .005$	
Station x	66 (Mod) Thickness $\frac{y_T}{\tau}$	a = 0.8 Camber $\frac{y_C}{f}$	Camberline Slope $\frac{dy_c}{dx}/f$
0	0*	0	7.1465**
0.007596	0.0817	0.06006	6.6001
0.030154	0.1608	0.18381	4.7712
0.066987	0.2368	0.33684	3.6751
0.116978	0.3135	0.49874	2.8581
0.178606	0.3807	0.65407	2.2096
0.250000	0.4363	0.79051	1.6350
0.328990	0.4760	0.89831	1.1071
0.413176	0.4972	0.96994	0.6001
0.500000	0.4962	1.00000	0.0914
0.586824	0.4712	0.98503	-0.4448
0.671010	0.4247	0.92306	-1.0483
0.750000	0.3612	0.81212	-1.8132
0.821394	0.2872	0.63864	-3.1392
0.883022	0.2108	0.42227	-3.7243
0.933013	0.1402	0.23423	-3.7425
0.969846	0.0830	0.09982	-3.5148
0.992404	0.0462	0.02365	-3.2028
1.000000	0.0333	0	-3.0025

Table C.2: Data for modified NACA 66

Bibliography

[1] I. H. Abbott and A. E. Von Doenhoff. *Theory of Wing Sections*. Dover Publications, 1959.

[2] Energy Information Administration. Annual Energy Outlook 2011, Report: DOE/EIA-0383, December 2010.

[3] P. Asmus and C. Wheelock. Hydrokinetic and ocean energy, Research reports, 2009, available from www.pikeresearch.com.

[4] A. S. Bahaj, W. M. J. Batten, and G. McCann. Experimental verifications of numerical predictions for the hydrodynamic performance of horizontal axis marine current turbines. *Renewable Energy*, 32(15):2479–2490, 2007.

[5] A. Betz. Schrauben propeller mit geringsten energieverlust. *K. Ges. Wiss. Gottingen Nachr. Math.-Phys. Klasse*, pages 193–217, 1919.

[6] A. Betz. Das maximum der theoretisch Möglichen Ausnützung des windes durch windmotoren. *Zeitschrift fr das Gesamte Turbinenwesen*, 26:307–309, 1920.

[7] J. Breslin, R. Van Houten, J. Kerwin, and C. A. Johnsson. Theoretical and experimental propeller-induced hull pressures arising from intermit-

tent blade cavitation, loading and thickness. *SNAME, Transactions*, 1982.

[8] T. Brockett. Minimum pressure envelopes for modified NACA-66 sections with NACA a = 0.8 camber and buships Type I and Type II sections. Technical Report 1780, David Taylor Model Basin, Bethesda, USA, 1966.

[9] T. Burton, D. Sharpe, N. Jenkins, and E. Bossanyi. *Wind Energy: Handbook*. John Wiley and Sons, 2001.

[10] B. P. Epps. *An impulse framework for hydrodynamic force analysis: fish propulsion, water entry of spheres, and marine propellers*. PhD thesis, Massachusetts Institute of Technology, 2010.

[11] B. P. Epps and R. W. Kimball. Unified rotor lifting line theory. *Journal of Ship Research*, Accepted, 2013.

[12] B. P. Epps, M. J. Stanway, and R. W. Kimball. Openprop: An open source design tool for propellers and turbines. In *Society of Naval Architects and Marine Engineers Propeller/Shafting 09 Symposium*, Virginia Beach, USA, September 2009.

[13] J. A. C. Falcão de Campos. Hydrodynamic power optimization of a horizontal axis marine current turbine with a lifting line theory. In *17th Internacional Offshore and Polar Engineering Conference*, Lisbon, Portugal, July 2007.

[14] N. E. Fine and S. A. Kinnas. A boundary-element method for the analysis of the flow around 3-d cavitating hydrofoils. *Journal of Ship Research*, 37(3):213–224, 1993.

[15] C. Frid, E. Andonegi, J. Depestele, A. Judd, D. Rihan, S. I. Rogers, and E. Kenchington. The environmental interactions of tidal and wave energy generation devices. *Environmental Impact Assessment Review*, 32(1):133–139, 2012.

[16] H. Glauert. *The Elements of Aerofoil and Airscrew Theory*. New York: Cambridge University Press, 1947.

[17] M. Gullikson and P.-Å. Wedin. Modifying the QR-decomposition to constrained and weighted linear least squares. *SIAM Journal on Matrix Analysis and Applications*, 13(4):1298–1313, 1992.

[18] M. S. Güney and K. Kaygusuz. Hydrokinetic energy conversion systems: A technology status review. *Renewable and Sustainable Energy Reviews*, 14(9):2996–3004, 2010.

[19] L. He. *Numerical simulation of unsteady rotor/stator interaction and application to propeller/rudder combination*. PhD thesis, The University of Texas at Austin, 2010.

[20] J. E. Kerwin. Hydrofoils and Propellers (13.04 Lecture Notes), Massachusetts Institute of Technology, 2001.

[21] J. E. Kerwin, W. B. Coney, and C-H. Hsin. Optimum circulation distribution for single and multi-component propulsorts. In *21st American Towing Tank Conference*, Washington DC, USA, 1986.

[22] J. E. Kerwin and J. C. Hadler. *Propulsion, The Principles of Naval Architecture Series*. SNAME, 2010.

[23] J. E. Kerwin, S. A. Kinnas, J-T. Lee, and W-Z Shih. A surface panel method for the hydrodynamic analysis of ducted propellers. *SNAME, Transactions*, 1987.

[24] J. E. Kerwin and C. S. Lee. Prediction of steady and unsteady marine propeller performance by numerical lifting-surface theory. *SNAME, Transactions*, 86:218–253, 1978.

[25] S. A. Kinnas. Leading-edge corrections to the linear theory of partially cavitating hydrofoils. *Journal of Ship Research*, 35(1):15–27, 1991.

[26] S. A. Kinnas and W. B. Coney. The generalized image model - an application to the design of ducted propellers. *Journal of Ship Research*, 36(3), 1992.

[27] S. A. Kinnas and N. E. Fine. A numerical nonlinear-analysis of the flow around 2-dimensional and 3-dimensional partially cavitating hydrofoils. *Journal of Fluid Mechanics*, 254:151–181, 1993.

[28] S. A. Kinnas and S. Pyo. Cavitating propeller analysis including the effects of wake alignment. *Journal of Ship Research*, 43(1):38–47, 1999.

[29] S. A. Kinnas, W. Xu, Y-H. Yu, and L. He. Computational methods for the design and prediction of performance of tidal turbines. *Journal of Offshore Mechanics and Arctic Engineering (OMAE)*, 134(1), 2012.

[30] O. Langhamer and D. Wilhelmsson. Colonisation of fish and crabs of wave energy foundations and the effects of manufactured holes - a field experiment. *Marine Environmental Research*, 68(4):151–157, 2009.

[31] Lazard. Levelized Cost of Energy Analysis, Version 5.0, August 2011.

[32] C. S. Lee. *Prediction of steady and unsteady performance of marine propeller with or without cavitation by numerical lifting surface theory.* PhD thesis, Massachusetts Institute of Technology, 1979.

[33] H. S. Lee and S. A. Kinnas. Unsteady wake alignment for propellers in nonaxisymmetric flows. *Journal of Ship Research*, 49(3):176–190, 2005.

[34] J.-T. Lee. *A potential based panel method for the analysis of marine propellers.* PhD thesis, Massachusetts Institute of Technology, 1987.

[35] H. W. Lerbs. Moderately loaded propellers with a finite number of blades and an arbitrary distribution of circulation. *SNAME, Transactions*, 60:73–129, 1952.

[36] T. P. Lloyd, V. F. Humphrey, and S. R. Turnock. Noise modelling of tidal turbine arrays for environmental impact assessment. In *9th European Wave and Tidal Energy Conference*, Southampton, GB, September 2011.

[37] T. A. Loukakis. *A new theory for the wake of marine propellers.* PhD thesis, Massachusetts Institute of Technology, 1971.

[38] Haskoning UK Ltd. SeaGen Environmental Monitoring Programme - Final Report, Report: 9S8562/R/303719/Edin, January 2011.

[39] D. Menéndez Arán and S. A. Kinnas. Hydrodynamic optimization of marine current turbines. In *17th Offshore Symposium, SNAME*, Houston, USA, February 2012.

[40] D. Menéndez Arán and S. A. Kinnas. Optimization and prediction of performance of marine current turbines. In *18th Offshore Symposium, SNAME*, Houston, USA, February 2013.

[41] S. Mishima and S. A. Kinnas. Application of a numerical optimization technique to the design of cavitating propellers in nonuniform flow. *Journal of Ship Research*, 41(2):93–107, 1997.

[42] R. H. Myers. *Classical and Modern Regression with Applications.* Duxbury Classic, 2000.

[43] Department of Energy and Climate Change. Marine Energy Action Plan, United Kingdom, March 2010.

[44] M. Öhman, P. Sigray, and H. Westerberg. Offshore windmills and the effects of electromagnetic fields on fish. *AMBIO: A Journal of the Human Environment*, 36(8):630–633, 2007.

[45] H. J. Stewart. Dual optimum aerodynamic design for a conventional windmill. *AIAA Journal*, 14(11):1524–1527, 1976.

[46] Frost & Sullivan. Hydro, Wave, and Tidal Power - Market Penetration and Roadmapping (Technical Insights), March 2010.

[47] H. Sun and S. A. Kinnas. Performance prediction of cavitating waterjet propulsors using a viscous/inviscid interactive method. In *SNAME Annual Meeting and Ship Production Symposium*, Houston, USA, 2008.

[48] Y. Tian and S. A. Kinnas. A wake model for the prediction of propeller performance at low advance ratios. *International Journal of Rotating Machinery*, 2012(4):519–527, 2012.

[49] D. Wilhelmsson, T. Malm, and M. Öhman. The influence of offshore wind power on demersal fish. *ICES Journal of Marine Science*, 63:775–784, 2006.

[50] J. W. Wrench. The calculation of propeller induction factors. Technical Report 1116, David Taylor Model Basin, Bethesda, USA, 1957.

[51] W. Xu. A Study of Producing the Maximum Efficiency for the Wind Turbine and Propeller, Report N UT-OE 09-1, Department of Civil Engineering, The University of Texas at Austin, 2009.

[52] W. Xu. Numerical techniques for the design and prediction of performance of marine turbines and propellers. Master's thesis, Department of Civil Engineering, The University of Texas at Austin, 2010.

[53] W. Xu and S. A. Kinnas. Performance prediction and design of marine current turbines in the presence of cavitation. *SNAME, Transactions*, 118, 2010.

[54] K. Zan. A Study of Optimum Circulation Distributions for Wind Turbines, Report N UT-OE 08-3, Department of Civil Engineering, The University of Texas at Austin, 2008.

Vita

David Menéndez Arán hails from Buenos Aires, Argentina. He was born in 1982, the son of Norberto Menéndez and Ana Arán. He graduated with honors in 2007 from the University of Buenos Aires with a Professional Degree in Civil Engineering. In the fall of 2011, he enrolled at the University of Texas at Austin to continue his studies as part of the Ocean Engineering Group at the Department of Civil, Architectural and Environmental Engineering.

Permanent address: 9014 Woodland Trace
Boerne, Texas 78006
dmenendez@gmail.com

This thesis was typeset with LaTeX[†] by the author.

[†]LaTeX is a document preparation system developed by Leslie Lamport as a special version of Donald Knuth's TeX Program.